Growth of spatially ordered ZnO nanowire arrays for field emission applications

Séamus Garry B.Sc.

School of Physical Sciences

Dublin City University

A thesis submitted to Dublin City University

for the degree of

Doctor of Philosophy

Research Supervisor

Dr. Enda McGlynn

March 2013

Declaration

I hereby certify that this material, which I now submit for assessment on the programme of study leading to the award of Doctor of Philosophy is entirely my own work, that I have exercised reasonable care to ensure that the work is original, and does not to the best of my knowledge breach any law of copyright, and has not been taken from the work of others save and to the extent that such work has been cited and acknowledged within the text of my work.

Signed: _______________________

ID No.: 54007034

Date: 4th March 2013

Acknowledgements

Firstly, I would like to thank my supervisor Dr. Enda McGlynn for giving me the opportunity to work on such an interesting project and for all his assistance, advice, and patience. I have benefitted greatly under his guidance and reassurance. I would also like to thank Dr. Jean-Paul Mosnier for his help and input throughout my work.

I would also like to thank all the staff at DCU, in particular Des Lavelle, Pat Wogan, Alan Hughes, Lisa Peyton, and Sheila Boughton, who have happily helped out in so many ways during my time here.

I would also like to thank my colleagues in the lab for all their time and support. In particular I'd like to thank Dr. Ruth Saunders, for many chats and so much encouragement, Dr. Daragh Byrne, for his endless patience and invaluable assistance; and to Dr. Mahua Biswas, Dr. Joe Cullen, and Ciarán Gray for their help and input and for making the lab a pleasant place to work. A special thanks to Éanna McCarthy, for all the assistance and for so many ZnO discussions over the course of our collaboration, especially during the preparation of my thesis.

Thank you too to all those who have enriched my experience at DCU, Mossy Kelly, Jiang Xi, Conor Coyle, Colm Fallon, Nicky Walsh, Vincent Richardson, Catherine Doyle, and Jack Connolly. Thank you all for making working here an enjoyable and very entertaining experience.

I must also thank my parents, for their endless support and encouragement, all my friends for support and for always being there. Finally, I must thank Gary, for being there for me, putting up with me, for unwavering support, and brightening my life immeasurably.

Abstract

In this work the growth of spatially ordered and vertically aligned ZnO nanowires is examined. Nanowire arrays are grown using chemical bath deposition (CBD) and carbothermal reduction vapour phase transport (CTR-VPT) techniques. Nanosphere lithography (NSL) was used to achieve spatial ordering of these arrays; arrays with inter-wire distances of 500 nm, 1.0 µm, and 1.5 µm were grown using both CBD and CTR-VPT techniques. Two distinct implementations of the NSL technique are investigated, one which relied on the deposition of a catalyst material and one which involved the deposition of a secondary mask which prevents ZnO deposition from occurring in undesired areas. The field emission (FE) characteristics of these arrays were examined, revealing a significant dependence of the FE properties on both nanowire morphology and array density. A geometric factor is calculated which is dependent on both nanowire aspect ratio and the density of nanowires in an array and this factor has been found to correlate with other indicators of FE properties. The results presented in this work may be useful in informing the design of ZnO nanowire arrays in order to maximise their FE efficiency and uniformity.

Table of Contents

List of figures: Abbreviated titles

List of tables

List of acronyms

CBD:	Chemical Bath Deposition
CTR:	Carbothermal Reduction
CTR-VPT:	Carbothermal Reduction Vapour Phase Transport
CVD:	Chemical Vapour Deposition
DI-H_2O:	Deionised water
EDX:	Energy Dispersive X-ray spectroscopy
FCC:	Face-Centred Cubic
FE:	Field Emission
FEI:	Field Emission Imaging
FESEM:	Field Emission Scanning Electron Microscope
FN:	Fowler-Nordheim
FWHM:	Full Width at Half Maximum
HCC:	Hexagonal Close Packing
HCl:	Hydrochloric acid
HMT:	Hexamethylenetetramine/Hexamine
IPA:	Isopropyl Alcohol
ITO:	Indium Tin Oxide
I-V:	Current/Voltage
MFC:	Mass Flow Controller
NSL:	Nanosphere Lithography

PLD:	Pulsed Laser Deposition
PTFE:	Polytetrafluoroethylene
RIE:	Reactive Ion Etching
SDS:	Sodium Dodecyl Sulfate
SEM:	Scanning Electron Microscope
TEM:	Transmission Electron Microscope
TEOS:	Tetraethylorthosilicate
VLS:	Vapour-Liquid-Solid
VPT:	Vapour Phase Transport
WKB:	Wentzel-Kramers-Brillouin
XRD:	X-Ray Diffraction

Publications

Control of ZnO nanowire arrays by nanosphere lithography (NSL) on laser-produced ZnO substrates.

Garry S, McCarthy E, Mosnier JP, McGlynn E, Appl. Surf. Sci. 257, 5159 (2011)

Field emission in ordered arrays of ZnO nanowires prepared by nanosphere lithography and extended Fowler-Nordheim analyses.

McCarthy E, Garry S, Byrne D, McGlynn E, Mosnier JP, Journal Appl. Phys. 110, 124324 (2012)

Length versus radius relationship for ZnO nanowires grown via Vapour Phase Transport.

Saunders, Ruth; Garry, Seamus; Byrne, Daragh; Henry, Martin; McGlynn, Enda.

Crystal Growth and Design, 12 (2012) 5972–5979.

Conferences

Oral Presentations:

Control of ZnO nanowire arrays by nanosphere lithography (NSL) on laser-produced ZnO substrates.

Garry S, McCarthy E, Mosnier JP, McGlynn E, EMRS, Strasbourg, 2010

Poster presentations:

Growth and Characterisation of ZnO Nanowires for Field Emission Applications.

S. Garry, É. McCarthy, C. McLoughlin, S. Krishnamurthy, E. McGlynn, and J.P. Mosnier, EMRS, Strasbourg, 2009

Optimisation of ZnO nanowires for field emission application.

É. McCarthy, S. Garry, J. Connolly, E. McGlynn, and J.P. Mosnier , EMRS, Strasbourg, 2010

Control of ZnO nanowire array morphology for field emission imaging.

S. Garry, É. McCarthy, J.P. Mosnier, and E. McGlynn, Photonics Ireland, Malahide, 2011

Growth of Zinc Oxide Nanostructures by Pulsed Laser Deposition for Field Emission Application.

É. McCarthy, S. Garry, E. McGlynn, and J.P. Mosnier, Photonics Ireland, Malahide, 2011

Chapter 1: Introduction

1.1 Introduction

This chapter will provide some general background information on the topics covered in this thesis, including the basic material properties of zinc oxide (ZnO) as a semiconductor material and more specifically background information on the growth of ZnO nanostructures. ZnO has a strong propensity to grow in nanostructured form with a wide range of morphologies that are sensitive growth parameters such as substrate type, deposition technique, and temperature. Because of this sensitivity and morphological diversity, along with its crystal and electrical properties as outlined below, ZnO has attracted much attention in recent years as it has considerable potential in a large number of applications [1-4].

1.2 Applications and motivation

The main motivation for this work is the goal of developing a method for producing ZnO nanowire arrays whose morphological properties such as inter-wire separation, nanowire length, etc. may be controlled using techniques that are simple to implement in terms of equipment and materials requirements, and that may be implemented reliably and repeatably. There has been much interest in recent years in developing techniques that allow for the deposition of spatially ordered nanowire arrays with a number of techniques being found capable of producing such ordered nanowire arrays, including e-beam lithography, laser interference lithography, mask lithography and others [5-12].

These techniques yield impressive results and appear to address the need to create ordered nanowire arrays for further research/technological purposes. However, due to the expense associated with the implementation of these techniques they are not viable options for many research groups and due to a possible lack of scalability they are also not a viable option for industrial use either. For this reason, nanosphere lithography (NSL), a relatively simple technique which is very inexpensive to implement was investigated in this work. This technique has been the subject of significant interest in recent years with a large number of publications reporting successful implementations; its use has not been limited to ZnO nanowires as is the goal of this work, but also to nanowires of a number of materials such as gallium nitride or gallium arsenide on a range of substrates [13, 14]. In brief, a lithographic mask of known spacing and aperture size may be deposited on a substrate with relative ease, this mask then allows for the patterned deposition of other materials, or for the selective etching of the substrate material [13, 15]. The development and refinement of this technique in this thesis and in the literature represent an advance in the capabilities of research groups in the area of nanolithography that previously would have required a large capital expenditure to achieve.

The second objective for this work is to characterise spatially ordered ZnO nanowire arrays by field emission with the goal of optimising array morphology to maximise the efficiency and emission uniformity of the arrays produced. The motivation for this is the large number of possible applications for field emission in technology, in particular in light sources and displays [16-18]. A brief introduction to field emission is given later in this chapter.

1.3 Material properties

ZnO is a II-VI semiconductor material with a wide direct band gap of 3.34 eV [19]. Materials with direct band gaps are useful technologically for optoelectronic devices since in a direct gap material radiative transitions can occur without any change in crystal momentum, and thus are a highly probable transition path (compared to non-radiative decays) and thus suitable for light emission devices. This is in contrast to the case for indirect band gap materials where radiative transitions can't happen without a change in crystal momentum, which normally proceeds by phonon absorption/emission making them much less probable than non-radiative decays, and thus such indirect band gap materials are much less suitable for optoelectronic devices. The large band gap of 3.34 eV corresponds to the blue/UV part of the spectrum, which give it potential applications in areas such as short wavelength light sources for optical data storage and also white lighting, while its exciton binding energy of 60 meV [19] is higher than the thermal energy at room temperature means it has the potential for highly efficient excitonic light emission at room temperature.

1.3.1 Crystal structure

Zinc oxide is a group II-VI binary compound semiconductor. The structure of most of this group of compounds (II-VI) is either cubic zinc-blende or hexagonal wurtzite structures where, in each case, each anion is surrounded by four cations and *vice versa*. Zn or O atoms in the crystal lattice involve hybridisation of the atomic orbitals leading to four equivalent sp^3 orbitals in a (close-to) tetrahedral geometry. At ambient pressure and temperature ZnO crystallises in the wurtzite structure which is the most stable phase under normal conditions. Under certain conditions ZnO can crystallise in either a zinc-blende or rocksalt phase. The zinc-blende phase is stable at ambient pressure and temperature when ZnO is grown on cubic substrates [20] while the rock-salt phase is only stable at very high pressures (~9 – 10 GPa) and is a metastable phase when pressure is reduced [21, 22]. The present work, like most work in this area, is conducted at (or below) atmospheric pressure and as such the wurtzite structure is the only one of relevance here.

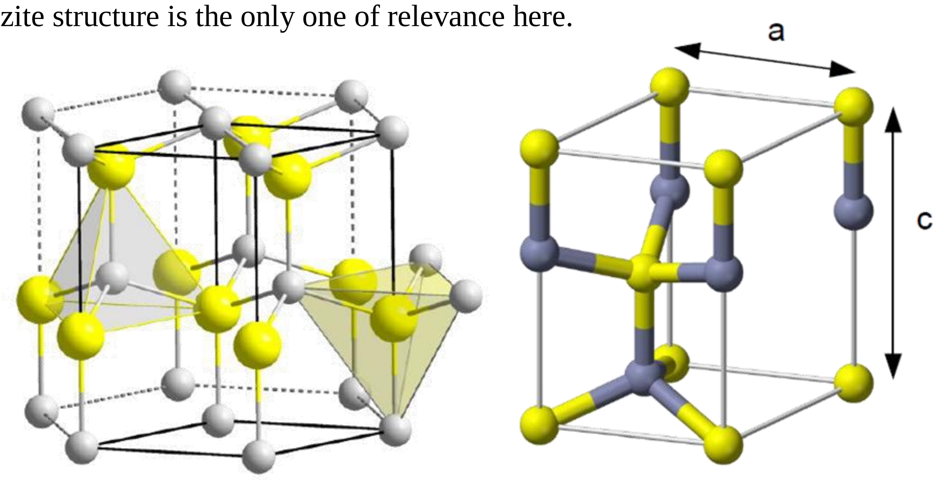

Figure 1.1: The wurtzite crystal structure of ZnO showing the tetrahedral coordination of each atom with 4 atoms of the second type (left) and the unit cell of wurtzite structured ZnO (right). Images reproduced from reference [23].

Figure 1.1 shows the hexagonal structure of the wurtzite crystal structure and its unit cell. The wurtzite unit cell contains two ZnO molecules and an ideal wurtzite unit cell has two lattice parameters, c and a, in the ratio $c/a = \sqrt{(8/3)} = 1.6330$. At room temperature in ZnO these lattice parameters are $a = 0.32498$ nm and $c = 0.52066$ nm and the ratio of c/a is then 1.6021 [24]. This deviation from ideal lattice parameters is possibly due to partial ionicity in the ZnO bonding which may lead to a distortion in the bond angle [1]. The wurtzite structure consists of planes of a single atom type in a hexagonal close packed configuration; each atom is coordinated with four atoms of the other type which also form hexagonal close packed planes both above and below. The ZnO wurtzite structure has a single main axis of symmetry, along the *c*-axis, with sixfold rotational symmetry, but does not possess inversion symmetry. The ZnO unit cell has a volume of 23.8 $Å^3$ [24].

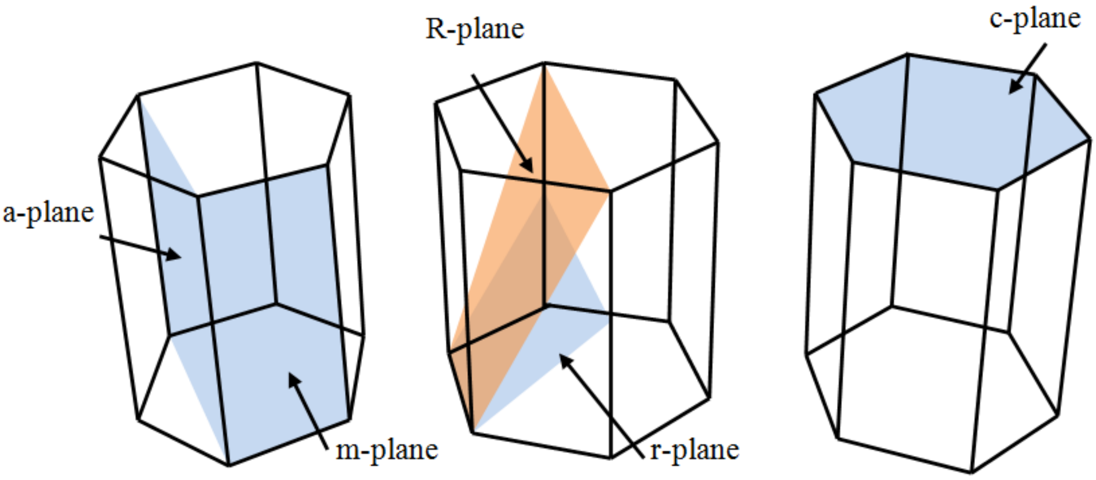

Figure 1.2: Hexagonal ZnO structure showing various crystal planes.

Figure 1.2 shows the principal planes of the ZnO wurtzite structure. The *a*-plane and *m*-plane contain the *c*-axis and using Miller-Bravais notation these are denoted by $(1\bar{1}20)$ and $(10\bar{1}0)$ respectively. The *a*-plane and *m*-plane are both terminated with Zn and O atoms and are non-polar. The c-plane is perpendicular to the c-axis and due to the nature of the wurtzite structure, having alternating hexagonally close packed planes of Zn and O atoms, is polar. Little information is available on the semi-polar *r*-plane $(10\bar{1}1)$ and *R*-plane $(10\bar{1}2)$, possibly due to difficulties in achieving epitaxial crystal growth in these planes [25]. Anisotropy in the crystal structure is very important factor in nanostructure growth as it leads to the preferential growth of ZnO along the *c*-axis as there will be preferential atom/molecule incorporation on the polar faces rather than on the non-polar side faces [26-28]. Some examples of morphologies exhibited by ZnO are shown in figure 1.3. The crystal structure of ZnO also gives rise to strong piezoelectric and pyroelectric properties; as such ZnO has found uses in mechanical actuators and piezoelectric sensors.

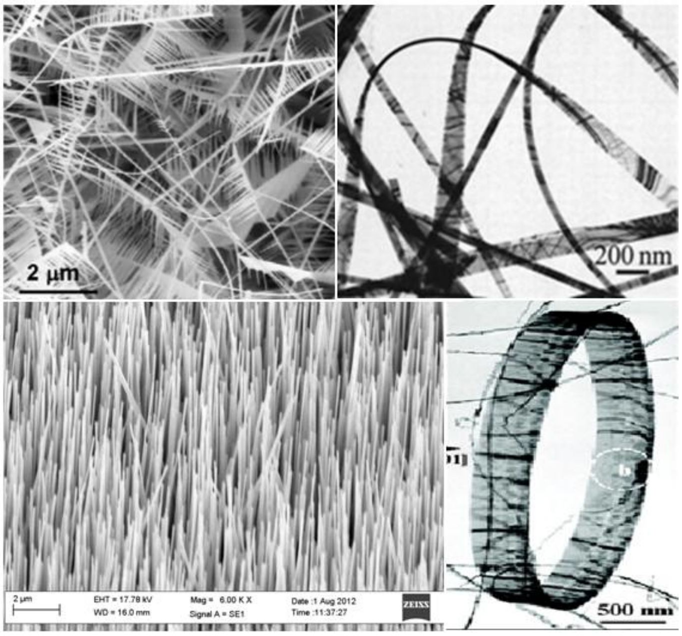

Figure 1.3: TEM/SEM images of ZnO nanostructures including (clockwise from top left) nanocombs from Z. L. Wang *et al.*[29], nanobelts from Z. W. Pan *et al*. [30], nanoring from X. Y. Kong *et al*. [31], and nanowires grown during this work.

1.3.2 Electronic structure

The outer electron configuration of Zn metal is $3d^{10}\ 4s^2$ while the outer electron configuration of oxygen is $2s^2\ 2p^4$. ZnO has sp^3 hybridised bonding, and because oxygen has a greater electronegativity than zinc, the outer $4s^2$ zinc electrons are drawn into unequal bonds with the oxygen to stabilise the oxygen outer shell. There remains some uncertainty in the understanding of the complete band structure of ZnO, with experimental results not accurately explained by theoretical models. This discrepancy has been partly explained by the role of the Zn 3d electrons, which have been treated theoretically as core level features for ease of calculation, as experimental evidence suggests that they have an effect on the position of the Zn 4s and O 2p valence band electrons [32-38]. The strongest influence on the valence band position is the hybrid orbitals of the Zn 4s and O 2p electrons. Figure 1.4 shows a schematic representation of the ZnO band structure. The band gap is between the O^{2-} 2p valence band and the Zn^{2+}4s conduction band states.

ZnO has a direct band gap of ~3.3 eV, meaning that the valence band maximum and conduction band minimum are at the same location in reciprocal space (i.e. they have the same k-vector). The conduction band is primarily composed of the empty Zn^{2+} 4s orbitals having Γ_7 symmetry while the valence band is formed from the occupied O^{2-} 2p *p*-type orbitals. The O *p*-type orbitals are split by the tetrahedral crystal field into three bands labelled A, B, and C, which have symmetries of Γ_7, Γ_9, and Γ_7 respectively.

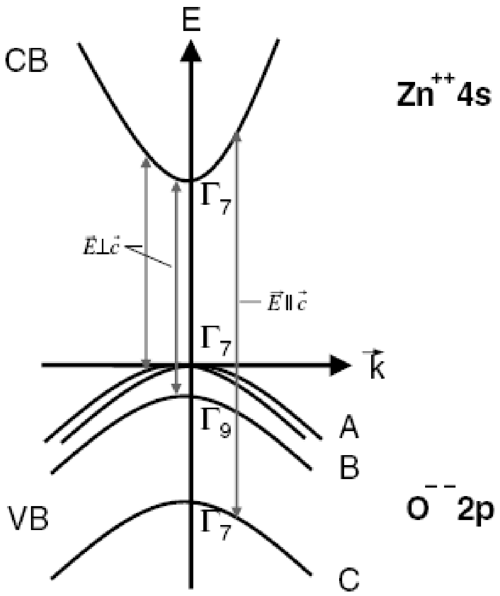

Figure 1.4: Schematic diagram of the ZnO electronic band structure. Image reproduced from reference [39].

ZnO is an intrinsic *n*-type semiconductor; the origin of this has been the subject of much debate over the years with varying theories being put forward in the literature. Deviations in material stoichiometry lead to the presence of native defects such as Zn interstitials (Zn_i) and O vacancies (V_o) in the ZnO lattice. Previously it was believed that these native defects were responsible for the intrinsic n-type conductivity of ZnO, but there remained uncertainty as to whether this conductivity was due to interstitials or vacancies [1, 40, 41]. It was later suggested that hydrogen was the source of *n*-type conductivity in ZnO. Hydrogen is amphoteric in most semiconductors, meaning that it is found as H^+ in p-type and as H^- in *n*-type semiconductors. In ZnO it is found only in the H^+ state and therefore acts as a donor [1]. Some reports suggested that native defects play little role in the n-type conductivity and that the effect is primarily due to hydrogen incorporated during the growth process [42, 43]. This possibility has been given prominence in the literature [1, 44] since hydrogen is ubiquitous during growth and has high diffusivity. Other impurities which act as donors in ZnO are aluminium (Al), gallium (Ga), and indium (In) and these are all present in most ZnO samples in trace amounts, which contribute to the background *n*-type conductivity.

Related to this natural *n*-type conductivity and associated uncertainty, efforts to effectively dope ZnO *p*-type in a reproducible and reliable way have faced serious challenges. There have been some reports of successful *p*-type doping in the literature using various dopants and deposition techniques [45-50]. Despite these reports however there are no indications of reliable and stable production of *p*-type ZnO and the material seems to be a unipolar *n*-type material. In particular there are no reports of reliable and stable high quality homoepitaxial ZnO pn junctions, which would be a first step in developing bi-polar optoelectronic devices. Because of ZnO’s unipolar electrical conduction, and as yet unsolved difficulties in *p*-type doping, some more recent research interest has turned to unipolar device technologies, such as field emission devices, which is one of the objectives of the present work. A more recent discussion of ZnO conductivity may be found in reference [51].

1.4 Growth techniques

There are many methods that may be used to deposit ZnO. In this section a brief outline of some of the more common techniques will be given, along with some of their main features.

ZnO thin films and nanostructures may be grown using chemical bath deposition (CBD) techniques. This has become increasingly popular due to the relatively inexpensive nature of the deposition process. There have been many techniques reported in the literature using a number of different precursor compounds; these are generally a Zn salt such as Zn acetate, nitrate, formate, sulphate, or chloride. These are generally used with a base chemical which can form Zn hydroxide [26, 52-55]. This is partially soluble and under certain conditions may be decomposed to form ZnO or Zn^{2+} which may then be oxidised to create ZnO [56]. Many bases have been used in these reactions including hexamine (HMT), ammonia, urea, sodium hydroxide, potassium hydroxide, or ethanolamine in solvents such as water, ethanol, methanol, propanol, or ethylene glycol [54, 57-65]. The choice of substrate, base, precursor chemicals, solvent, and addition of surfactant all influence the morphology of the resulting deposition. The chemical environment used may thus be adapted to suit particular needs, giving control over nanostructure and thin film morphology that other techniques can’t match. CBD depositions generally require only low temperatures (< 100°C), meaning that a wide range of substrates may be used which are not compatible with other high temperature deposition techniques. CBD techniques are used extensively in this work and more thorough description of the methods used and the results obtained will be given in chapters 2, 3, and 4.

Pulsed Laser Deposition (PLD) is a well established technique which has been used to deposit ZnO thin films and nanostructures [66-68]. The principle of PLD is that a pulsed laser vapourises the surface of a ZnO target in a vacuum. This creates a plasma which expands normal to the target surface and which is then incident on a substrate mounted some distance away from the target. The ablated material recondenses on the substrate surface. The morphological and crystal properties of the deposited ZnO may be altered by changing parameters such as substrate temperature, laser fluence, and gas pressure. PLD has the advantage that the deposited materials' stoichiometry is generally the same as that of the target due to the nature of the ablation process.

ZnO nanostructures and thin films have also been deposited using high temperature techniques such as chemical vapour deposition (CVD), plasma assisted CVD, and vapour phase transport (VPT) [69-78]. CVD is based on the decomposition of a precursor material on a substrate surface. The substrate is heated to a temperature at which the precursor material will decompose while the precursor is transported to the substrate using a carrier gas. Metal-organic precursors such as dimethylzinc, dimethylzinc triethylamine, or zinc acetylacetonate are used in the deposition of ZnO [44, 70]. ZnO nanostructures and films may also be deposited using VPT. This technique usually involves placing a substrate downstream from an elemental Zn source in a furnace. Typically the source material is a high quality ZnO powder which is reduced to Zn and O_2 at high temperatures. The Zn vapour is carried by a carrier gas to the substrate, where it is oxidised to create a ZnO deposit. A reducing agent is generally used in order to lower the temperatures required for the chemical reduction of ZnO source powders because significant sublimation of ZnO only occurs at temperatures greater than 1900°C. With the addition of carbon, carbothermal reduction (CTR) allows for reduction of ZnO powder and subsequent deposition to occur at ~ 900°C. CTR-VPT is used extensively in this work and will be discussed in more detail in chapters 2, 3, and 4.

1.5 Field emission

The goal of this thesis, as will be described in chapter 5 is to optimise ZnO nanowire array morphology for field emission efficiency and uniformity. There are a number of possible applications for field emission, such as display technologies, where ZnO, due to its propensity to grow in nanostructured form, along with its low electron affinity and low work function, offers significant materials' advantages.

The ability to create ZnO nanowire arrays with tailored morphological features such as nanowire height, diameter, and separation is beneficial as it is believed that these factors influence the field emission properties [79-81].

Field emission (FE) is a quantum-mechanical effect whereby free electrons in a metal or semiconductor may tunnel through a (close to) triangular energy barrier into a vacuum in the presence of an applied electric field but in the absence of any heating. Unlike other kinds of electron emission such as Schottky or thermionic emission where electrons overcome the potential barrier at the material surface, in field emission electrons tunnel through the barrier [82]. Much of the interest in the development of field emission electron sources has been for use in new technologies such as flexible displays [83, 84] or small x-ray sources [3, 84]. For these applications robust, sharp emitters of conductive, low work function materials are required. However, commercial development in this field generally has been hindered by various factors, including poor emission uniformity, the origin of which probably rests in the lack of fundamental understanding of the field emission process [85].

Field emission experiments are carried out by gradually increasing/decreasing the voltage applied to a ZnO nanowire sample with respect to an anode. The sample/anode separation is generally on the order of microns and the current is recorded at each voltage step. The *I-V* data gained in this way is interpreted based on Fowler-Nordheim theory [86]. Field emission occurs when an applied electric field reduces the potential barrier to a point where electrons may tunnel through. The effective barrier experienced by electrons is a combination of an image potential and the applied electric field, this is shown schematically in figure 1.5. The electrical current emitted through field emission is described by the Fowler-Nordheim equation as shown in equation 1.1, where *I* is the current emitted (A), β is a geometric factor (m^{-1}), *A* is the emission area (m^2), Φ is the work function (eV) and *f(y)* and *t(y)* are factors to correct for the image potential. A more detailed description is given in chapter 5.

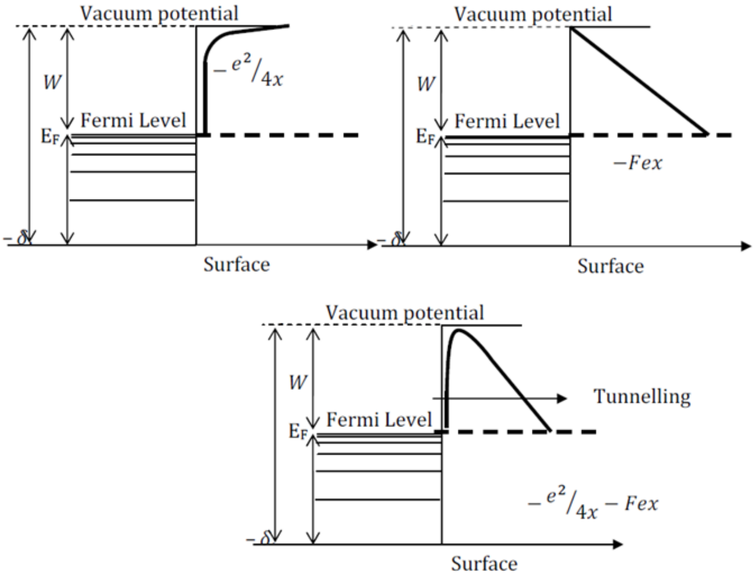

Figure 1.5: Schematic of potential barrier at conductor surface. Top and left shows the image potential effect while top and right show the potential due to an applied electric field. Bottom shows the result of the combination of these effects.

$$I = 1.54 \times 10^{-6} \frac{\beta^2 V^2 A}{\Phi(t(y))^2} \exp\left[-6.83 \times 10^9 \frac{\Phi^{\frac{3}{2}}}{\beta V} v(y)\right] \tag{1.1}$$

The field emission quality of a given sample is determined by its turn on voltage, the voltage at which field electron emission begins to occur, and its geometric factor β, a geometric factor relating to the local electric field experienced by the emitting tips compared to the average field expected based on the applied voltage and sample/anode separation. Samples with low turn on voltages and high β factors along with uniform emission from all points over the sample are desirable for field emission applications

1.6 Thesis outline

This thesis describes the growth and characterisation of ZnO nanowire arrays with various morphological features such as nanowire height, separation, etc. The methods used to produce and characterise these arrays are described in detail. The thesis begins by presenting work demonstrating the use and outcomes of a number of deposition techniques to deposit ZnO. Particular attention is then paid to the spatial ordering of ZnO nanowire arrays, and this in effect is the core of the work presented here. The thesis ends with an examination of the field emission properties of ZnO nanowire arrays produced using the techniques described in earlier chapters. The contents of each chapter are as follows:

1.6.1 Chapter 1: Introduction

This chapter provides a brief discussion of the material properties of ZnO and of ZnO nanowires and growth techniques, along with some of the motivations for the work presented in this thesis.

1.6.2 Chapter 2: Experimental techniques

Chapter 2 describes the various experimental techniques used throughout this thesis. It does not attempt to assess the results or merits of any particular method at this stage, but instead rather describes each technique, be it a deposition or characterisation technique, and how it was carried out.

1.6.3 Chapter 3: Deposition techniques

In this chapter the techniques used to deposit both ZnO thin films and nanowire arrays are discussed in detail along with experimental results of each technique.

1.6.4 Chapter 4: Nanosphere lithography

Chapter 4 describes in detail the use of NSL to create spatially ordered arrays of ZnO nanowires. Two distinct NSL patterning techniques which were successfully implemented are discussed. This chapter demonstrates that not only can array inter-wire spacing be controlled using this technique but, by altering the nanosphere diameter, arrays of nanowires of any desired spacing may be achieved. When combined with deposition techniques such as CBD and CTR-VPT, quite precise control over array morphology may be achieved.

1.6.5 Chapter 5: Field Emission

This chapter describes the characterisation by field emission of samples produced using the methods outlined in previous chapters. *I-V* data is captured and analysed from NSL samples produced with 4 different inter-wire spacings. Samples produced by both CTR-VPT and CBD techniques are examined in this way. Information on the spatial distribution of emission is also gathered through the use of phosphor coated anodes, allowing for a discussion not only of emission efficiency but also of emission uniformity.

1.6.6 Chapter 6: Conclusions and outlook

Finally, the last chapter concludes with some general discussion and conclusions based on the results presented in this thesis and gives some perspectives on future research which remains to be carried out and which would be a useful continuation of the work presented here.

1.7 References

1. Ozgur, U., et al., *A comprehensive review of ZnO materials and devices.* Journal of Applied Physics, 2005. **98**(4): p. 041301-103.

2. Hofstetter, D., et al., *Demonstration of an ultraviolet ZnO-based optically pumped third order distributed feedback laser.* Applied Physics Letters, 2007. **91**(11): p. 111108-3.

3. Lee, C.J., et al., *Field emission from well-aligned zinc oxide nanowires grown at low temperature.* Applied Physics Letters, 2002. **81**(19): p. 3648-3650.

4. Huang, M.H., et al., *Room-Temperature Ultraviolet Nanowire Nanolasers.* Science, 2001. **292**(5523): p. 1897-1899.

5. Rajendra Kumar, R.T., et al., *Control of ZnO nanorod array density by Zn supersaturation variation and effects on field emission.* Nanotechnology, 2007. **18**(21) 215704.

6. Tsung-Yen, T., et al., *The fabrication of a carbon nanotube array using a catalyst-poisoning layer in the inverse nano-sphere lithography method.* Nanotechnology, 2009. **20**(30): p. 305303.

7. Liu, D.F., et al., *A simple route to scalable fabrication of perfectly ordered ZnO nanorod arrays.* Nanotechnology, 2007. **18**(40): p. 405303.

8. Zhang, X., et al., *Synthesis of large-scale periodic ZnO nanorod arrays and its blue-shift of UV luminescence.* Journal of Materials Chemistry, 2009. **19**(7): p. 962-969.

9. Fan, H.J., et al., *Well-ordered ZnO nanowire arrays on GaN substrate fabricated via nanosphere lithography.* Journal of Crystal Growth, 2006. **287**(1): p. 34-38.

10. Cheng, C., et al., *High-Quality ZnO Nanowire Arrays Directly Fabricated from Photoresists.* ACS Nano, 2008. **3**(1): p. 53-58.

11. Kim, T.-U., et al., *Creation of Nanoscale Two-Dimensional Patterns of ZnO Nanorods using Laser Interference Lithography Followed by Hydrothermal Synthesis at 90 °C.* Crystal Growth & Design, 2010. **10**(10): p. 4256-4261.

12. Wei, Y., et al., *Wafer-Scale High-Throughput Ordered Growth of Vertically Aligned ZnO Nanowire Arrays.* Nano Letters, 2010. **10**(9): p. 3414-3419.

13. Kim, B.-J., et al., *Fabrication of GaN nanorods by inductively coupled plasma etching via* SiO_2 *nanosphere lithography.* Thin Solid Films, 2009. **517**(14): p. 3859-3861.

14. Madaria, A.R., et al., *Toward Optimized Light Utilization in Nanowire Arrays Using Scalable Nanosphere Lithography and Selected Area Growth.* Nano Letters, 2012. **12**(6): p. 2839-2845.

15. Frommhold, A., A.P.G. Robinson, and E. Tarte, *High aspect ratio silicon and polyimide nanopillars by combination of nanosphere lithography and intermediate mask pattern transfer.* Microelectronic Engineering, 2012. **99**(0): p. 43-49.

16. Choi, W.B., et al., *Fully sealed, high-brightness carbon-nanotube field-emission display.* Applied Physics Letters, 1999. **75**(20): p. 3129-3131.

17. Wang, Q.H., et al., *A nanotube-based field-emission flat panel display.* Applied Physics Letters, 1998. **72**(22): p. 2912-2913.

18. Fang, X., et al., *Inorganic semiconductor nanostructures and their field-emission applications.* Journal of Materials Chemistry, 2008. **18**(5): p. 509-522.

19. Jagadish, C. and S.J. Pearton, *Zinc oxide bulk, thin films and nanostructures: processing, properties and applications* 2006, Amsterdam, Oxford: Elsevier.

20. Ashrafi, A. and C. Jagadish, *Review of zincblende ZnO: Stability of metastable ZnO phases.* Journal of Applied Physics, 2007. **102**(7): p. 071101-12.

21. Jaffe, J.E. and A.C. Hess, *Hartree-Fock study of phase changes in ZnO at high pressure.* Physical Review B, 1993. **48**(11): p. 7903-7909.

22. Liu, H., J.S. Tse, and H.K. Mao, *Stability of rocksalt phase of zinc oxide under strong compression: Synchrotron x-ray diffraction experiments and first-principles calculation studies.* Journal of Applied Physics, 2006. **100**(9): p. 093509-5.

23. *Wurtzite crystal structure,* Wikipedia.org, article: Zinc Oxide, accessed 25th Feb 2013.

24. Desgreniers, S., *High-density phases of ZnO: Structural and compressive parameters.* Physical Review B, 1998. **58**(21): p. 14102-14105.

25. Aggarwal, R., et al., *Semipolar r-plane ZnO films on Si(100) substrates: Thin film epitaxy and optical properties.* Journal of Applied Physics, 2010. **107**(11): p. 113530-6.

26. Govender, K., et al., *Understanding the factors that govern the deposition and morphology of thin films of ZnO from aqueous solution.* Journal of Materials Chemistry, 2004. **14**(16): p. 2575-2591.

27. Hu, J.Q. and Y. Bando, *Growth and optical properties of single-crystal tubular ZnO whiskers.* Applied Physics Letters, 2003. **82**(9): p. 1401-1403.

28. Li, W.-J., et al., *Growth mechanism and growth habit of oxide crystals.* Journal of Crystal Growth, 1999. **203**(1–2): p. 186-196.

29. Wang, Z.L., X.Y. Kong, and J.M. Zuo, *Induced Growth of Asymmetric Nanocantilever Arrays on Polar Surfaces.* Physical Review Letters, 2003. **91**(18): p. 185502.

30. Pan, Z.W., Z.R. Dai, and Z.L. Wang, *Nanobelts of Semiconducting Oxides.* Science, 2001. **291**(5510): p. 1947-1949.

31. Kong, X.Y., et al., *Single-Crystal Nanorings Formed by Epitaxial Self-Coiling of Polar Nanobelts.* Science, 2004. **303**(5662): p. 1348-1351.

32. Zhang, S.B., S.H. Wei, and A. Zunger, *d-band excitations in II-VI semiconductors: A broken-symmetry approach to the core hole.* Physical Review B, 1995. **52**(19): p. 13975-13982.

33. Schröer, P., P. Krüger, and J. Pollmann, *First-principles calculation of the electronic structure of the wurtzite semiconductors ZnO and ZnS.* Physical Review B, 1993. **47**(12): p. 6971-6980.

34. Vogel, D., P. Krüger, and J. Pollmann, *Ab initio electronic-structure calculations for II-VI semiconductors using self-interaction-corrected pseudopotentials.* Physical Review B, 1995. **52**(20): p. R14316-R14319.

35. Wei, S.H. and A. Zunger, *Role of metal d states in II-VI semiconductors.* Physical Review B, 1988. **37**(15): p. 8958-8981.

36. Schleife, A., et al., *First-principles study of ground- and excited-state properties of MgO, ZnO, and CdO polymorphs.* Physical Review B, 2006. **73**(24): p. 245212.

37. Preston, A.R.H., et al., *Band structure of ZnO from resonant x-ray emission spectroscopy.* Physical Review B, 2008. **78**(15): p. 155114.

38. Janotti, A., D. Segev, and C.G. Van de Walle, *Effects of cation d states on the structural and electronic properties of III-nitride and II-oxide wide-band-gap semiconductors.* Physical Review B, 2006. **74**(4): p. 045202.

39. Klingshirn, C., *ZnO: From basics towards applications.* physica status solidi (b), 2007. **244**(9): p. 3027-3073.

40. Look, D.C., et al., *Electrical properties of bulk ZnO.* Solid State Communications, 1998. **105**(6): p. 399-401.

41. Vanheusden, K., et al., *Correlation between photoluminescence and oxygen vacancies in ZnO phosphors.* Applied Physics Letters, 1996. **68**(3): p. 403-405.

42. Janotti, A. and C.G. Van de Walle, *Native point defects in ZnO.* Physical Review B, 2007. **76**(16): p. 165202.

43. Van de Walle, C.G., *Defect analysis and engineering in ZnO.* Physica B: Condensed Matter, 2001. **308–310**(0): p. 899-903.

44. Klingshirn, C.F., et al., *Zinc Oxide: from fundamental properties towards novel applications*. Springer series in materials science, 2010: Springer.

45. Kim, J.B., et al., *Cu-doped ZnO-based p–n hetero-junction light emitting diode.* Semiconductor Science and Technology, 2008. **23**(9): p. 095004.

46. Park, C.H., S.B. Zhang, and S.-H. Wei, *Origin of p-type doping difficulty in ZnO: The impurity perspective.* Physical Review B, 2002. **66**(7): p. 073202.

47. Ryu, Y.R., T.S. Lee, and H.W. White, *Properties of arsenic-doped p-type ZnO grown by hybrid beam deposition.* Applied Physics Letters, 2003. **83**(1): p. 87-89.

48. Xiu, F.X., et al., *High-mobility Sb-doped p-type ZnO by molecular-beam epitaxy.* Applied Physics Letters, 2005. **87**(15): p. 152101-3.

49. Look, D.C., et al., *Characterization of homoepitaxial p-type ZnO grown by molecular beam epitaxy.* Applied Physics Letters, 2002. **81**(10): p. 1830-1832.

50. Joseph, M., H. Tabata, and T. Kawai, *p-Type Electrical Conduction in ZnO Thin Films by Ga and N Codoping.* Japanese Journal of Applied Physics. 1999 **38**: p. L1205.

51. Morkoc, H. and U. Ozgur, *Zinc Oxide: Fundamentals, Materials and Device Technology*2009: WILEY-VCH Verlag GmbH.

52. Afzaal, M., M.A. Malik, and P. O'Brien, *Preparation of zinc containing materials.* New Journal of Chemistry, 2007. **31**(12): p. 2029-2040.

53. Kakiuchi, K., et al., *Fabrication of mesoporous ZnO nanosheets from precursor templates grown in aqueous solutions.* Journal of Sol-Gel Science and Technology, 2006. **39**(1): p. 63-72.

54. Greene, L.E., et al., *General route to vertical ZnO nanowire arrays using textured ZnO seeds.* Nano Letters, 2005. **5**(7): p. 1231-1236.

55. Vayssieres, L., et al., *Purpose-Built Anisotropic Metal Oxide Material: 3D Highly Oriented Microrod Array of ZnO.* The Journal of Physical Chemistry B, 2001. **105**(17): p. 3350-3352.

56. Ashfold, M.N.R., et al., *The kinetics of the hydrothermal growth of ZnO nanostructures.* Thin Solid Films, 2007. **515**(24): p. 8679-8683.

57. Lokhande, C.D., et al., *CBD grown ZnO-based gas sensors and dye-sensitized solar cells.* Journal of Alloys and Compounds, 2009. **475**(1–2): p. 304-311.

58. Saito, M. and S. Fujihara, *Large photocurrent generation in dye-sensitized ZnO solar cells.* Energy & Environmental Science, 2008. **1**(2): p. 280-283.

59. Chu, D., et al., *Formation and Photocatalytic Application of ZnO Nanotubes Using Aqueous Solution.* Langmuir, 2009. **26**(4): p. 2811-2815.

60. Peterson, R.B., C.L. Fields, and B.A. Gregg, *Epitaxial Chemical Deposition of ZnO Nanocolumns from NaOH Solutions.* Langmuir, 2004. **20**(12): p. 5114-5118.

61. Kokotov, M., A. Biller, and G. Hodes, *Reproducible Chemical Bath Deposition of ZnO by a One-Step Method: The Importance of "Contaminants" in Nucleation.* Chemistry of Materials, 2008. **20**(14): p. 4542-4544.

62. Kokotov, M. and G. Hodes, *Reliable chemical bath deposition of ZnO films with controllable morphology from ethanolamine-based solutions using* $KMnO_4$ *substrate activation.* Journal of Materials Chemistry, 2009. **19**(23): p. 3847-3854.

63. Wang, M., et al., *Controlled Crystal Growth and Crystallite Orientation in ZnO Films/Nanorods Prepared by Chemical Bath Deposition: Effect of Solvent.* Crystal Growth & Design, 2008. **8**(2): p. 501-506.

64. Hosono, E., S. Fujihara, and T. Kimura *Low-Temperature Deposition of Nanocrystalline ZnO Phosphor Films from Neutral Ethanolic Zinc Acetate Solutions in the Absence of Base.* Electrochemical and Solid-State Letters, 2004. **7**(4): p. C49-C51.

65. Hosono, E., et al., *Growth of layered basic zinc acetate in methanolic solutions and its pyrolytic transformation into porous zinc oxide films.* Journal of colloid and interface science, 2004. **272**(2): p. 391-398.

66. Doggett, B., et al., *Electrical characterisation of phosphorus-doped ZnO thin films grown by pulsed laser deposition.* Superlattices and Microstructures, 2007. **42**(1–6): p. 74-78.

67. Zúñiga-Pérez, J., et al., *Ordered growth of tilted ZnO nanowires: morphological, structural and optical characterization.* Nanotechnology, 2007. **18**(19): p. 195303.

68. Sun, Y., G.M. Fuge, and M.N.R. Ashfold, *Growth mechanisms for ZnO nanorods formed by pulsed laser deposition.* Superlattices and Microstructures, 2006. **39**(1–4): p. 33-40.

69. Garry, S., et al., *Control of ZnO nanowire arrays by nanosphere lithography (NSL) on laser-produced ZnO substrates.* Applied Surface Science, 2011. **257**(12): p. 5159-5162.

70. Baxter, J.B. and E.S. Aydil, *Metallorganic Chemical Vapor Deposition of ZnO Nanowires from Zinc Acetylacetonate and Oxygen.* Journal of The Electrochemical Society, 2009. **156**(1): p. H52-H58.

71. Xu, W.Z., et al., *ZnO light-emitting diode grown by plasma-assisted metal organic chemical vapor deposition.* Applied Physics Letters, 2006. **88**(17): p. 173506-3.

72. Singh, P., et al., *ZnO nanocrystalline powder synthesized by ultrasonic mist-chemical vapour deposition.* Optical Materials, 2008. **30**(8): p. 1316-1322.

73. Liu, X., et al., *Growth mechanism and properties of ZnO nanorods synthesized by plasma-enhanced chemical vapor deposition.* Journal of Applied Physics, 2004. **95**(6): p. 3141-3147.

74. Gruber, T., C. Kirchner, and A. Waag, *MOCVD Growth of ZnO on Different Substrate Materials.* physica status solidi (b), 2002. **229**(2): p. 841-844.

75. Bakin, A., et al., *Vapour phase transport growth of ZnO layers and nanostructures.* Superlattices and Microstructures, 2007. **42**(1–6): p. 33-39.

76. Biswas, M., E. McGlynn, and M.O. Henry, *Carbothermal reduction growth of ZnO nanostructures on sapphire—comparisons between graphite and activated charcoal powders.* Microelectronics Journal, 2009. **40**(2): p. 259-261.

77. Li, C., et al., *Effect of substrate temperature on the growth and photoluminescence properties of vertically aligned ZnO nanostructures.* Journal of Crystal Growth, 2006. **292**(1): p. 19-25.

78. Yang, P., et al., *Controlled Growth of ZnO Nanowires and Their Optical Properties.* Advanced Functional Materials, 2002. **12**(5): p. 323-331.

79. Yao, L., et al., *Morphology-dependent field emission properties and wetting behavior of ZnO nanowire arrays.* Nanoscale Research Letters, 2011. **6**(1): p. 74.

80. Zhu, Y.W., et al., *Efficient field emission from ZnO nanoneedle arrays.* Applied Physics Letters, 2003. **83**(1): p. 144-146.

81. Qian, X., et al., *Effect of Aspect Ratio on Field Emission Properties of ZnO Nanorod Arrays.* Nanoscale Research Letters, 2008. **3**(8): p. 303 - 307.

82. Gomer, R., *Field Emission and Field Ionisation*1993: American Vacuum Society Classics.

83. Carey, J.D., *Engineering the next generation of large-area displays: prospects and pitfalls.* Philosophical Transactions of the Royal Society of London. Series A: Mathematical, Physical and Engineering Sciences, 2003. **361**(1813): p. 2891-2907.

84. Wang, S., et al., *A carbon nanotube field emission multipixel x-ray array source for microradiotherapy application.* Applied Physics Letters, 2011. **98**(21): p. 213701-3.

85. Silva, S.R.P., et al., *Electron field emission from carbon-based materials.* Thin Solid Films, 2005. **482**(1–2): p. 79-85.

86. Fowler, R.H. and L. Nordheim, *Electron Emission in Intense Electric Fields.* Proceedings of the Royal Society of London. Series A, 1928. **119**(781): p. 173-181.

Chapter 2: Experimental techniques

2.1 Introduction

This chapter describes the experimental methods used to carry out the work described in this thesis. A brief discussion of the techniques and experimental procedures used is given. In later chapters the techniques described here will be discussed in more detail where appropriate and the results obtained will be presented. This chapter shows the steps required to deposit arrays of ZnO nanowires, both spatially ordered and disordered, onto bare substrates (typically silicon wafers) with the endpoint of this work being the discussion on the effects of spatial ordering and morphology on Field Emission (FE) characteristics, as well as giving a description of the main characterisation methods used. The deposition of arrays of ZnO nanowires is a multi-step process, substrates must initially be coated with a ZnO buffer layer, patterned using a lithographic technique, and finally have nanowires grown on the patterned buffer layers. Reasonably low cost techniques are preferred for this work over more expensive lithographic techniques, and as such spatial control of nanowire growth was achieved using a Nanosphere Lithography (NSL) technique that provides high levels of control over array morphology and is readily reproducible and inexpensive.

There are numerous methods for growing ZnO nanowires, all of which involve the production and transport of the source species to the substrate and incorporation of that material into a nanowire. The differences in growth methods lie both in the method of generating the source species and the means of transporting these species to the substrate. This thesis uses three methods for the deposition of ZnO materials, Carbothermal Reduction Vapour Phase Transport (CTR-VPT), Chemical Bath Deposition (CBD), and Pulsed Laser Deposition (PLD). While nanowires may be grown using the PLD technique [1, 2], the present work utilises it only for the deposition of ZnO buffer layers, on which nanowires are subsequently grown using CBD or CTR-VPT. CBD has been used to both produce the underlying ZnO buffer layer and also for subsequent nanowire growth, while CTR-VPT was used solely for the growth of nanowires. A variety of characterisation techniques are used, including Scanning Electron Microscopy (SEM), Field Emission Scanning Electron Microscopy (FE-SEM), X-Ray Diffraction (XRD), Field Emission (FE), and field emission imaging (FEI). Chapter 3 describes in more detail the growth techniques used and resulting depositions, chapter 4 outlines the use of NSL as a patterning technique and describes its use as a conventional shadow lithographic mask and its use in implementing a secondary deposition mask, controlling the spatial density of nanowire deposition while maintaining excellent crystal quality. Chapter 5 is dedicated to characterisation by field emission and discussion regarding the impact of factors such as crystal quality, nanowire morphology, and spatial density on both the FE efficiency and uniformity.

2.2 Substrate preparation

The majority of samples produced in this work were grown on silicon wafers, with a small number grown on sapphire. Phosphorous doped, *n*-type, Si with (111) or (100) surface orientation was used. The decision to use silicon was made as it is compatible with the high temperatures required for deposition techniques such as

PLD and CTR-VPT, is readily available and inexpensive. It is also compatible with visualisation by SEM, and is a good candidate for characterisation by field emission since it provides a conductive path through the sample. Sapphire (Al_2O_3) can also be used for CTR-VPT depositions and has the benefit of being closely lattice matched to ZnO, naturally yielding vertically aligned growth [3-5], however it lacks the required electrical conductivity required for it to be a candidate material for use as a substrate in this work, in addition to being more expensive than Si. Si wafers were cleaved into individual samples, typically 1 cm^2 (1 cm x 1 cm) or 2 cm^2 (1 cm x 2 cm). 1 cm^2 is the minimum desired size for characterisation by FE and was the predominant sample sized used. For this work samples of area 2 cm^2 were grown and then cleaved into two identical 1 cm^2 samples so that one may be characterised by FE, a destructive technique, while leaving one sample with identical morphology intact for further characterisation such as XRD, SEM, TEM etc. Once cleaved to the desired size, the substrates were blown under a stream of nitrogen for several seconds to remove any silicon fragments remaining on the sample after cleaving. Before use, samples are cleaned by sonication in acetone for ten minutes, followed by rinsing in fresh acetone and then sonicated in absolute ethanol for ten minutes. Finally the samples are rinsed in ethanol and dried under a nitrogen stream. No attempt was made to remove the native oxide layer of the silicon and our results do not depend on the exact Si wafer orientation used ((111) or (100)), due to the ubiquitous SiO_2 present in all cases on the substrate.

2.3 Seed layer preparation

ZnO will not readily deposit onto bare Si/SiO_2 using either the CTR-VPT or CBD techniques and for this reason a seed layer consisting of a thin layer of ZnO must be deposited in order to provide initial seed or nucleation sites for ZnO buffer layer growth and subsequent nanowire deposition. Seed layers were prepared using the technique proposed by Greene and Law et al. [6, 7] from a zinc acetate solution. A 5 mM zinc acetate solution is prepared by dissolving zinc acetate dihydrate (99%) in absolute ethanol (99.9%). This process is heavily influenced by the presence of water and as such it is important that absolute (anhydrous) ethanol is used. The solution is then sonicated for up to 1 hour, until the zinc acetate has completely dissolved. This solution is then drop coated onto the cleaned Si/SiO_2 substrate at a rate of 3.5 µl per cm^2. The drop is allowed to spread across the substrate and is left for 20 seconds. After this time has elapsed, the substrate is thoroughly rinsed in absolute ethanol and is dried gently under a nitrogen stream such that remaining ethanol is pushed off the substrate rather than dried so as to prevent residues on the substrate. This procedure is typically repeated a further four times, however relative humidity plays a vital role in this process and during times of low humidity (< 20 %) this step may need to be repeated up to eight times. The ingress of water vapour causes a transformation of the zinc salt to zinc hydroxide, which settles onto the substrate. Once the substrate has been coated, it is annealed at 350 °C for 30 minutes, which decomposes the residual zinc hydroxide into platelet-like zinc oxide seed particles which lie with their basal planes parallel to the substrate surface, giving a quite well textured seed layer [8].

However, these seed layers are not suitable for high temperature CTR-VPT growths in an oxygen-rich environment due to coalescence of seeds which reduces seed density and to substrate coverage and also the growth of SiO_2 which causes deterioration in seed layer texture and which can overgrow seed particles and thus remove them as possible nucleation sites. For these reasons in all cases a subsequent low temperature CBD growth of nanorods on the seed layers is undertaken, either as a final step to nanorod formation itself, or as an intermediate step before subsequent CTR-VPT nanowire growth. The CBD-grown nanorods are much more stable in the high temperature, oxygen-rich CTR-VPT growth environment [8, 9].

2.4 Chemical bath deposition

Deposition of ZnO buffer layers and nanowires by chemical bath deposition was achieved using three different CBD techniques. Firstly, ZnO was deposited using aqueous solutions of zinc nitrate and hexamine (HMT). Equimolar solutions of zinc nitrate (99%) and HMT (99.5%) are used. In all cases the concentration of both the zinc nitrate and HMT was 25 mM. The second technique used was the direct thermal decomposition of zinc acetate in solution. Aqueous solutions of zinc acetate were heated, resulting in the formation of partially soluble zinc hydroxide due to the loss of the acetate anion. The zinc hydroxide produced then goes on to form zinc oxide. The third CBD method used involved sodium hydroxide (NaOH, 99%) and zinc nitrate. These create a metastable $Zn(OH)_4^{-2}$ solution from which ZnO is deposited. This technique has the advantage that, unlike the first two, there are no other precipitates or debris formed during the reaction.

The setup used in all three cases is the same; a schematic is shown in figure 2.1 below. A hotplate is used as the source of heat while all reactions are performed in a laboratory beaker. The reaction solutions are stirred using a PTFE coated magnetic stirring bar while the reaction temperatures are monitored using a digital temperature probe.

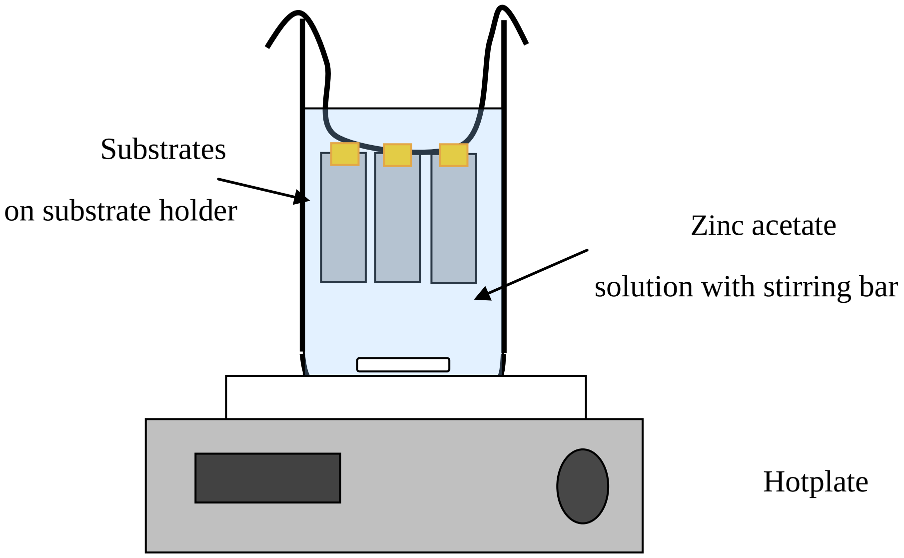

Figure 2.1: Schematic representation of equipment used for CBD deposition of ZnO.

2.4.1 HMT based reaction

Zinc nitrate and HMT are dissolved in deionised water (DI-H_2O) at a concentration of 25 mM by stirring. This equates to 7.4 mg zinc nitrate and 3.5 mg HMT per ml of solution. The total volume of reaction solution used was around 100 ml, chosen due to the size of the reaction vessel. The seeded substrate is submerged in the solution and heated to 90 °C and stirred continuously. The reaction time is 30 minutes, after which the sample is removed from the solution and rinsed thoroughly in DI-H_2O and dried under a stream of nitrogen.

2.4.2 Acetate based reaction

Zinc acetate is dissolved in DI-H_2O to create a 25 mM solution. 5.28 mg of zinc acetate is required per ml of solution. Typically around 100 ml of solution was used as this was convenient for the size of beaker used. The seeded substrates are submerged in the solution and heated to approximately 65 °C. Deposition of buffer layers of reasonable thickness may take up to three hours with this technique. Due to formation of precipitates during this reaction, the sample is removed after 90 minutes and rinsed with DI-H2O and dried. The solution is discarded and the substrate is submerged again into a freshly prepared solution for a further 90 minutes. Following deposition the substrate is again rinsed with DI-H_2O and allowed to dry at room temperature.

2.4.3 NaOH based reaction

Due to the metastable nature of the NaOH reaction it is important that the equipment used is free of any zinc oxide residue. The presence of zinc oxide in the solution before optimal conditions are met will result in the formation of precipitates in the solution by homogenous nucleation. To ensure that all zinc oxide has been removed from equipment, it is washed in a dilute sulphuric acid (H_2SO_4), followed by thorough rinse with copious amounts of DI-H_2O. H_2SO_4 in the presence of water reacts with zinc oxide to produce zinc sulphate ($ZnSO_4$), which is water soluble and is easily removed by rinsing. As with the other two CBD methods the reaction volume was typically 100 ml, once again this is a choice of volume determined solely by equipment size and any change in the volume used caused no observable differences in the samples produced. An aqueous solution of NaOH is prepared at a concentration of 0.8 mM and in a second beaker an aqueous solution of zinc nitrate is prepared at a concentration of 20 mM. Once the two solutions are completely dissolved, the zinc nitrate solution is slowly added to the NaOH solution under constant stirring. Stirring is important as it fully disperses the zinc acetate throughout the NaOH solution preventing localised high concentration of zinc acetate, which would cause the precipitation of zinc hydroxide from the solution. A correctly prepared solution is completely clear and no precipitates should be formed. The concentrations in the final solution are 0.4 mM NaOH and 10 mM zinc nitrate. Unlike the other two techniques discussed the solution must be heated to the reaction temperature before the sample is submerged, as again this would cause the formation of precipitates in the solution. Once the solution is heated to 70 °C the sample is submerged with constant stirring using a magnetic stirrer bar. The temperature is kept constant for a reaction time of 30 minutes. The substrate is then removed and rinsed in DI-H_2O and allowed to dry at room temperature.

2.5 Pulsed layer deposition

Before deposition of a ZnO layer by pulsed laser deposition (PLD), a silicon wafer is cleaved into appropriate sized pieces and cleaned by sonication in acetone for ten minutes then rinsed with fresh acetone before being sonicated in absolute ethanol for a further ten minutes. The substrate is then rinsed with fresh ethanol and dried under a stream of nitrogen.

PLD deposition was performed using a custom-designed Neocera vacuum system, designed specifically for PLD, a simple schematic of which is shown in figure 2.2. The cleaned substrate is then attached to the sample mount in the PLD vacuum chamber with silver paste (SPI supplies, Silver Paste Plus). The chamber is then evacuated to ultra high vacuum (~ 5 x 10^{-8} mbar). PLD is carried out using a Continuum Powerlite Precision II Laser, this is an Nd:YAG laser with a fundamental wavelength of 1064 nm, which for PLD is frequency quadrupled using harmonic crystals to a wavelength of 266 nm. The energy output at this wavelength is approximately 150 mJ per shot, at a pulse frequency of 10 Hz with pulse duration of 6 ns. The laser is directed into the chamber and focussed onto the deposition target with a system of mirrors and lenses (all optics designed for a wavelength of 266 nm). The power output of the laser may vary slightly between depositions but the spot size is adjusted to retain a fluence of ~ 2 J•cm^{-2}. The deposition target used in all experiments was a sintered 99.999 % purity ZnO target, and the sample mount is situated 4 cm away from the target.

Before deposition takes place the sample holder is heated to a temperature of 900 °C for five minutes to further clean the surface of any remaining contaminants or residues from cleaning and handling. The temperature is then slowly ramped down to 300 °C, which is then kept constant during the deposition. A background gas pressure of 0.1 mbar of oxygen is introduced before deposition begins to ensure stoichiometric deposition. The laser is fired and ablates the ZnO target which creates a plume of high energy particles. This plume moves predominantly normal to the target surface and is incident normally on the sample. The sample mount is rotated during growth so that a uniform layer is deposited across the entire sample area, while the target is rotated to ensure the same spot is not constantly being ablated. The laser is pulsed 10,000 times over the course of the deposition. Once the deposition is over, the sample mount temperature is increased from 300 °C to 700 °C to anneal the ZnO layer. After five minutes the temperature is slowly ramped down to room temperature. A low ramp rate is necessary here to reduce the effect of thermal shock, which would otherwise result in the formation of cracks in the newly deposited ZnO layer.

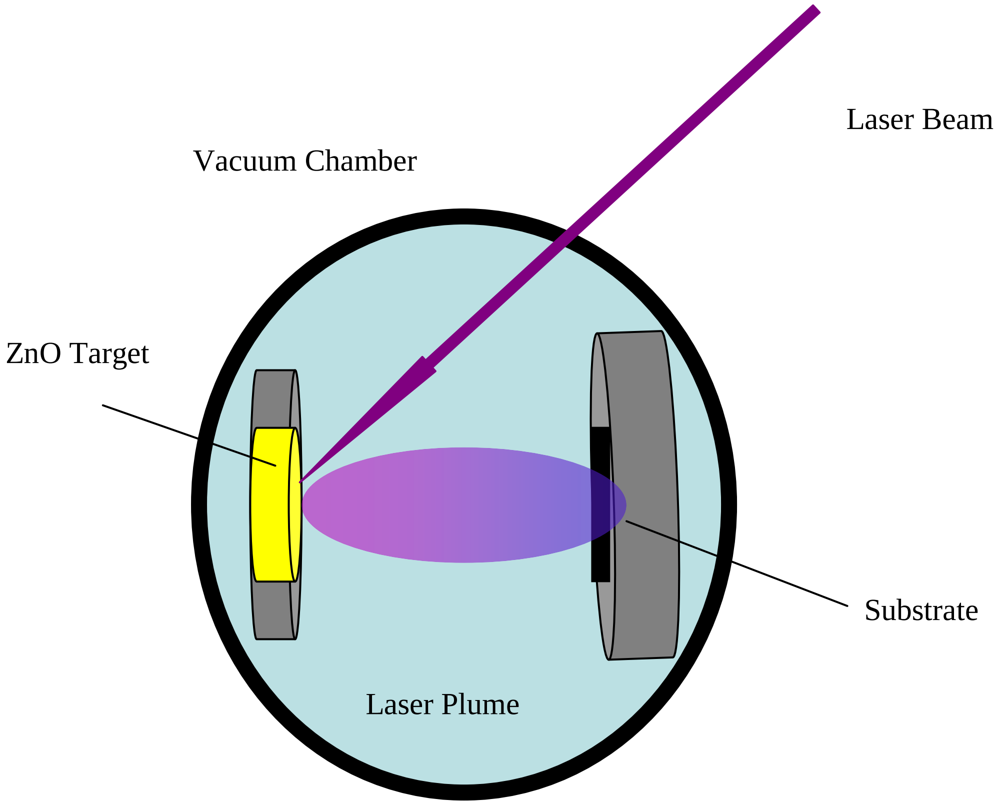

Figure 2.2: Schematic of Pulsed Laser Deposition experimental set-up

2.6 Carbothermal reduction vapour phase transport

Nanowires grown by carbothermal reduction vapour phase transport (CTR-VPT) were typically grown on Si substrates with a ZnO buffer layer but also on Si substrates coated with an Au catalyst layer. In the first instance the bare Si/SiO_2 substrate will not readily nucleate ZnO, so direct deposition thereon by various techniques is not possible. Furthermore, because Si is non-lattice matched, any ZnO nanowire deposition which does occur (e.g. by PLD) on it without such a buffer layer will not be aligned and will result in disordered unaligned growth. The role of the ZnO buffer layer during these growths is both to provide nucleation sites to initiate growth and also to provide a crystallographically textured substrate for vertically aligned nanowire growth. The role of the Au catalyst layer, as with the ZnO buffer layer, is to provide suitable nucleation sites for deposition, however growth on Si/SiO_2 using Au catalyst will still tend to be not aligned due to the absence of lattice-matching to the underlying substrate and the absence of a crystallographically textured buffer layer. All CTR-VPT depositions were carried out in a quartz tube of length 115 cm, internal diameter 37 mm, positioned in a single temperature zone horizontal tube furnace (Lenton Thermal Designs). Argon (Air Products, Argon Premier, 99.9992%) is used as a carrier gas in all cases to assist in the transfer of zinc species to the substrate. the argon used is of high purity and flow is controlled using a mass flow controller (MFC: Analyt GFC 17). A schematic of the setup is shown in figure 2.3.

The Ar flow rate is an important variable that needs to be kept constant. The effects of changing the gas flow are discussed in detail in chapter 3. In order to ensure the flow rate through the system is 90 sccm the gas flow is measured using a graduated cylinder and a timer periodically to calibrate the MFC. A schematic of the technique used is shown in figure 2.4. The time taken to displace a certain volume, typically 45 cm^3, was measured and the flow rate calculated. If any deviation from the nominal flow rate is found, it may be corrected by compensating until the correct flow is achieved (if the flow rate is consistent) or by returning the MFC to the manufacturer for calibration.

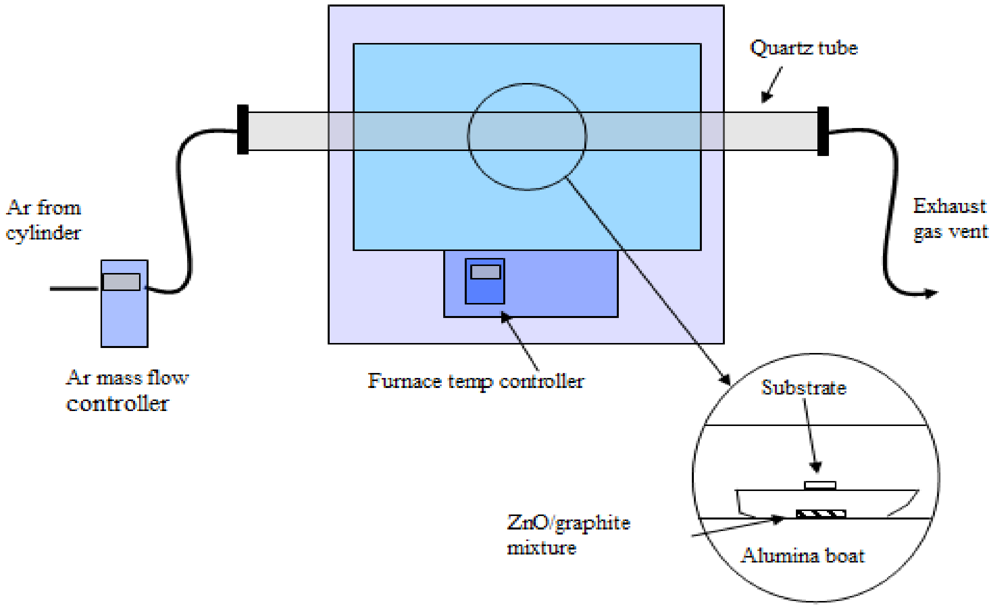

Figure 2.3: Equipment setup for CTR-VPT growth of ZnO nanowires

A number of materials may be used in VPT. These include zinc oxide and zinc metal as the zinc source, and for the case of CTR-VPT, ZnO as the Zn source and graphite, carbon black or other carbon- allotropes as the reducing agent to reduce the ZnO. For all CTR-VPT depositions described in this work, zinc oxide and graphite were the source materials used. Typically 60 mg of high purity ZnO (Alfa

Aesar, 99.9995%) and 60 mg of graphite powder (Alfa Aesar, 99.9999%) were used. The powders are thoroughly ground together using a pestle and mortar until a homogeneous mixture is obtained. This increases the contact area between the two powders, which may influence the subsequent growth. After mixing, the powders are carefully loaded into an alumina boat and spread evenly across a 2 cm length of the boat. The substrate is placed directly above the source powders on two thin strips of clean silicon which are used to support the substrate in place. The alumina boat is then loaded into the quartz tube and positioned so that the source materials and sample are located at the centre of the hot zone of the furnace. The quartz tube end caps are replaced and the tube is flushed with a flow of argon at 90 sccm for 5 – 10 minutes. After this the furnace is heated to the target reaction temperature, typically in the region of 850 °C to 950 °C while maintaining the flow of argon. For consistency the reaction time was kept to 1 hour for all depositions, this time includes the heat up period of approximately 11 minutes. After the 1 hour reaction time has elapsed, the furnace is turned off and allowed to cool to room temperature over the course of several hours. The alumina boat containing the sample is then removed.

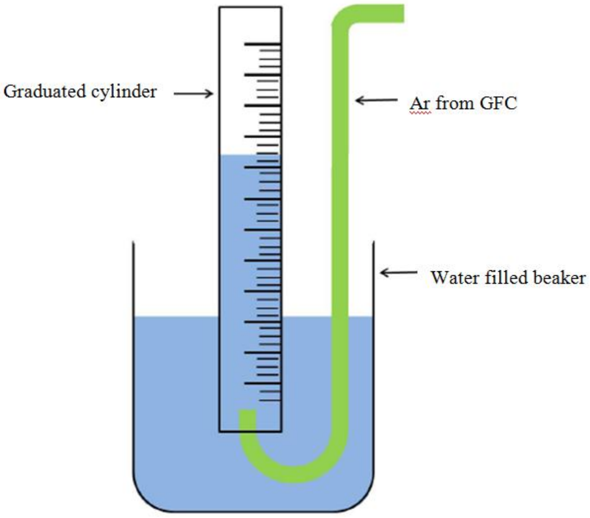

Figure 2.4: Schematic of setup used to measure gas flow rate.

2.7 Nanosphere Lithography

Nanosphere Lithography (NSL) is a patterning technique that is based on the natural tendency of some materials to self assemble into particular formations. Colloidal nanosphere monolayers are a promising route to the development of spatially ordered nanowire arrays as they provide an array of uniformly spaced spheres which may be used as a template for growth [10, 11]. In this work two separate NSL template techniques were investigated, both offering a method for the growth and spatial control of vertically aligned ZnO nanowire arrays. Both of these techniques rely on the use of hexagonally close packed arrays of such colloidal nanospheres, typically on a Si substrate coated with a ZnO buffer layer.

Three methods for the deposition of hexagonally close packed nanosphere monolayers were investigated, the first of which was a spin coating technique [12].

The second method was a drop coating [13] technique and the third was a method proposed by Rybczynski et al [14] which involves the generation of colloidal monolayers on the surface of water allowing for the easy transfer of nanosphere monolayers onto any flat wettable surface.

Once the nanosphere monolayer has been transferred to the substrate the next step is to use the monolayer as a template for the growth of nanowires. The first method investigated involves the use of Au catalyst deposited through the nanosphere monolayer, resulting in a pattern of triangular Au catalyst points on the substrate once nanospheres have been removed. The second method investigated involves the use of a secondary silica mask. The sphere covered sample is coated with silica, which covers the entire surface area except for the contact points between the nanospheres and the surface. This yields a silica honeycomb pattern which can then be used to template nanowire growth. Apart from the absence of a catalyst in the second technique the main difference in the arrays produced using these techniques is the pattern produced. As is illustrated in figure 2.5, the density of subsequent nanowire growth varies greatly between the two techniques. The silica secondary template technique results in the growth of one nanowire per sphere whereas the Au catalyst technique yields two per sphere. Furthermore, there is significant difference in the way that nanosphere monolayer defects are propagated through the growth process. When using Au catalyst, any area not shadowed by a sphere will be coated with Au and subsequently nanowire growth will take place at that point, resulting in uncontrolled growth at the location of a nanosphere vacancy or in the case of a boundary defect a line of nanowires. However, due to the inverse nature of the silica secondary mask any defects present in the nanosphere monolayer are coated with silica and are therefore not viable sites for nucleation. Defects are not propagated as uncontrolled growth but as areas of no growth.

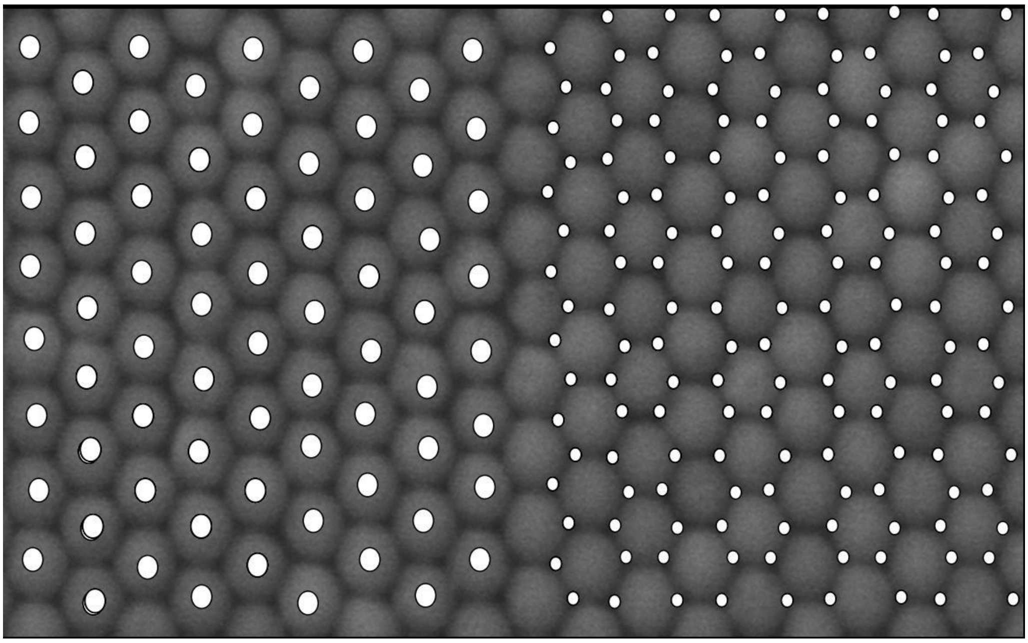

Figure 2.5: SEM image of nanosphere array with white dots inserted to show locations of potential nucleation points. The white dots on the left side mark the locations of subsequent nanowire growth using the silica secondary template method. The right shows location of growth if using the Au catalyst technique.

2.7.1 Generating colloidal monolayers

As outlined above, three methods of generating nanosphere monolayers were investigated, the first of which is a spin coating technique. Before spin coating Si substrates must be treated with a base piranha solution (3:1 ammonium hydroxide (NH_4OH) and hydrogen peroxide (H_2O_2)) to ensure that the substrate surface is hydrophilic. A dilute nanosphere solution (Thermo Fisher) is dropped onto the substrate. It is first spun at low speed (300 – 600 rpm), to spread the sphere solution across the surface area. It is then spun at high speed (2000 rpm) to remove any excess spheres and to force the formation of a close packed monolayer.

The second technique was drop-coating. The Si wafer is cleaned in a base piranha solution. A dilute solution of nanospheres (1 – 10 % by weight) in DI-H_2O is mixed in equal amounts with a solution containing 1 part in 400 of the surfactant Triton X-100 in methanol. Approximately 20 µl of this solution is dropped onto and allowed to spread across the substrate surface. This is then left to dry.

The final method of generating colloidal monolayers was self assembly on the surface of water. A low form glass crystallisation dish is filled with DI-H_2O, leaving approximately 5 mm at the top unfilled. A clean microscope slide is inserted into the water and is held in place using a retort stand. A nanosphere solution (10 % by weight in aqueous solution), containing spheres of either 500 nm or 1 µm diameter, is mixed with equal amounts of ethanol and mixed thoroughly by sonication. Typically approximately 100 µl is prepared. Using a micro-pipette 20 µl of this solution is very slowly applied to the glass slide, immediately above the water surface. The tip of the pipette is moved slowly from side to side in order to spread the nanosphere solution across the glass slide covering approximately 1 – 2 cm of the slide. Care must be taken to ensure the tip of the pipette does not come into contact with the surface of the water as this will lead to spheres being dispersed into the bulk water under the monolayer. This is repeated until enough solution has been applied to the slide for it to flow down to the water surface. When this occurs, the nanospheres disperse over the water surface. The process is continued until a large area of the water surface is covered, while leaving a clear area large enough for samples to be submerged in the water without coming in contact with the spheres. During this process the application of solution should be continuous; the nanosphere solution should not be allowed to dry on the glass slide as this causes the formation of clumps of nanospheres. The nanosphere solution may also be applied to the side of the glass dish if it has been cleaned thoroughly.

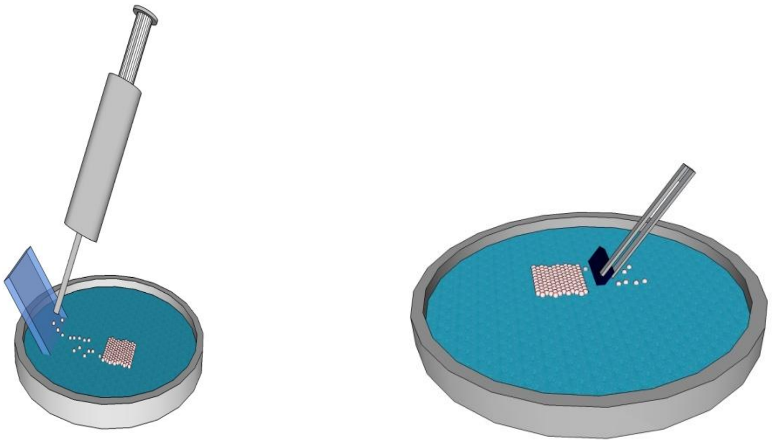

Figure 2.6: Schematic of the equipment used to obtain nanosphere monolayers on any wettable substrate. First the sphere solution is applied to the glass slide just above the water surface. Once assembled the monolayer may be transferred by lifting a substrate though a close packed area.

In order to grow the area of monolayer produced the dish may be gently tilted in order to create waves on the surface, agitating the spheres and moving them together. Large areas of monolayer may be created using this technique, in the lab scale it is limited only by the size of dish used. Monolayers of > 30 cm^2 have been produced in this way in our laboratory. Before transferring the monolayer onto the substrate, a small amount of surfactant is added to the water. The change in surface tension creates additional force between the nanospheres causing them to pack tightly. This helps ensure that the monolayer does not disperse while being transferred onto the substrate. Due to the highly periodic nature of nanosphere monolayers, the colloidal crystal exhibits strong opalescent effects when illuminated by white light, making it trivial to identify areas of high quality monolayer (using domain size as indicator of quality). Before transferring the spheres, areas of monolayer which appear cloudy (due to multilayers or spheres dispersed in the water bulk) may be remedied with the use of a Pasteur pipette. By gently flowing water underneath the monolayer these spheres may be dispersed, leaving the desired area clean. Transferring the nanosphere monolayer onto the substrate involves submerging the substrate through an area of the water surface that does not contain nanospheres and slowly positioning it underneath the nanospheres. By gently lifting the substrate through the monolayer the colloidal crystal is transferred. The substrate is then allowed to dry at room temperature. Due to the reproducible nature of this method, it was the one used in all cases for subsequent ZnO deposition.

2.8 Nanospheres as templates for growth

Due to the low melting temperature of the polystyrene spheres used, it is not possible to use them in situ as a template for CTR-VPT growth. Two techniques were investigated with the aim of achieving the growth of spatially ordered nanowire arrays by using the spheres to create a template and then removing them before growth. The first used Au catalyst to provide a pattern of Au catalyst nucleation sites for growth, while the second used a secondary silica mask to prevent growth at all but the desired areas.

2.8.1 Au catalyst assisted growth

Substrates coated with nanosphere monolayers of both 500 nm and 1 µm diameter and these substrates + monolayers were coated with Au using a thermal evaporator. The Au used was 99.999 % purity Au wire (Advent Research Materials, 1 mm diameter) cut into lengths of ~ 3 mm. One length of Au wire is sonicated in IPA for 10 minutes and rinsed with fresh IPA before being dried under a nitrogen stream. This is then placed into a molybdenum boat attached to a current source. Typically a nominal thickness of 5 – 10 nm was deposited. Before Au deposition, the substrate is placed on a sample holder, approximately 20 cm from the Au source and a shutter is moved into place between the substrate and Au source. Evaporation of the Au is begun by slowly ramping up the current to the molybdenum boat carrying the catalyst material. The shutter is kept closed initially to prevent any remaining residue on the Au wire being transferred to the substrate. When Au evaporation has begun, as shown by deposition on the side wall of the bell jar, the shutter is opened. The rate of deposition is controlled by varying the current supplied to the molybdenum boat and is monitored using a quartz crystal thickness controller. The deposition rate is kept very low, (< 1 nm per minute), in order to ensure uniform deposition. If the substrate is held perpendicular to the Au source, the area of each individual Au catalyst region in the pattern is dependent only on the size and coverage of the nanosphere monolayer. However, some control over the area of each individual Au catalyst region in the pattern deposited can be achieved by altering the angle at which the substrate is placed with respect to the Au source as described in detail in chapter 4.

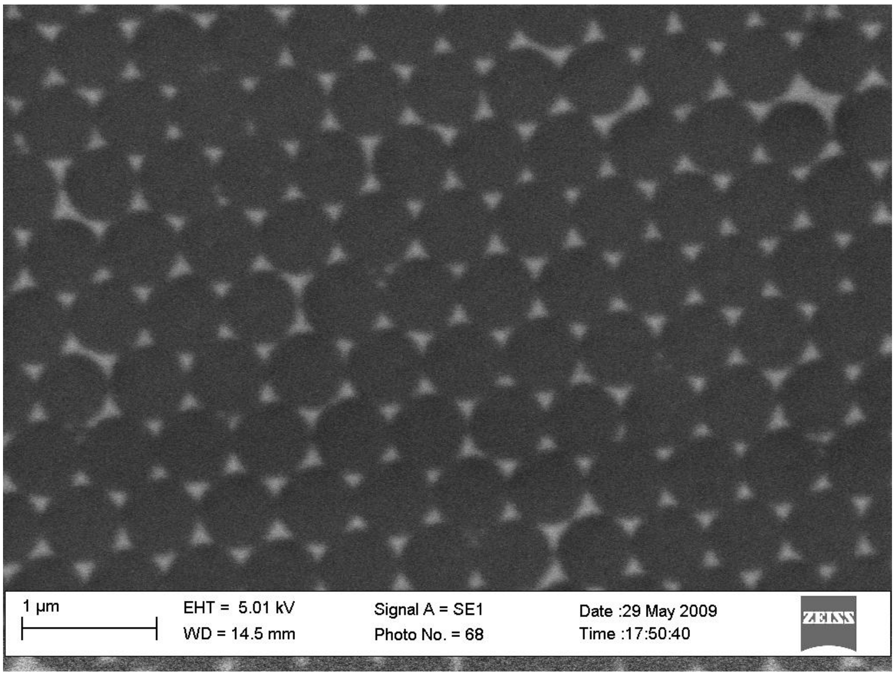

Figure 2.7: SEM image of typical triangular Au islands as deposited through a nanosphere monolayer.

After Au deposition, the nanosphere monolayer must be removed to reveal the Au catalyst pattern on the substrate. This may be achieved by physically removing the spheres by using adhesive tape to slowly peel off the monolayer. Alternatively, the substrate may be sonicated in toluene for 15 minutes to dissolve the polystyrene nanospheres. After sonication the sample must be rinsed thoroughly to remove the Au which had been deposited onto the now dissolved nanospheres. The remaining Au pattern on the substrate surface is a hexagonal array of triangular islands as shown in figure 2.7.

The substrate is then ready to be grown upon using the CTR-VPT technique described above with some slight changes to the sample positioning relative to the source powders as will be discussed in chapter 4. This technique for creating patterned arrays of Au islands works independent of choice of substrate, however there are some issues limiting its use on some substrates such as bare Si wafer. This is discussed in detail in chapter 4.

2.8.2 Silica secondary template growth

Contrasting with the use of nanospheres as a shadow mask for the deposition of catalyst material, the use of silica to create a secondary template was investigated. The choice of silica as the material for this mask was due to its ability to withstand the high temperatures required in CTR-VPT deposition. Silica templates were produced using a sol-gel process.

Silica templates are formed by depositing a silica sol-gel onto the surface of substrates. In this work only Si wafers coated with ZnO buffer layers were used but this technique is applicable to other substrate choices. This technique is based on methods proposed by Li *et al* and Wang *et al* [15, 16]. The sol is produced using a catalysed reaction of tetraethyl orthosilicate (TEOS). TEOS reacts with DI-H_2O to form silicon dioxide (SiO_2). This process is the result of two reactions, a hydrolysis reaction followed by a condensation reaction [17]. In the first reaction, shown in equation 2.1, one of the alcohol ligands with a hydroxide group. The second reaction, shown in equation 2.2, occurs when two hydrolysed TEOS molecules come into contact with each other. One hydroxide group is removed from one of the two silicon centres and also removes the hydrogen atom from the other hydroxide group forming a water molecule. The oxygen atom remaining from the broken hydroxide group then bonds with the silicon atom forming a Si – O – Si linkage.

$$Si(OC_2H_5)_4 + H_2O \rightarrow HO\text{-}Si(OC_2H_5)_3 + OC_2H_6 \qquad (2.1)$$

$$HO\text{-}Si(OC_2H_5)_3 + HO\text{-}Si(OC_2H_5)_3 \rightarrow (OC_2H_5)_3Si\text{-}O\text{-}Si(OC_2H_5)_3 + H_2O \qquad (2.2)$$

Both these reactions take place naturally between TEOS and water, but the rate of reaction is too slow to be useful. In order to perform these reactions at a more practical rate a catalyst is used. Both bases and acids may be used to catalyse these reactions. With bases, the first reaction is faster than the second, so that there is an increase of the rate of removal of the alcohol ligand. During the second reaction (2.2), the silicon centre is likely to cross link forming nanoparticles. This is the basis of the formation of silica nanospheres [18, 19]. When the reactions are catalysed by an acid, the second reaction is faster than the first one, leading to long chained polymeric silica sols.

2.8.3 Sol preparation

In this work the silica templates used were derived from acid catalysed sols. The solution is prepared by mixing 1 ml of TEOS and 1 ml of the chosen acid catalyst to 20 ml of absolute ethanol. The acid catalyst may be 0.05 M sulphuric acid (H2SO4) or 0.1 M hydrochloric acid (HCl). The choice of acid catalyst was not observed to affect the sol produced. A magnetic stirrer is then used to stir the solution for three hours. Before use, the sol is diluted with an equal amount of ethanol. Before application, the nanosphere coated substrate is placed on a hot plate at 110 °C for 30 seconds. This temperature is above the glass temperature of polystyrene and allows the spheres to deform slightly and adhere to the substrate. This prevents the nanosphere monolayer from lifting away from the substrate when the sol is applied. To create the silica template, the sol is drop-coated onto the sample (i.e. the substrate with the nanosphere monolayer thereon) and allowed to dry in air. 20 µl was applied per cm^2 of sample area. Once the sol has dried in air, the substrate is placed on a hotplate at 90 °C for 5 minutes. To remove the nanospheres, the substrate is dipped into toluene and rinsed thoroughly in DI-H_2O and then dried under a gentle stream of nitrogen. It is then necessary to densify the silica to reduce the porosity of the layer. This is achieved by annealing the substrate at 450 °C for 30 minutes in air. Heating the substrate up to the annealing temperature must be carried out gradually; at this point the silica layer is very prone to thermal shock leading to the formation of cracks or the layer peeling from the substrate. A ramp rate of < 15 °C per minute should be used. Once the silica layer has been densified, the substrate is ready to be grown upon using either the CBD or CTR-VPT techniques as described above. Densification of the silica ensures that the sample will withstand the high temperatures and high temperature ramp rates that are required for CTR-VPT deposition.

2.9 Characterisation techniques

This thesis primarily discusses the growth of ZnO nanowire arrays and the techniques used to control their morphology and spatial ordering. As such, the primary means of characterising samples prepared was the one most suited to examining nanostructured sample morphology – Scanning Electron Microscopy (SEM). In addition to SEM characterisation, techniques were used to gain information on the material properties of the samples produced such as crystal quality and nanowire alignment. In addition to these conventional techniques, in line with the end goal of this work, the FE properties of the samples produced were also examined.

In all cases samples were examined by SEM, followed by XRD in cases where the sample morphology was acceptable for FE. The following sections give an introduction to the various characterisation techniques used, with some background including their principles of operation and specific setup for the present work. Field emission was carried out with the close collaboration of a colleague, Mr. Éanna McCarthy.

2.9.1 Scanning Election Microscopy (SEM)

SEM was used extensively during this work as the feature sizes that require imaging fall into the usual range of operation of conventional SEM systems. There is a limit on the size of features that may be resolved and is related to the wavelength of light, or electron beam, used. The diffraction pattern from a feature must not significantly overlap with the pattern from another neighbouring feature. The Rayleigh criterion dictates that if the centre of the diffraction pattern from one feature overlaps with the first minimum of the pattern from another, the two features are not resolvable. Given that the feature sizes of nanostructures in this work are on the order of 10’s to 100’s of nanometres, shorter than wavelengths in the optical range, optical microscopy was ruled out as a characterisation technique. In scanning electron microscopy, a high energy beam of electrons is focussed and incident on the surface being analysed. The interaction between the incident electrons and the sample surface may be an elastic or inelastic scattering process. The different modes of interaction lead to multiple means of operation for an SEM with different information being obtained by each mode. Some modes give morphological information while other signals also carry information on the material properties of the sample being examined. The SEM system used in this work consists of two chambers under vacuum. The lower chamber may be brought to atmosphere without breaking vacuum in the other through the use of a differential pumping system with pressure limiting apertures. The top chamber is the gun column, this contains the electron source. The source may either be a hot cathode thermionic emitter, generally a tungsten filament or lanthanum hexaboride source, or a cold cathode field emission source. Below the electron gun, an anode provides additional acceleration and some focussing to the emitted electrons. As in an optical microscope, the electrons are then focussed into a beam using lenses. However unlike in an optical microscope the lenses used are not refractive, but magnetic lenses which focus the electron beam through the use of the magnetic Lorentz force. The focussed beam is then incident on the sample. Unlike optical microscopy where light is incident over large areas and then focussed to produce an image, the electron beam is raster scanned over the sample being examined. The resultant interactions and emitted electrons and photons are measured using a variety of detectors, including a secondary electron detector, a back scattered electron detector and an x-ray detector. Figure 2.8 shows a schematic of a typical SEM setup showing all the major components.

Elastically scattered collisions are those where electrons, from the SEM beam, are deflected away from the sample. Elastic interactions lead to backscattered electrons. Backscattering is very dependent on the mass of the element being examined with higher mass elements backscattering larger numbers of electrons than lower mass elements. This contrast can be used to gain information about the composition of the material under examination. Since backscattered electrons are more likely to be directed back along the beam path than at other angles, they are detected by placing a circular detector surrounding the beam path through the aperture.

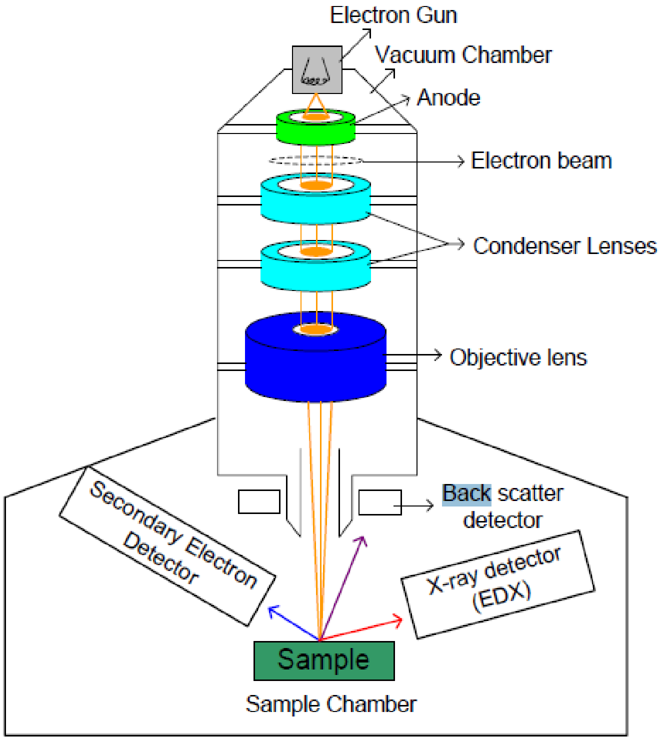

Figure 2.8: Schematic representation of a typical SEM setup

Inelastic interactions occur when electrons from the atoms on the sample are knocked out of their orbitals. These ejected electrons are known as secondary electrons, and have low energies (≤ 50 eV. The ejected secondary electrons are accelerated towards a detector which is positively biased and then detected.

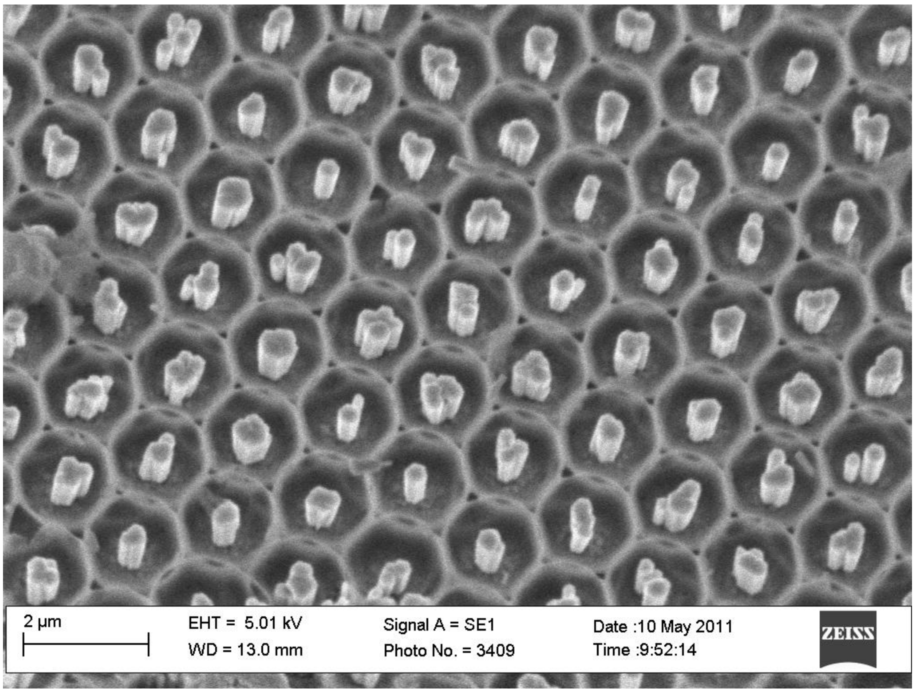

Figure 2.9: SEM image of nanowires exhibiting tilt-contrast effects.

The detected signals (from inelastically or elastically scattered electrons or other signals such as x-rays) form a digital image by collating the intensity data with the position of the electron beam on the sample. Images produced in this manner have a large depth of field and photograph like qualities. Secondary electrons are a good choice for studying morphology as their low energy means that their emission is very topography related; only electrons very near the surface can exit the sample. The number of secondary electrons emitted increases significantly as the angle of electron beam incidence is increased from the normal. This may be used to determine orientation of surfaces on the sample. The angle/contrast relationship is due to the larger exposed surface area within the interaction volume at higher angles. This contrast effect can be seen in figure 2.9, where the flat tops of each nanostructure are darker than the sides, which are observed at a much more oblique angle.

The electrons ejected during the interaction process also give rise to a second detectable signal. Some secondary electrons emitted leave behind an inner shell hole. Electrons from outer orbitals of the atoms can then combine with the hole created in the inner orbitals. The energy difference between the two orbitals is emitted in the form of x-rays. The energies of the emitted x-rays are characteristic of the binding energies of the atomic orbitals present and may be used to identify the elements present. This process is known as energy dispersive x-ray (EDX) spectroscopy and allows for the identification of the atomic species present. It may also be used to form elemental maps of the sample to determine the distribution of elements in a composite material.

Another type of electron emission may occur when an electron beam is incident on a material. The incident primary electron may collide with inner shell electrons of the sample, leaving those atoms in an ionised state. Subsequently this inner shell vacancy is filled by an electron from a higher energy level. The energy emitted from this transmission in some cases is non-radiative and result in the emission of a third electron. This type of electron emission is known as Auger emission and the electrons emitted have energies characteristic of the material under examination. Scanning Auger microscopy, similar to SEM, provides topographical information about the sample but also may provide material information due to the characteristic energies of electrons emission.

In this work, SEM characterisation was typically carried out using a Carl Zeiss EVO series SEM fitted with secondary electron, backscattered electron and EDX detectors. Additional high resolution characterisation was performed using a

Hitachi S5500 FESEM in conjunction with Dr. Brendan Twamley of the School of Chemical Sciences in DCU.

2.9.2 X-Ray Diffraction (XRD)

XRD is a technique used to gain information on the crystal structure of materials. When a beam of x-rays is incident on a crystal structure, it may either be absorbed, which is the basis of x-ray photoelectron spectroscopy, or scattered either elastically or inelastically. Inelastic scattering, known as Compton scattering, transfers some of the incident x-ray's energy to the electrons of the material being examined. In this kind of scattering there is no phase relationship between the incident and scattered x-rays and they do not interfere with each other, meaning no crystallographic information may be obtained from Compton scattering. Elastic scattering however yields partially coherent x-rays when a monochromatic beam of x-rays is incident on the sample. The partially coherent x-rays interfere with each other under certain conditions. By measuring the interference patterns produced, information on the crystallographic nature of the material may be determined. The conditions under which interference will occur are described by Bragg's law [20] as shown in equation 2.3.

$$n\lambda=2d\sin\theta \tag{2.3}$$

Where d is the interatomic distance, θ is the incident angle, λ is the x-ray wavelength and n is an integer. The crystals' structure is viewed as a series of atomic planes with scattering nodes (e.g. atoms/molecules) equally spaced along each plane as shown in figure 2.9. Incident x-rays are scattered elastically off the nodes in each atomic plane at an angle θ. As described by the Bragg equation, when the path lengths taken by scattered electrons differ by an integer multiple of the incident wavelength, constructive interference will occur. Destructive interference occurs when path length differs by half integer multiples. The right hand side of the Bragg equation shown above is simply the difference in path length taken by x-rays scattering off two adjacent atomic planes.However due to the crystal structure of some materials, there are certain reflections that do not occur. A structure factor for a given crystal structure may be calculated, which gives information on what reflections are allowed/disallowed, for example in ZnO only the (0002) and higher order reflections given by (0002*l*) are observed. A thorough description is given in reference [20].

The interference pattern (diffraction pattern or diffractogram) is normally measured by scanning a collimated monochromatic x-ray beam through an angle θ while simultaneously scanning the detector through the same angle to measure the scattered x-rays (the θ-2θ configuration) so that the atomic planes being measured are those parallel to the sample surface (the so-called symmetrical configuration). Peaks detected in this way are at angular locations where the Bragg condition is met. This allows the atomic spacing for these planes to be determined. For unaligned deposits or powder samples all the possible reflecting planes are present parallel to the surface in a certain fraction of the powder particles, so that a very rich diffractogram with many reflections is seen, whereas for textured samples or aligned nanorods in many cases only a single reflecting plane (the basal plane) is parallel to the sample surface and only a single reflection peak is seen. In this work a Bruker AX8 D8 Advance Texture Diffractometer was used, a schematic showing the geometry of this system is shown in figure 2.10. The sample is rotated through θ and the detector is rotated simultaneously though *2θ*, this ensures the detector is at *θ* degrees with respect to the sample surface. A second mode of operation is used when an interference peak of interest is located. The detector is kept at *2θ* while the sample is rotated about the *θ* angle. This mode of operation is called rocking curve determination. The first mode of operation gives information on the distance between the atomic planes in the sample material while the rocking curve gives information on the structure of the material including the degree of alignment of crystallites/nanowires in the sample. The planar spacing found by the first mode of operation may be used to identify a material and its crystal structure by comparison to databases. The quality of crystalline materials may also be determined since impurity phases in the material may be detected in this way. Material information such as crystal orientation is very useful in the scope of this thesis, as c-axis aligned ZnO buffer layers are required for the growth of vertical nanowires. XRD is used in this work to determine the alignment of nanowires deposited as the data gathered is from a much larger area of the substrates than can be reasonably observed by a microscopy technique.

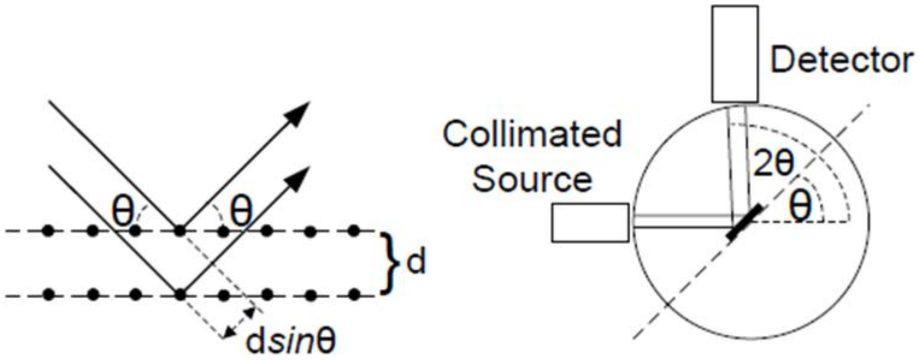

Figure 2.10: Schematic representation of Bragg diffraction conditions and right: schematic of geometry of XRD equipment used.

2.9.3 Spectroscopic ellipsometry

Ellipsometry is an optical technique which may be used to determine the optical properties of a material or, if the material properties are known, it may be used to determine the thickness of thin films. Ellipsometry operates by measuring the change of polarisation as a polarised beam of light is reflected from the interface between two materials of different refractive index.

Linearly polarised light with an axis of polarisation between the s and p planes is incident on the substrate. *S* and *p* polarization refers to the component of the electric field perpendicular and parallel to the plane of incidence respectively. This light is then reflected from the material interfaces inside the sample, the ZnO – Si interface for example, and from the air-sample interface. Since the axis of polarisation of the incident light lies off both the *s* and *p* planes, light reflected from the sample interfaces will have components from each plane leading to the reflection of elliptically polarised light. The intensity of the light reflected in the *s* and *p* planes is determined by the Fresnel equations.

$$\boldsymbol{R_s = \left|\frac{n_1 \cos\theta_i - n_2 \cos\theta_t}{n_1 \cos\theta_i + n_2 \cos\theta_t}\right|^2} \qquad \boldsymbol{R_p = \left|\frac{n_1 \cos\theta_t - n_2 \cos\theta_i}{n_1 \cos\theta_t + n_2 \cos\theta_i}\right|^2}$$

Where θ_i is the angle of incidence and θ_t is the angle light is transmitted through the interface in question into the next layer, R_S and R_P are the reflection coefficients of the *s* and *p* planes respectively and n_1 and n_2 are the refractive indices of the materials at each side of the interface.

A rotating polarisation analyser is used to gather the polarisation information of the light reflected from the substrate. The superposition of multiple light waves from each interface introduces interference that is dependent on the relative phase of each light wave. This information can then be compared to a model of the materials in question to determine layer thickness. During this work a J.A. Woollam M-2000UI ellipsometer was used as described in reference [21].

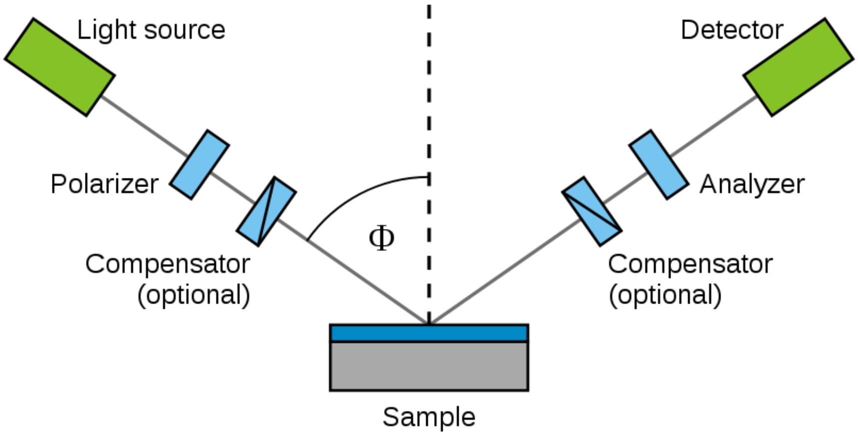

Figure 2.11: Schematic showing principle of operation of ellipsometry. (Image from Wikipedia.org article ‘Ellipsometry’ accessed 18th January 2012.

2.10 Field emission

The FE properties of samples produced in this work were the main topic of interest of the overall SFI-funded Research Frontiers Project which supported the work, and hence these properties were also examined in some depth. A requirement for FE is that characterisation must take place under high vacuum. Background gasses present may be ionised by the strong electric fields used in FE experiments resulting in arcing between the sample and anode (where the sample is the cathode), especially at sharp edges. Arcing is damaging to the samples and makes it difficult to obtain data. In order to minimise this issue, FE is not carried out until the chamber has reached a pressure of the order of 10^{-8} mbar. FE characterisation was carried out in a stainless steel CF vacuum chamber equipped with an Edwards EXT 555HE turbomolecular pump, backed by an Edwards RV12 rotary vane pump. The chamber pressure was monitored using an Edwards WRG-S-NW35 combitron gauge. The system is capable of reaching 10^{-7} mbar from atmosphere in approximately 12 hours and has an ultimate base pressure of ~ 2 x 10^{-8} mbar. Figure 2.12 shows a schematic of the chamber used with major components labelled.

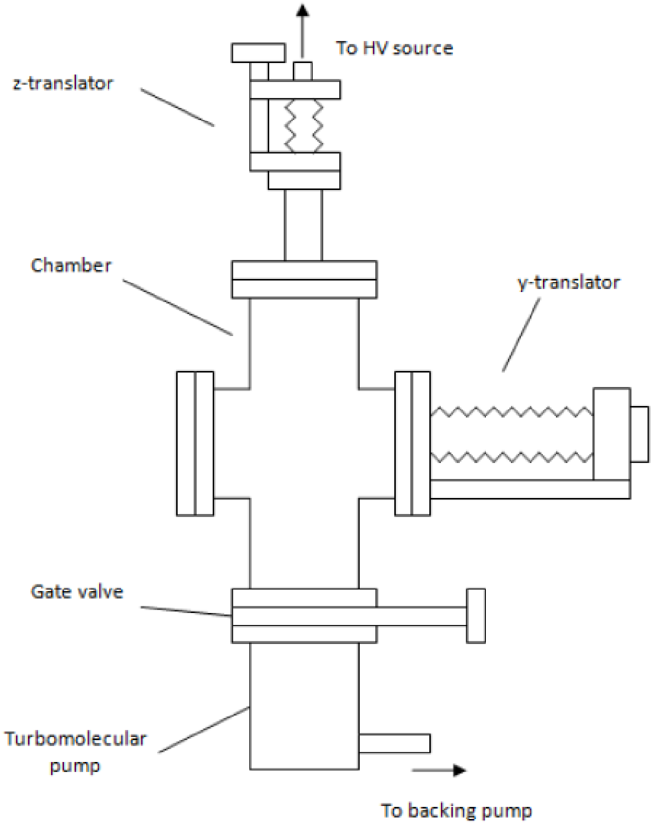

Figure 2.12: Schematic of field emission vacuum chamber.

A schematic of the internal setup is shown in figure 2.13. The sample holder consists of four stainless steel contacts, embedded in PTFE. One of the four contacts is left exposed and samples to be examined are placed onto the other three. Samples are affixed onto the contacts using silver paste to ensure both that the samples do not move during characterisations due to system vibrations and that there is good electrical contact between the sample and the stainless steel. The sample holder can be moved horizontally using the *y*-translator, as shown in figure 2.11. This allows up to three samples to be loaded into the system and characterised without breaking vacuum between samples. The anode used is a flat, polished, circular, stainless steel electrode of radius 8 mm. This is mounted onto a rod attached to a linear translator at the top of the chamber. The anode is set into a PTFE block situated at the end of the rod. This prevents any electrical interactions with the sides of the anode; for reliable FE data only interaction with the planar face of the anode is desired.

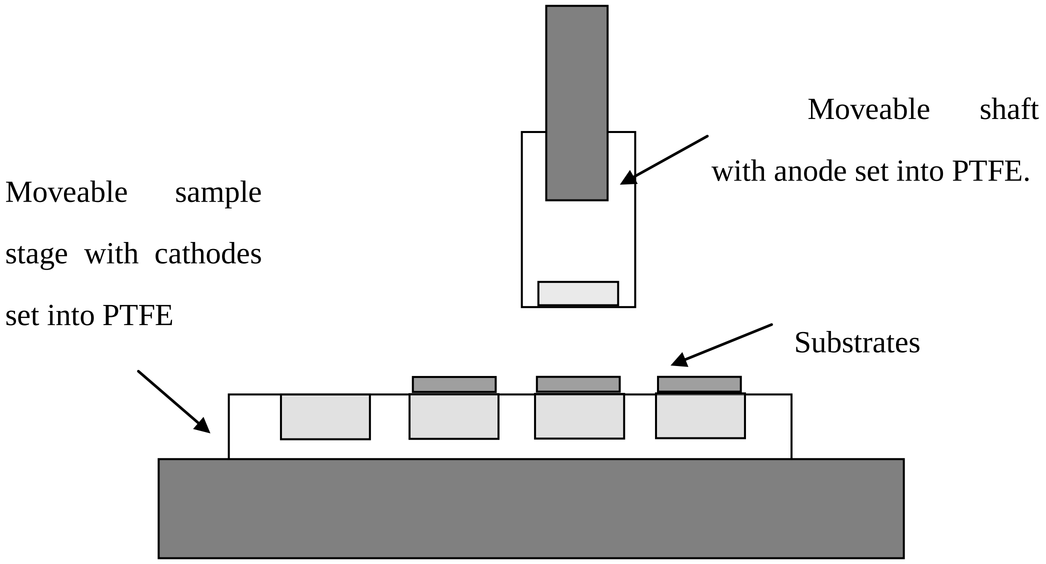

Figure 2.13: Field emission chamber interior

The linear translator has a digital scale with a resolution of 10 µm which allows the distance between the anode and sample to be controlled reliably. Before the anode is moved into place above each sample, the sample holder is moved so that the empty sample contact is below the anode. The anode is then lowered until electrical contact is made and the digital scale on the linear translator is zeroed. This must be repeated for every set of samples examined, as the linear translator is removed when the samples are being placed on the holder. The thickness of each sample is known, as is given by the specification of the wafers plus the additional thickness of subsequent layers deposited. However since electrical contact is made through the use of silver paste, the height of the sample over the metal contact cannot be assumed to be constant. Due to this, the height of each sample above the contacts is measured using a micrometer. Typically the sample – anode separation used is 250 µm. Figure 2.14 shows photographs of the system used.

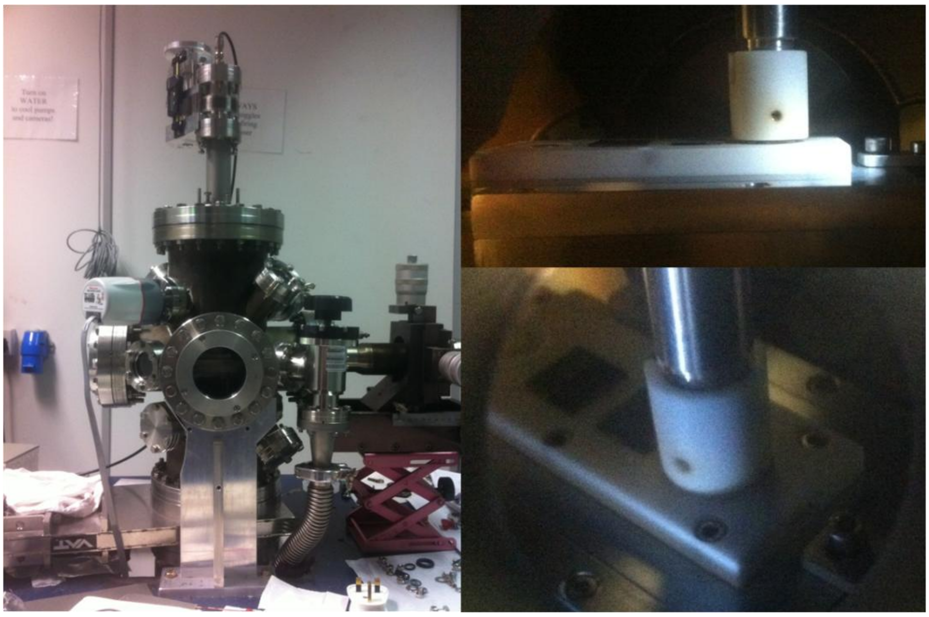

Figure 2.14: Photographs of FE chamber (left) and of the sample holder and movable electrode (right).

Figure 2.15 shows a circuit diagram of the apparatus used. The picoammeter used is a Keithley model 6485 with 10 fA resolution. The diodes and resistor in the circuit are to protect the picoammeter from high currents, which can occur during arcing. The resistor limits the current while the two diodes are fast acting low leakage diodes that serve to bypass the picoammeter in the case of a current surge. However the resistor between the sample and earth means that the sample is not electrically grounded but is floating at some low voltage. This may be calculated by measuring the voltage drop over the resistors and using Ohm's law; the potential over the sample may be determined in this way. The electrode is positively biased using a Stanford PS350 high voltage source capable of supplying up to 5 kV and 5 mA.

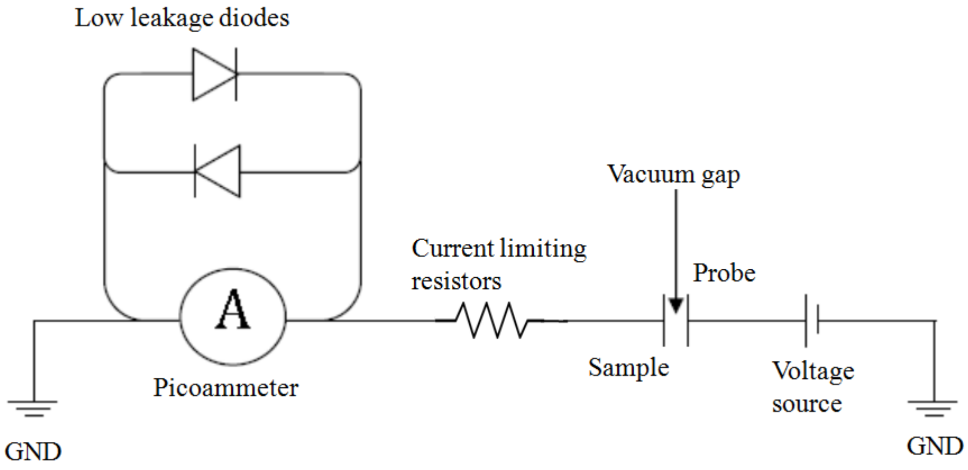

Figure 2.15: Circuit diagram of FE apparatus.

The voltage source and picoammeter are controlled using a Labview program through a GPIB interface. The voltage was ramped up and down at a rate of 1 V/s. The potential difference over the sample and the current measured by the picoammeter are stored by the computer.

The *I*-*V* data gathered in this way is initially very noisy with some hysteresis generally observed. This is due to factors such as adsorbates on the surface of the sample, Joule heating of the sample and abnormal features such as individual nanowires (perhaps protruding more than others) that are melted or field ionised [22]. In order to eliminate the noise and hysteresis the sample is "conditioned", i.e. the voltage over the samples is ramped up and down repeatedly until a smooth repeatable curve with no pronounced hysteresis is obtained.

2.10.1 Field emission imaging

The *I*-*V* data produced by field emission may be used to determine some properties of the sample but may not give information on the uniformity of emission across the sample. In order to gain information on this, the metal anode is replaced with a phosphor electrode. This electrode consists of glass coated with ITO, which is then coated with phosphor (P22G, TMS Vacuum Components). Due to the modular design of the chamber, it is possible to remove and replace the anode without disturbing the rest of the apparatus.

A prism positioned above the phosphor electrode directs the light (generated by FE electron impact on the phosphor screen) out of the chamber through a window, as illustrated in figure 2.16. The directed light is imaged using an Artray Artcam

150p2 camera. The operation of the FE circuit remains the same as in the case with the metal electrode, the phosphor is connected to the Stanford voltage source and IV data may be gathered during imaging. However due to the fragile nature of the phosphor electrodes, the samples are conditioned beforehand to reduce the instance of arcing as this may damage the phosphor.

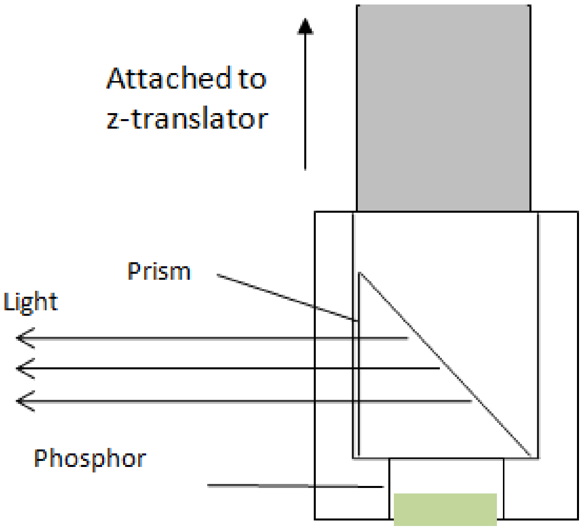

Figure 2.16: Schematic of phosphor electrode showing phosphor along with prism used to direct the light produced to a detector. This is mounted in a PTFE block which is itself mounted on a rod attached to the linear translator.

Field emission characterisation carried out in the work was done in collaboration with a colleague, Mr. Éanna McCarthy. The picoammeter, current source, safety circuit, and data acquisition system used were put in place prior to this work while chamber interior, including sample holder, phosphor electrodes, and z-translator were added during the course of this work.

2.11 References

1. Tien, L.C., et al., *Synthesis and microstructure of vertically aligned ZnO nanowires grown by high-pressure-assisted pulsed-laser deposition.* Journal of Materials Science, 2008. **43**(21): p. 6925-6932.

2. Zhang, Y., R.E. Russo, and S.S. Mao, *Femtosecond laser assisted growth of ZnO nanowires.* Applied Physics Letters, 2005. **87**(13): p. 133115-133115-3.

3. Biswas, M., E. McGlynn, and M.O. Henry, *Carbothermal reduction growth of ZnO nanostructures on sapphire—comparisons between graphite and activated charcoal powders.* Wide Band Gap Semiconductor Nanostructures for Optoelectronic Applications, 2009. **40**(2): p. 259-261.

4. Grabowska, J., et al., *Studying the growth conditions, the alignment and structure of ZnO nanorods.* PSE 2004 Plasma Surface Engineering (PSE 2004), 2005. **200**(1–4): p. 1093-1096.

5. Grabowska, J., et al., *Synthesis and photoluminescence of ZnO nanowires/nanorods.* Journal of Materials Science-Materials in Electronics, 2005. **16**(7): p. 397-401.

6. Greene, L.E., et al., *General route to vertical ZnO nanowire arrays using textured ZnO seeds.* Nano Letters, 2005. **5**(7): p. 1231-1236.

7. Law, M., et al., *Nanowire dye-sensitized solar cells.* Nat Mater, 2005. **4**(6): p. 455-459.

8. Byrne, D., et al., *Study of Morphological and Related Properties of Aligned Zinc Oxide Nanorods Grown by Vapor Phase Transport on Chemical Bath Deposited Buffer Layers.* Crystal Growth & Design, 2011. **11**(12): p. 5378-5386.

9. Saunders, R.B., E. McGlynn, and M.O. Henry, *Theoretical Analysis of Nucleation and Growth of ZnO Nanostructures in Vapor Phase Transport Growth.* Crystal Growth & Design, 2011. **11**(10): p. 4581-4587.

10. WangWang, C.J. Summers, and Z.L. Wang, *Large-Scale Hexagonal-Patterned Growth of Aligned ZnO Nanorods for Nano-optoelectronics and Nanosensor Arrays.* Nano Letters, 2004. **4**(3): p. 423-426.

11. Liu, D.F., et al., *Periodic ZnO Nanorod Arrays Defined by Polystyrene Microsphere Self-Assembled Monolayers.* Nano Letters, 2006. **6**(10): p. 2375-2378.

12. Yu, C.-W., et al., *Patterned Fabrication of Single ZnO Nanorods and Measurement of Their Optoelectrical Characteristics.* Journal of Nanoscience and Nanotechnology, 2008. **8**(9): p. 4377-4381.

13. Ng, V., et al., *Nanostructure array fabrication with temperature-controlled self-assembly techniques.* Nanotechnology, 2002. **13**(5): p. 554-558.

14. Rybczynski, J., et al., *Formation of super arrays of periodic nanoparticles and aligned ZnO nanorods - Simulation and experiments.* Nano Letters, 2004. **4**(10): p. 2037-2040.

15. Li, C., et al., *Wet Chemical Approaches to Patterned Arrays of Well-Aligned ZnO Nanopillars Assisted by Monolayer Colloidal Crystals.* Chemistry of Materials, 2009. **21**(5): p. 891-897.

16. Wang, L.K., Q.F. Yan, and X.S. Zhao, *From planar defect in opal to planar defect in inverse opal.* Langmuir, 2006. **22**(8): p. 3481-3484.

17. Brinker, C.J. and G.W. Scherer, *Sol-gel science: the physics and chemistry of sol-gel processing.* 1990, San Diego: Academic Press Limited.

18. Nozawa, K., et al., *Smart Control of Monodisperse Stöber Silica Particles: Effect of Reactant Addition Rate on Growth Process.* Langmuir, 2005. **21**(4): p. 1516-1523.

19. Stober, W., A. Fink, and E. Bohn, *Controlled Growth of Monodisperse Silica Spheres in Micron Size Range.* Journal of colloid and interface science, 1968. **26**(1): p. 62-&.

20. Cullity, B.D. and S.R. Stock, *Elements of X-Ray Diffraction (3rd Edition).* 2001: Prentice Hall.

21. McCarthy, E., et al., *Effects of the crystallite mosaic spread on integrated peak intensities in 2θ–ω measurements of highly crystallographically textured ZnO thin films.* Journal of Physics D: Applied Physics, 2011. **44**(37): p. 375401.

22. Gomer, R., *Field Emission and Field Ionisation.* 1993: American Vacuum Society Classics.

Chapter 3: Deposition techniques

3.1 Introduction

This chapter describes the results of using the growth techniques described previously in chapter 2. The three deposition techniques, PLD, CBD, and CTR-VPT are discussed in detail as is the reasoning used to determine which of these techniques would be used in creating spatially ordered nanowire arrays for characterisation by field emission. The results of these techniques are presented in two main sections, firstly, a discussion on the results of depositing ZnO buffer layers using the PLD and CBD techniques, and secondly, a discussion on nanowire arrays grown using both CBD and CTR-VPT techniques.

3.2 ZnO Buffer layer deposition

The use of a ZnO buffer layer is required in order to both initiate growth and to ensure c-axis aligned nanowire growth because, in both the CBD and CTR-VPT techniques, ZnO will not readily nucleate on bare Si/SiO_2 substrates. In this work ZnO buffer layers have been deposited using two techniques, PLD and CBD, in order to facilitate the subsequent deposition of vertically aligned ZnO nanowires. In both cases, Si/SiO_2 substrates were coated with highly uniform and well textured ZnO layers as described in this section.

3.2.1 Pulsed laser deposition (PLD)

PLD was carried out on bare Si/SiO_2 as described in section 2.5. The parameters outlined in that section are those used in previous work by our group [1, 2] to prepare ZnO buffer layers for subsequent vertically aligned CTR-VPT deposition and were not altered during the course of this work.

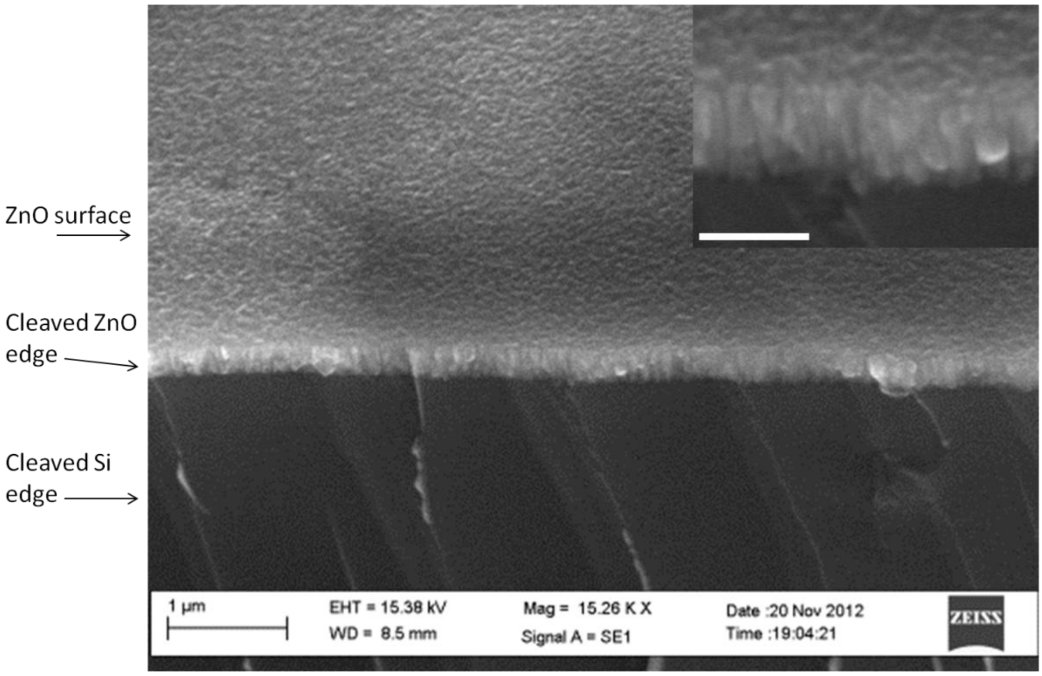

Figure 3.1: SEM image of cleaved edge on PLD deposited ZnO thin film. A higher magnification of the ZnO cleaved edge is shown in inset with scale bar showing 500nm.

ZnO layers deposited were found to be columnar in structure with very high column density such that adjacent columns are in contact and form an effectively continuous film of ZnO. Figure 3.1 shows an SEM image of a cleaved PLD ZnO sample showing the columnar structure. Unlike CBD depositions, PLD does not need a pre-existing ZnO seed layer to either initiate nucleation or to ensure crystal alignment. High temperature depositions allow for the migration of atoms to energetically favourable positions, enhancing the crystallinity and c-axis orientation of the film [3]. Ellipsometry was carried out on ZnO layers deposited by PLD, under the conditions used, the thickness of the layer was found to be in the range ~ 175 nm – 325 nm, with the thickest areas of the layer found in the centre of the sample, directly adjacent to the ZnO target. Larger samples, which extend further from the centre of the sample holder, were found to have thicknesses at the lower end of the range above towards their edges. Ellipsometry measurements were carried out as described in McCarthy *et al.*[4] where good agreement between ellipsometry and TEM thickness measurements are reported.

3.2.2 Chemical bath deposition (CBD)

In order to deposit a ZnO buffer layer onto Si/SiO_2 using any of the CBD techniques investigated, a ZnO seed layer must first be present on the substrate. This seed layer provides an energetically favourable site for the heterogeneous nucleation and crystal growth [5]. Without such a seed layer, many substrates, including Si/SiO_2 will not initiate nucleation. There are many techniques available to deposit such seed layers including sol-gel, magnetron sputtering, and pulsed laser deposition [6-8]. In the interests of using a technique that is both simple to implement and scalable the method devised by Greene and Law was used [5]. This technique, as outlined in chapter 2, involves the drop-coating of a zinc acetate solution onto the substrate.

A number of factors influence the deposition of the seed layer onto a substrate. These include the volume of solution applied and atmospheric humidity [9]. Lee *et al.* have demonstrated a link between humidity and the deposition of the seed layer, proposing that it is not zinc acetate that coats the substrate but rather zinc hydroxide.

The chemical origins of the seed layer have been reported by Byrne *et al.*[10], revealing the nature of the process dependence on atmospheric humidity. The reaction is driven by an excess of water which has diffused from the atmosphere. This excess alters the equilibrium toward the hydrolysis of zinc acetate, leading to the formation of insoluble zinc hydroxide. This hydroxide precipitate takes time to travel through the bulk of the solution before reaching the substrate since in the solution the concentration of water will be highest at the interface between the air and solution. If 3.5 µl of solution is applied per cm^2 of substrate area, leaving the solution on the substrate for approximately 20 seconds prior to rinsing led to substrates that would subsequently produce high quality buffer layers and nanowire depositions. Due to a number of factors such as changes in film volume due to ethanol evaporation [11], and changes in zinc acetate concentration [12], there is a convective fluid flow which may carry suspended particles to the edge of the sample [13] resulting in the edges being coated with a thicker layer than the substrate centre. However this was not observed to significantly alter the nature of subsequent ZnO deposition in either region. After drop coating the substrates are annealed at 350°C for 30 minutes to decompose the zinc hydroxide into zinc oxide. Figure 3.2 shows the chemical route to the formation of ZnO seeds proposed by Byrne *et al.*[14]. The drop-coating technique has been used successfully on substrates ranging in size from 2 cm^2 up to full silicon wafers (~45 cm^2).

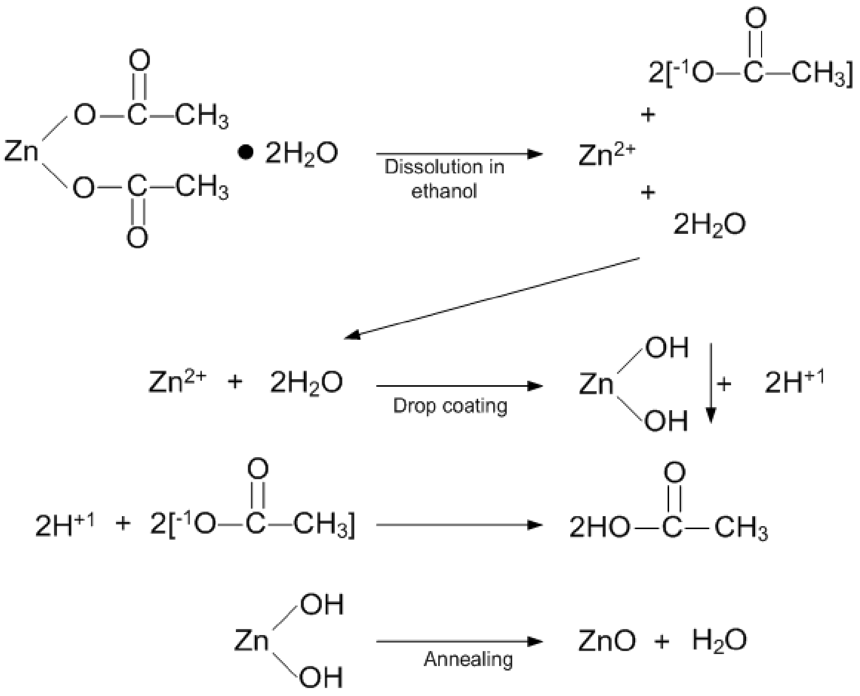

Figure 3.2: Chemical route to the formation of ZnO seed layers proposed by Byrne *et al*.[14].

Work carried out previously by a colleague in our laboratory, Dr. Daragh Byrne, has shown that while CTR-VPT depositions may be carried out on this seed layer without any subsequent step, the results are indicative of poor substrate coverage and poor alignment. For this reason, even though potential nucleation points are provided, a second stage ZnO buffer layer must be deposited to achieve more consistent results with a final VPT nanowire growth step.

In this work, three CBD techniques were investigated as described in section 2.4. In all cases these depositions were carried out on substrates coated with a ZnO seed layer as described above. In comparison to ZnO buffer layers deposited using PLD, as described above, low temperature aqueous solutions have the advantage of not requiring specialist equipment and the technique is easily scalable so that full Si/SiO_2 wafers may be uniformly coated using a CBD technique, a sample size significantly larger than may be coated using the PLD technique described in chapter 2.

All three techniques resulted in highly uniform ZnO deposition across the substrate with layers composed of densely packed ZnO columns being observed, the thickness of the layers being determined by the length of time the deposition is carried out with the thickness generally in the range of 300 – 500 nm for the durations as noted in section 2.4. In general buffer layers produced using the NaOH based reaction had a much lower incidence of precipitates on the substrate surface while those produced using the both the Zn acetate and HMT based reactions required constant agitation of the substrate during deposition to remove precipitates that settle on the surface. The quantity of precipitate present on the substrate post-deposition is related to the density of the underlying seed layer. It has been observed in cases where ZnO seed density is low there is a higher incidence of precipitates on the substrate. This may be due to precipitates becoming trapped in the space between ZnO columns, since denser areas tend to grow a buffer layer with greater uniformity, with no empty space in the film.

ZnO buffer layers grown by CBD tend to be very well aligned; in general this is due to the highly textured nature of the underlying ZnO seed layer. As shown by Greene *et al.* the ZnO seeds as derived from Zn acetate are flat platelets with their c-axis perpendicular to the large face and that the platelets generally lie flat with respect to the substrate surface [5]. Since the c-axis is the preferred axis of growth, in general ZnO crystals are vertically aligned due to the orientation of the seed on the substrate. However, since the seeds precipitate randomly onto the substrate, some will inevitably not be vertically aligned due to multiple seed settling on top of or immediately adjacent to each other. A slight tilt in some of the ZnO columns produced in subsequent CBD growths may be observed, the incidence of which however, appears to be inversely related to the density of the film. It appears that in the case of high density layers, adjacent columns confine each other laterally, allowing only for vertical growth. This tilt can be seen in figure 3.3, which shows an example of a Zn acetate derived buffer layer with low column density, while inset is an image from above showing the same sample.

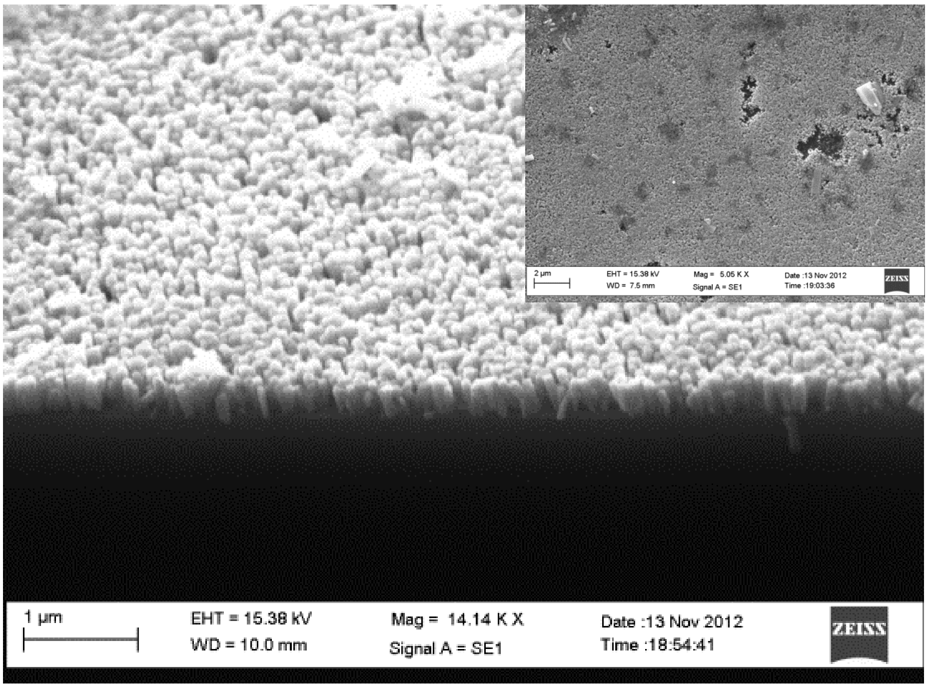

Figure 3.3: SEM image of low density Zn acetate derived ZnO buffer layer, clearly visible at the edge of the layer is a tilt in some of the ZnO columns, suggesting that c-

axis alignment is also brought about by spatial confinement. Inset is a plan-view image of the same sample showing gaps in the CBD layer.

While all three methods produced highly uniform and well aligned ZnO layers, the decision was made to use buffer layers deposited primarily by the direct decomposition of Zn acetate by forced hydrolysis [15, 16] for subsequent nanowire deposition. The reason for this is surface roughness; as is explained later in chapter 4, inverse nanosphere lithography requires a flat surface to ensure uniform results. Figure 3.4 shows a comparison of a buffer layer deposited using Zn acetate based CBD and HMT based CBD. Zn acetate based depositions tend to exhibit flat topped columnar growth, while both HMT and NaOH techniques tend to produce tapered structures.

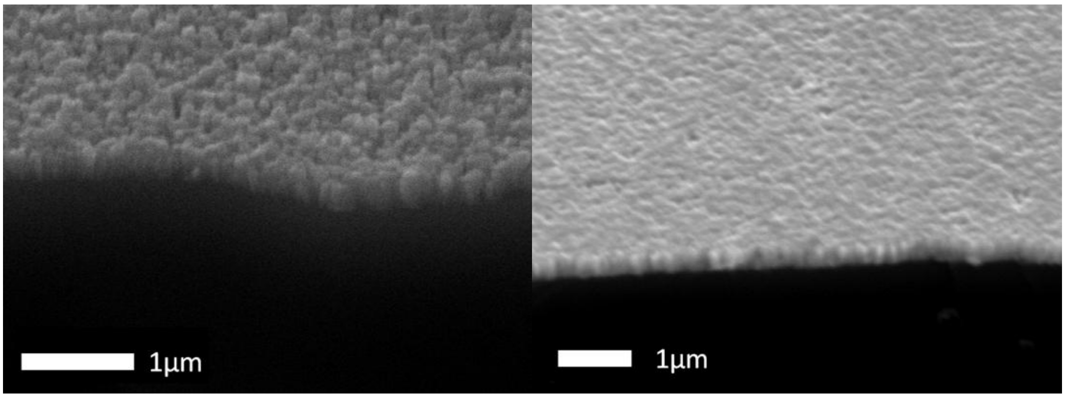

Figure 3.4: SEM images of ZnO buffer layers deposited by HMT based CBD (left) and by Zn acetate based CBD (right). It is clear that the Zn acetate method results in layers with a flatter surface morphology.

During Zn acetate based buffer layer deposition, it is necessary to regularly agitate the substrate during growth. In this solution both bubbles and precipitates form and adhere to the substrate, if these are not removed they will cause defects in the layer deposited. In the case of any precipitate remaining on the substrate, this can act as a point for further nucleation of precipitates; while an air bubble on the substrate surface will prevent any deposition from occurring in that area for the time it is present, possibly leading to large variations in layer thickness.

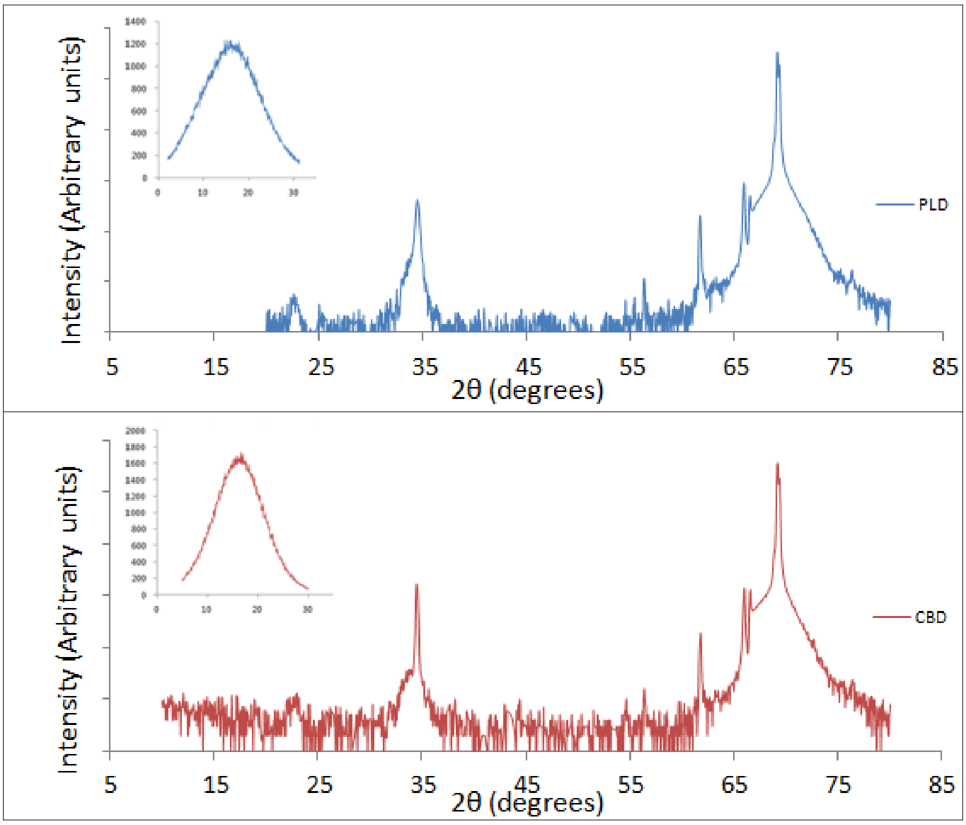

Figure 3.5: XRD θ-2θ scan of PLD ZnO buffer layer (blue) and Zn acetate buffer layer (red), y-axes are in log scale. The inset shows the rocking curve data from both taken using the 34.4° ZnO (002) plane.

Compared to ZnO buffer layers produced using the PLD technique, Zn acetate derived buffer layers compare quite favourably. Both provide quite flat surfaces for subsequent growth, uniform substrate coverage and c-axis orientation. Figure 3.5 shows XRD data from ZnO buffer layers produced by Zn acetate derived CBD and by PLD. The inset in this graph is the XRD rocking curve taken using the 34.4° peak corresponding to the ZnO (002) plane, showing that both layers are quite well textured with respect to the substrate normal with the CBD layer having a rocking curve full width at half maximum (FWHM) of 10.4° compared to the PLD layer's value of 15.2°.

3.3 ZnO Nanowire growth

The vast majority of the work described in this thesis was carried out on ZnO buffer layers deposited on Si/SiO_2 substrates by CBD. However while some work was carried out on buffer layers deposited by PLD, growths carried out under the same conditions using either buffer layer type showed no noticeable morphological differences.

As described in chapter 2, two techniques were used during the course of this work in order to achieve the deposition of ZnO nanowires. These are CBD and CTR-VPT. CBD nanowire growth is carried out under similar conditions to CBD buffer layer deposition while CTR-VPT is a technique only suitable for the deposition of nanostructures.

3.3.1 CBD nanowire growth

The goal of this thesis is to develop a method for the growth of spatially ordered ZnO nanowire arrays for field emission characterisation. For this reason, any deposition technique used must be compatible with the methods used to control the ordering of ZnO nanowire arrays. In order to achieve spatially ordered nanowire arrays using CBD, an inverse nanosphere lithography technique must be used. This is discussed in greater detail in chapter 4 and this section is concerned with some of the details pertaining to the growth method itself, leaving the description of the patterning technique to the next chapter.

CBD nanowire depositions were carried out predominantly using the Zn acetate CBD method in order to ensure compatibility with the inverse nanosphere lithography technique described later in this thesis. It was found that HMT and NaOH derived CBD solutions etched the silica mask and were unsuitable for ordered nanowire array growth.

Zn acetate based nanowire growth was carried out using the same concentrations as used for ZnO buffer layers. The nature of CBD depositions is such that ZnO will nucleate at all points where it is energetically favourable to do so. In the case of a ZnO buffer layer, it will be favourable for nucleation to occur at all points on the substrate, so in order to achieve the growth of individual nanowires as opposed to continuous film growth, the sample must be masked, as described later in chapter 4, to leave only selected areas, where deposition is desired, exposed to the Zn acetate solution.

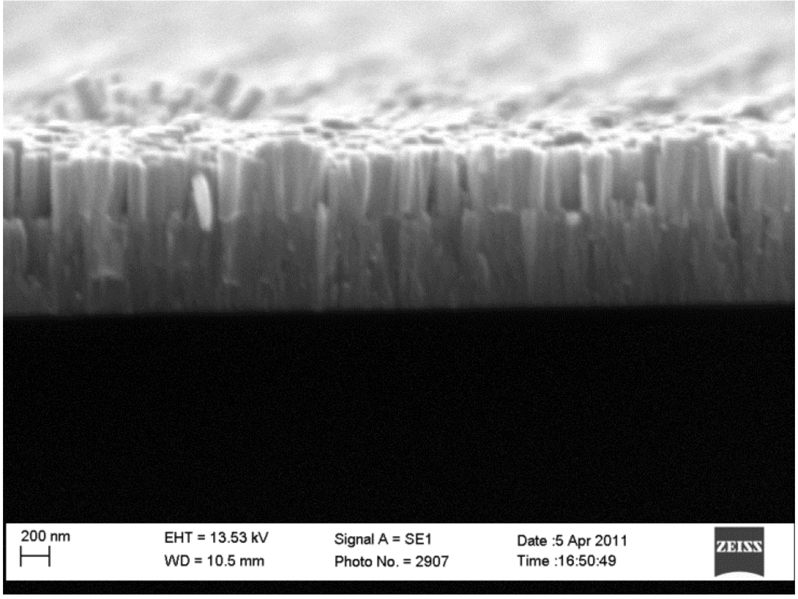

Figure 3.6: Cross section SEM image of Zn acetate nanowire array with deposition time of 90 mins.

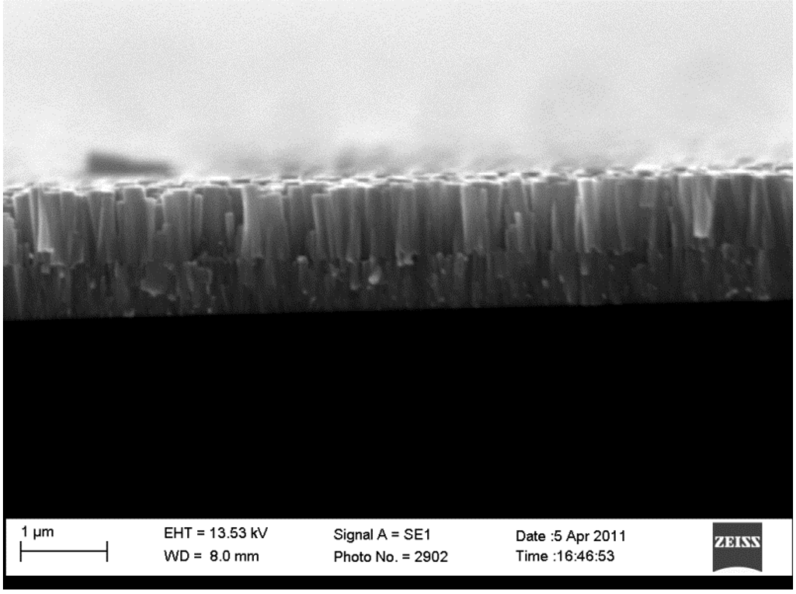

Figure 3.7: Cross section SEM image of Zn acetate nanowire array with deposition time of 180 mins.

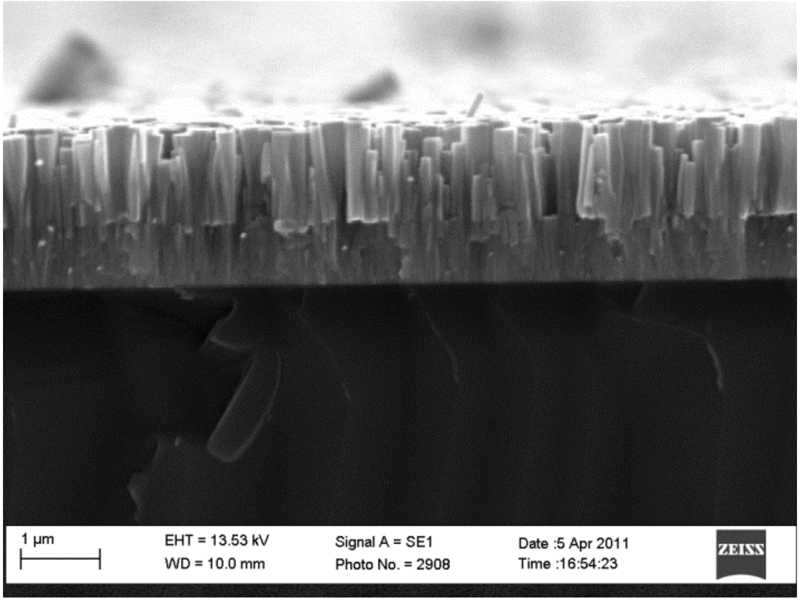

Figure 3.8: Cross section SEM image of Zn acetate nanowire array with deposition time of 270 mins.

Figures 3.6 – 3.8 show cross-section SEM images of CBD nanowire arrays with deposition times of 90, 180, and 270 minutes respectively. The height of the nanowires over the underlying buffer layers appears to approximately proportional to the deposition time as is shown in figure 3.9. Due to the accumulation of precipitates in the CBD solution, the acetate solution is replaced every 90 mins during deposition. Samples grown by CBD tend to have very uniform height over the entire substrate area. This makes them an attractive option for field emission purposes as their height is highly uniform and very controllable, since there is a direct relationship with the deposition time, and there is little variation over large areas. There are, however, a number of drawbacks immediately apparent, firstly as shown in figure 3.10 below; any area not suitably masked from the CBD solution will exhibit film growth, with the same height as the nanowires produced. Secondly, Zn acetate derived nanowires tend to widen laterally as they grow, placing a limit on the possible height of nanowires grown this way as they will eventually coalesce to form a film. An example of a spatially ordered nanowire array where a number of nanowires are wider at their tips than at their bases is shown in Figure 3.11. The origin of this is in the capping nature of Zn acetate depositions. During deposition the acetate counter ion is preferentially absorbed on the Zn^{2+} (001) face, screening it from growth and forcing deposition to occur on other faces [17]. This capping action is also responsible for the flat morphology of buffer layers grown using Zn acetate, contributing to the decision to utilise it for the majority of samples grown.

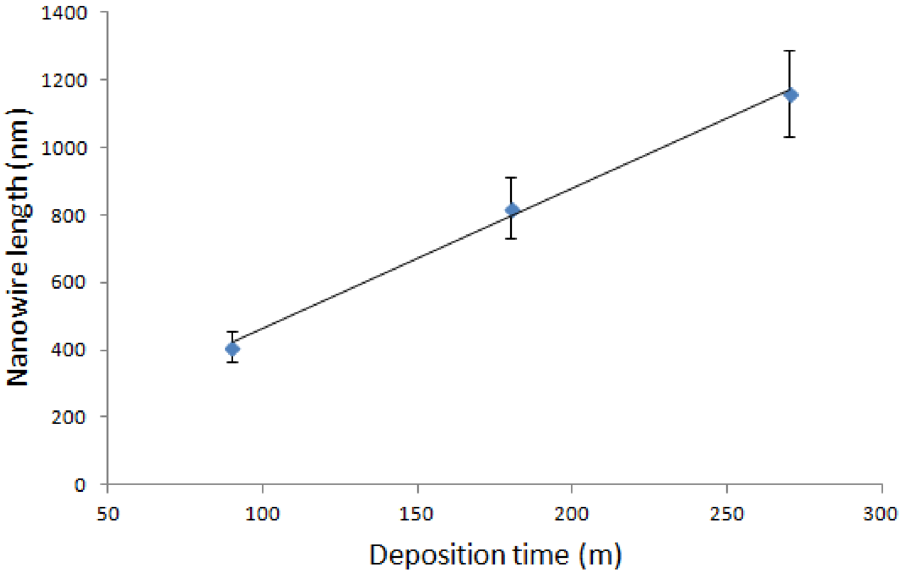

Figure 3.9: CBD nanowire length vs. Time. Zn acetate derived CBD depositions appear to deposit material along the *c*-axis at a constant rate. Standard deviation in CBD nanowire height is shown as error bars. Measurements taken from cross-sectional SEM images.

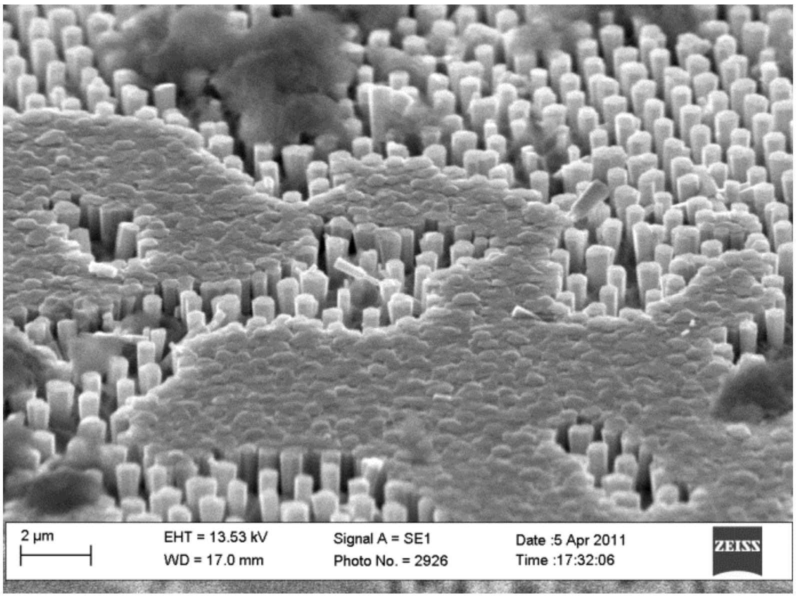

Figure 3.10: CBD nanowire array exhibiting film growth in areas not effectively masked from the CBD solution.

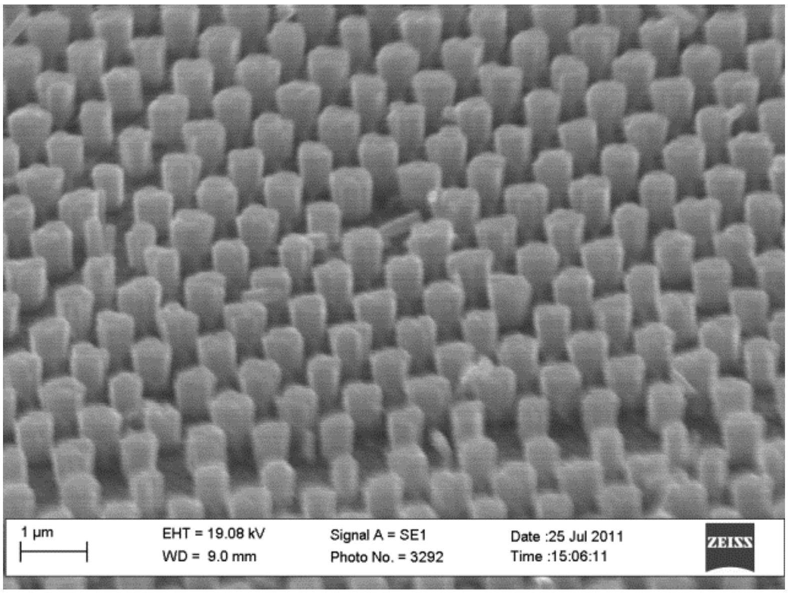

Figure 3.11: Zn acetate CBD nanowire array with nanowires exhibiting some widening towards their tips.

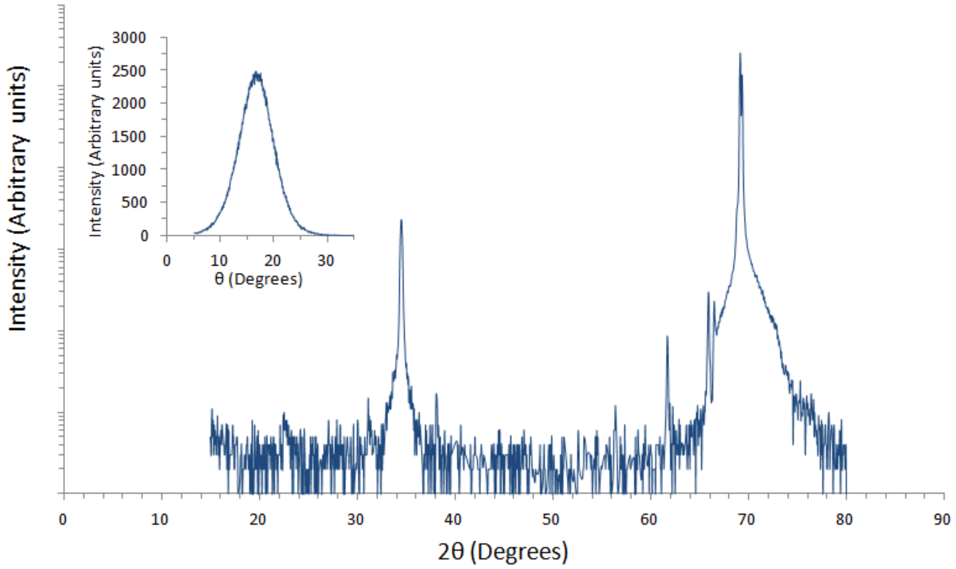

Figure 3.12: XRD *θ-2θ* scan of ZnO nanowire arrays grown by Zn acetate CBD with log y-axis. This particular array was templated using the inverse nanosphere lithography technique described in the chapter 4. This data is taken from sample with 1.5 µm spacing. The inset shows the rocking curve data taken using the 34.4° ZnO (002) plane.

Figure 3.12 shows XRD data for a nanowire array deposited using Zn acetate CBD. The inset shows rocking curve data taken using the 34.4° ZnO (002) plane showing a FWHM of ~7.5°. This shows that this technique yields highly uniform results not only in terms of nanowire length and morphology but also crystal quality and alignment.

Very uniform and repeatable results are achievable using CBD techniques; however for the purposes of field emission it is believed that sharp tipped nanowires, with high aspect ratios are the most efficient emitters [18-21]. The nanowires presented here are relatively short and have low aspect ratios. It is known however, that nanowires grown using the NaOH CBD technique, based on the work of Peterson *et al.* [22], produce narrow needle like nanowires [23]. The possibility of using this technique subsequent to acetate nanowire growth was investigated with the aim of growing nanowires as seen in figure 3.10 and then using the NaOH technique to continue the growth of these structures to eventually result in sharp tipped nanowires. The reason that initially the acetate method is required is that the silica mask described later in chapter 4 is etched by the basic NaOH solution. Figure 3.13 shows the results of these growths, it is clear that no significant tapering of the acetate grown structures has occurred, but the spaces between such structures have become filled with narrow needle like NaOH derived nanowires. Their presence at these locations is due to the etching of the silica mask and subsequent growth on the freshly exposed buffer layer. Figure 3.14 shows this sample from above, it can be clearly seen that in many areas the spaces between the acetate nanowires are being filled with needle like nanowires, which is due to the basic solution etching the mask, because if there were exposed ZnO regions during the initial acetate deposition those areas would have nanowires of the same height as other structures due to the highly uniform nature of CBD deposition.

Thus all CBD nanowires discussed later in this thesis are grown using Zn acetate solutions only with no combinations with other CBD methods used due to incompatibility with the nanosphere lithography mask.

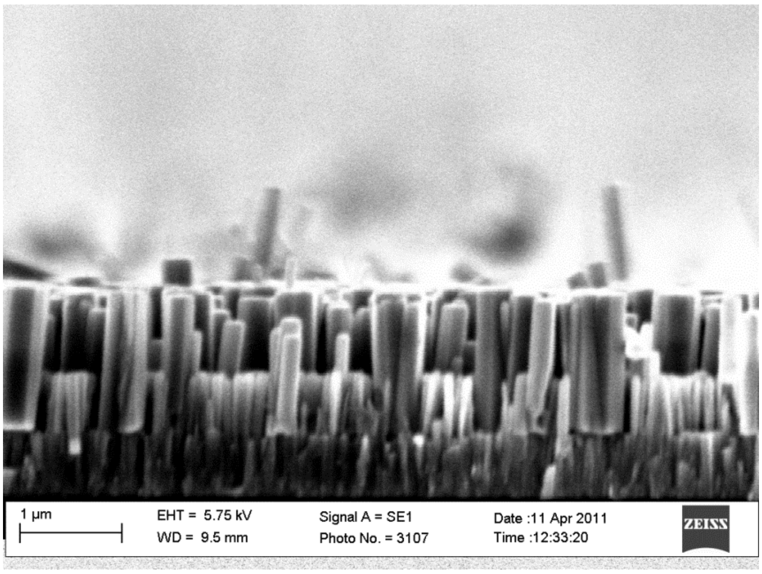

Figure 3.13: Cross section of array produced using a hybrid Zn acetate/NaOH CBD technique. Zn acetate nanowires are visible with needle like NaOH derived nanowires in between.

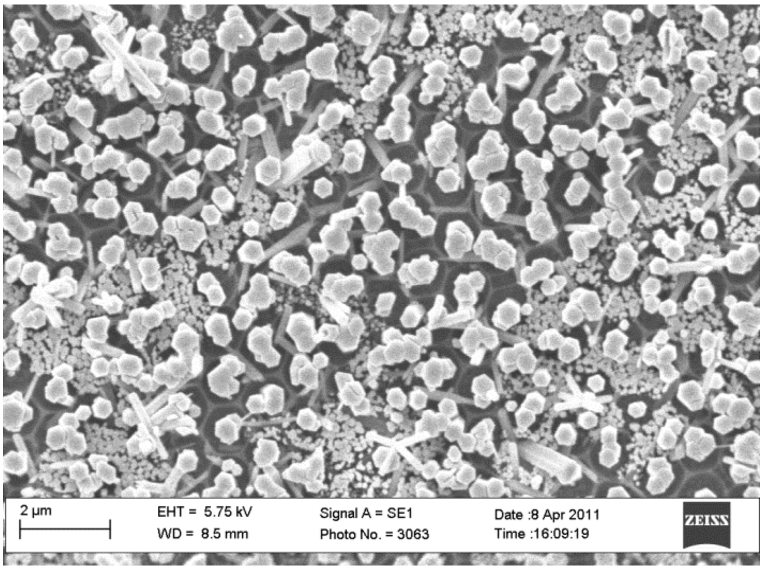

Figure 3.14: Results of hybrid Zn acetate/NaOH CBD deposition, the patterned acetate nanowires are visible with NaOH derived growth in between. NaOH nanowires grow in areas previously covered by the silica mask.

3.3.2 CTR-VPT nanowire growth

This section will discuss the use of CTR-VPT to grow ZnO nanowires, predominantly on Si/SiO_2 substrates which have been coated with a ZnO buffer layer either by PLD or CBD or have been coated with an Au catalyst layer. Carbothermal reduction is based on the ability of carbon to act as a reducing agent. At high growth temperatures metal oxide powders in contact with carbon are reduced to metal vapour and either carbon monoxide or carbon dioxide as shown in equations 3.1 and 3.2, which dominate in different temperature regimes; [24-27]

$$MO + C \rightarrow M + CO \qquad (3.1)$$

$$MO + ½C \rightarrow M + ½CO_2 \qquad (3.2)$$

The metallic vapour is quickly reoxidised by residual oxygen following condensation on regions of a substrate where it is energetically favourable for nucleation to occur to form a metal oxide deposit. ZnO grown on non-epitaxially matched substrates in this manner tend to not be aligned [25]. It is possible to achieve vertically aligned nanowire growth by either using an epitaxially matched substrate coated with a metallic catalyst such as Au or to use substrates coated with ZnO buffer layers [5, 28, 29]. In the case of ZnO, the CTR equations given above take the following form, where the reaction shown in equation 3.4 is dominant in the temperature range where ZnO deposition occurs;

$$T < 973K \qquad ZnO(s) + \tfrac{1}{2} C(s) \rightarrow Zn(g) + \tfrac{1}{2} CO_2(g) \tag{3.3}$$

$$T > 973K \qquad ZnO(s) + C(s) \rightarrow Zn(g) + CO(g) \tag{3.4}$$

Significant sublimation of ZnO only occurs at temperatures greater than 2250 K, and thus the CTR reaction allows Zn vapour to be produced at the much lower temperatures of ~1200 K, which is much easier to achieve. It is also possible to produce Zn vapour at even lower temperatures of 700 – 800 K by the direct evaporation of Zn metal, however such experiments carried out by a colleague resulted in very unpredictable deposition and this route was not investigated further in the course of this thesis.

There are two mains routes by which CTR-VPT ZnO nanowires may grow on a substrate. These are the vapour-liquid-solid (VLS) and vapour-solid (VS) growth mechanisms. VLS growth requires that there is a metallic catalyst for deposition to occur. At the high temperatures required for CTR-VPT growth to occur, vapour generated in the CTR reaction is incident on the substrate surface and condenses at metal catalyst coated regions preferentially, since the metal provides energetically favourable sites for nucleation. The Zn/metal alloy (the metal is Au in all cases described in this thesis) becomes supersaturated with dissolved Zn and the Zn precipitates out of the Au and may then react with oxygen in the furnace to form ZnO. The Au is not consumed in this process and is available for further Zn nucleation to occur. In this way ZnO nanowires may be grown, with the Au tip staying on top of the grown wire [30]. This process continues as long as there is Zn vapour present in the furnace and the temperature is high enough that the catalyst material remains in its liquid state. Nanowires grown by the VLS method often have Au tips. Controlled VLS growth may be achieved with the use of patterned catalyst layers, as discussed in chapter 4.

The VS mechanism is a catalyst free growth method that involves the production of Zn vapour through the CTR reaction and nucleation directly onto a substrate at an energetically favourable point. In this thesis substrates coated with ZnO buffer layers provide the energetically favourable nucleation points. Both VLS and VS growth modes may be observed on the same sample (i.e. a ZnO buffer layer with Au coating in certain regions) under the growth conditions used in this work and in such circumstances nanowires are observed both with and without Au tips.

Figure 3.15 shows an example of CTR-VPT nanowire growth on a Si/SiO_2 substrate which has been catalysed using Au. There is a clear line in this image beyond which no growth has taken place; this is the boundary between the Au coated area and an uncoated area with no Au deposited thereon. This shows us clearly that in the absence of a source of suitable nucleation sites, such as those provided by a metallic catalyst or ZnO buffer layer no nucleation will take place. Also apparent in this image is the lack of alignment in the nanowires grown, since ZnO and Si/SiO_2 are not epitaxially matched. Figure 3.16 shows the same sample from above, illustrating not just the lack of alignment present on this sample but also the uniformity. This sample is typical of those grown in this way, exhibiting full substrate nanowire coverage.

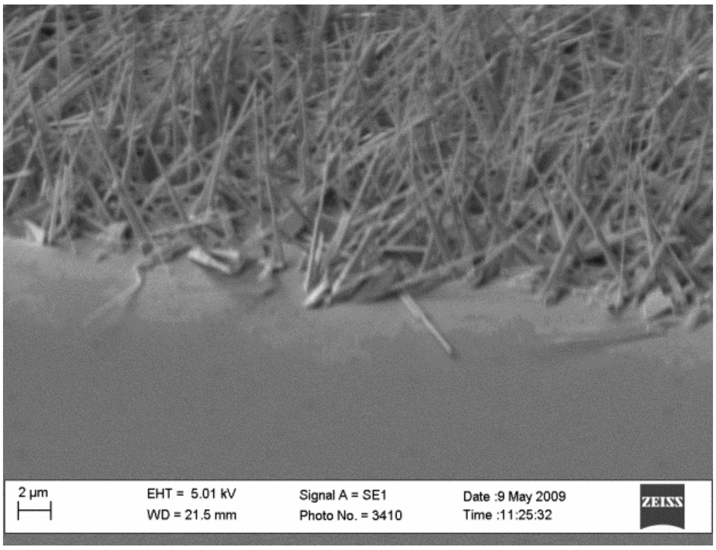

Figure 3.15: ZnO nanowire array grown by CTR-VPT on Si/SiO_2 substrate which has been catalysed with a deposited layer of Au. Top of image shows nanowire growth from catalysed region while bottom shows an area where Au was not deposited and subsequently no ZnO deposition occurred.

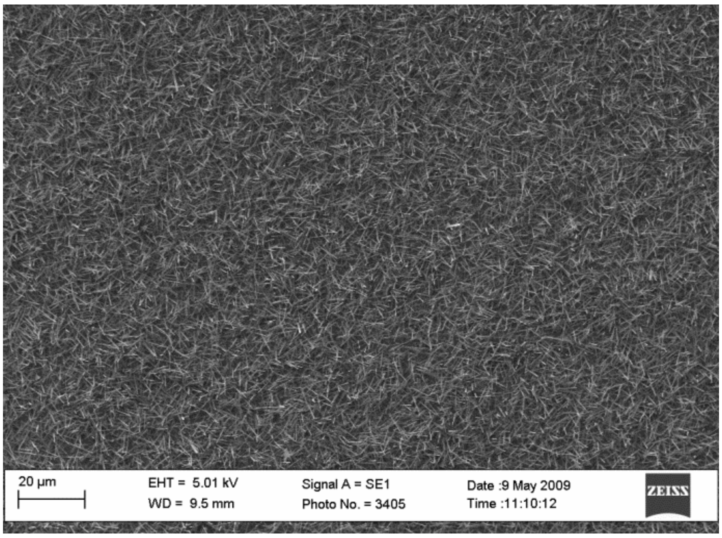

Figure 3.16: ZnO nanowire array grown on Au catalysed Si/SiO_2 substrate. The substrate is very uniformly covered in this mode of growth but there is no vertical alignment.

Nanowires grown using VLS on Si/SiO_2 were generally catalysed using a layer of Au of nominal thickness in the range 5 – 10 nm, measured using a quartz resonator thickness monitor. It is believed that Au layer thickness has an impact on the diameter of any nanowires subsequently grown [31], however within the Au film thickness range used in this work, no significant dependency was observed.

The use of Au to catalyse growth on epitaxially matched substrates was also investigated. ZnO buffer layers deposited using PLD were coated with Au layers, again with nominal thickness of 5 – 10 nm. Figure 3.17 shows an example of a nanowire array produced using an Au layer of 10 nm nominal thickness. In general it can be seen that the nanowires are quite well aligned but as with the nanowires seen in figures 3.15 and 3.16 above they are very long. Au catalysed depositions, under the growth conditions generally used in our laboratory, tend to produce quite long nanowires, up to tens of microns in length. One drawback of nanowires of this length is that they tend to bend under their own weight; this is seen in figure 3.18 where a number of nanowires that were originally vertically aligned are lying at some angle with respect to the substrate. This tendency may be mitigated by controlling the Zn vapour incident on the substrate. Given the equipment used in this work there is no way to directly control this, but indirect methods such as altering the placement of the sample with respect to the source materials, reducing the quantity of source materials, or altering the furnace temperature ramp rate may be attempted in order to reduce the length of nanowires. This point is elaborated on further in chapter 4.

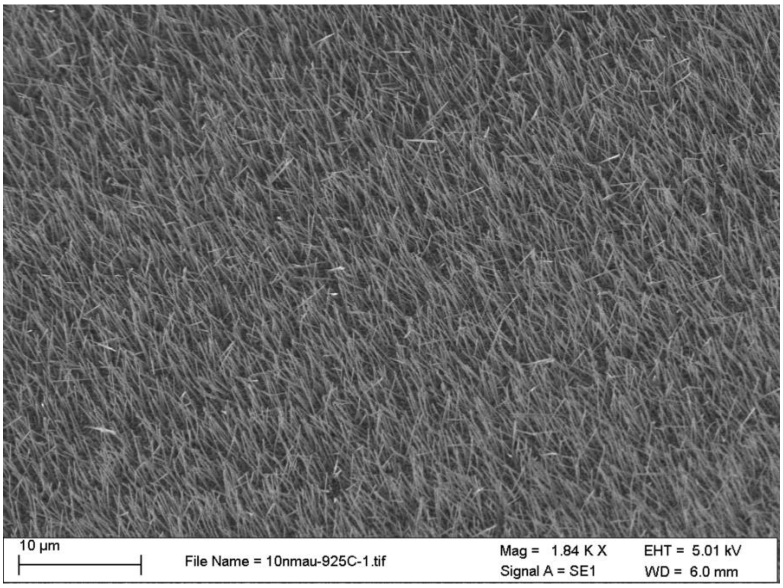

Figure 3.17: CTR-VPT ZnO nanowire array grown on Au catalysed ZnO buffer layer. Quite long and (initially) well aligned nanowires are observed.

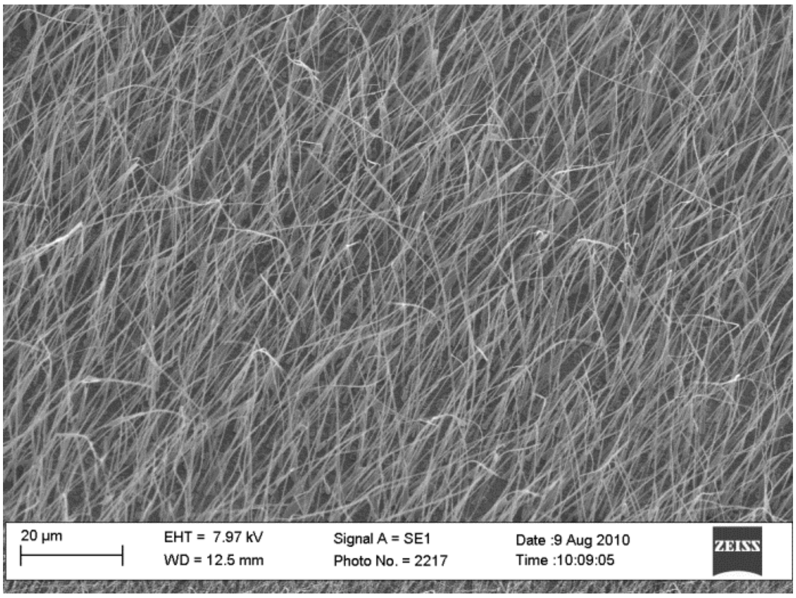

Figure 3.18: CTR-VPT ZnO nanowires grown on Au catalysed ZnO buffer layer. Very long nanowires are seen here, with loss of vertical alignment as wires bend.

Greene *et al.* have suggested that ZnO nanowires may be grown on ZnO buffer layers deposited by Zn acetate CBD with or without the use of metallic catalysts [5, 26]. In that work, the growths were carried out with the substrate placed downstream from the source materials. This is an added complication in the growth process that we believe adds uncertainty to the deposition process. Previous work carried out in our group on PLD produced buffer layers involved the placement of the substrate directly above the powders [25, 32], this simplifies the growth system as vapour concentration varies with distance from source powder [33]. Since buffer layers produced using acetate CBD were found to be essentially identical to PLD layers, both morphologically and by XRD data, CTR-VPT growths were carried out with the substrate directly above the source powders.

Figure 3.19 shows an example of a ZnO nanowire array grown using CTR-VPT on a CBD buffer layer, without the use of a catalyst. Nanowires grown are very uniform over the sample and are extremely well aligned. Figure 3.20 shows a higher magnification SEM image of the same sample showing the exposed edge after cleaving. This shows that the nanowires are very well aligned and also have a tendency to have a wide base which narrows slightly before continuing upwards as a nanowire with a constant diameter. This morphology is common among nanowire arrays grown by CTR-VPT. RT Kumar *et al.* showed that variations in Zn vapour saturation during growth have a large effect on nanowire morphology, with high Zn saturation tending to produce nanowires with wide bases [1]. In that work, saturation was controlled by changing the temperature profile of the furnace used. By measuring the furnace temperature during growth it is possible to determine if a similar effect is occurring here.

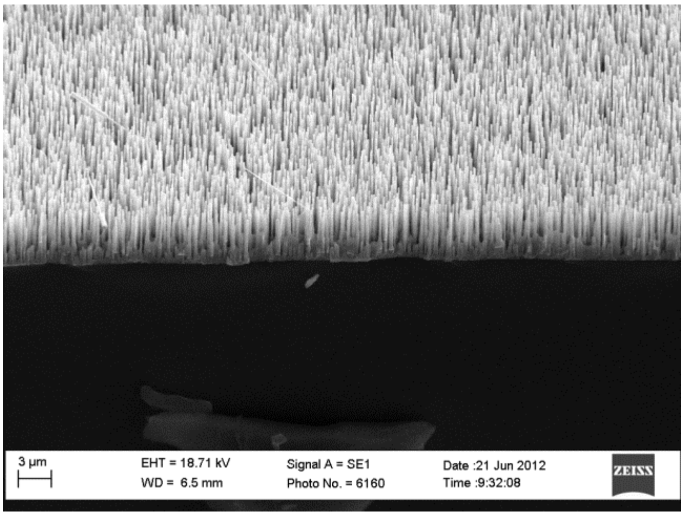

Figure 3.19: ZnO nanowire array grown on CBD ZnO buffer layer by CTR-VPT. Nanowires show very good alignment along with relatively uniform height.

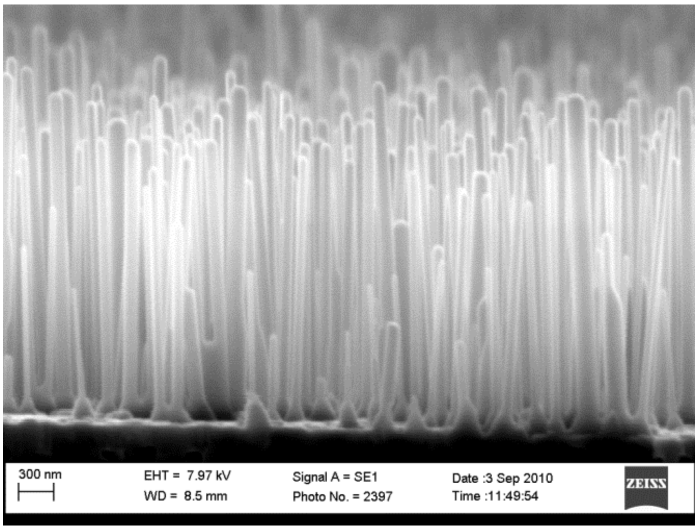

Figure 3.20: Cross section SEM image of the CTR-VPT as seen in figure 3.19. Very good alignment is seen. The nanowires are wider at the bottom before narrowing to a constant thickness growth mode.

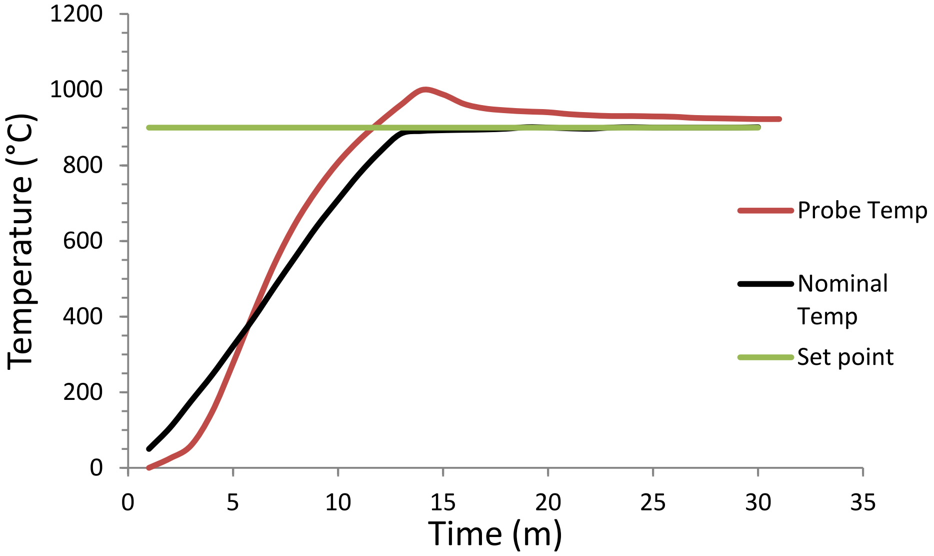

Figure 3.21: Temperature ramp profile of CTR-VPT furnace set to 900°C. Actual temperature was measured using a thermocouple probe while nominal temperature was displayed on the furnace PID controller

Figure 3.21 shows a graph of furnace temperature, with the furnace set-point being 900°C, the temperature of a typical CTR-VPT deposition. In blue, we see the evolution over time of the nominal furnace temperature as displayed on the system's PID temperature controller. In red, the system temperature, as measured using a thermocouple probe is shown. We can see clearly that the actual temperature, as measured by the probe, overshoots the desired temperature by some amount (generally by 100 - 150°C depending on furnace set-point). It is possible that during this initial peak in temperature that there is a greater Zn vapour saturation which leads to wide bases, which then narrow to a constant diameter as the temperature stabilises. This would be consistent with the results seen by Kumar *et al.* as they observe narrower bases when the temperature is slowly ramped up (eliminating the overshoot) to the desired growth temperature [1].

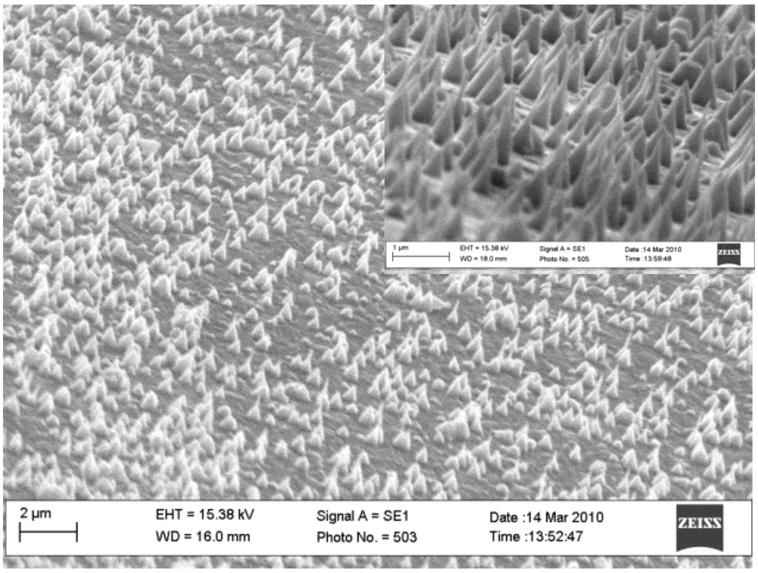

Figure 3.22: Conical ZnO structures grown by CTR-VPT when a reduced quantity of source powders was used. The inset shows a higher magnification image with greater tilt showing the tapering of the structures.

Altering the quantity of source materials used also has an impact on the morphology of nanowires grown. If a greater amount of ZnO/graphite powders are used, more growth takes place, with longer nanowires deposited, as might be expected. However when a smaller amount of powders is used, very different morphologies may be observed, as demonstrated by figure 3.22. In this case 20 mg each of ZnO and graphite powders were used, one third of the 60 mg used in standard depositions. We can see that instead of the expected nanowire growth, the sample is covered relatively uniformly with conical structures, which taper to a point in most cases or continue to grow a short nanowire from their tips. The explanation for this morphology is similar to the wide bases as seen in Kumar *et al.*[1]. It is reasonable to assume that the smaller amount of source material is being vaporised in a shorter time than conventional depositions, leading to an initially high Zn saturation which then drops quickly down to a much lower level.

While CTR-VPT nanowire arrays grown on ZnO buffer layers tend to be quite uniform over the area of any given sample, there does tend to be some variation in morphology between samples grown at different times, even when the deposition is carried out using the same growth parameters (source powders, temperature, ramp-rate, nominal Ar flow, origin of buffer layer used etc.) – i.e. run to run variations. Figure 3.23 shows an example of a nanowire array grown under nominally identical conditions to those for the sample shown above in figure 3.19. There are differences in array morphology, such as array density and nanowire length, despite the nominally similar growth conditions. There are a number of possible reasons for this variation. Firstly, when the source powders are being prepared they are mixed using a pestle and mortar. It has been observed that variations in mechanical mixing may be reflected in the morphology of the arrays grown, with more thoroughly mixed powders leading to a greater amount of deposition on the substrate. This is possibly due to an increased contact area between the two powders, facilitating the CTR reaction more readily. This parameter cannot be controlled exactly by mechanical mixing in a pestle and mortar and as such variations are to be expected. Secondly, as CTR-VPT depositions are carried out on ZnO buffer layers which may have variations such as thickness and crystallite size, these too may cause variations to be seen in subsequent nanowire growths. For these reasons it is important, especially for the purposes of field emission measurements, to implement a technique to control array density, since any two CTR-VPT samples may show significant variations.

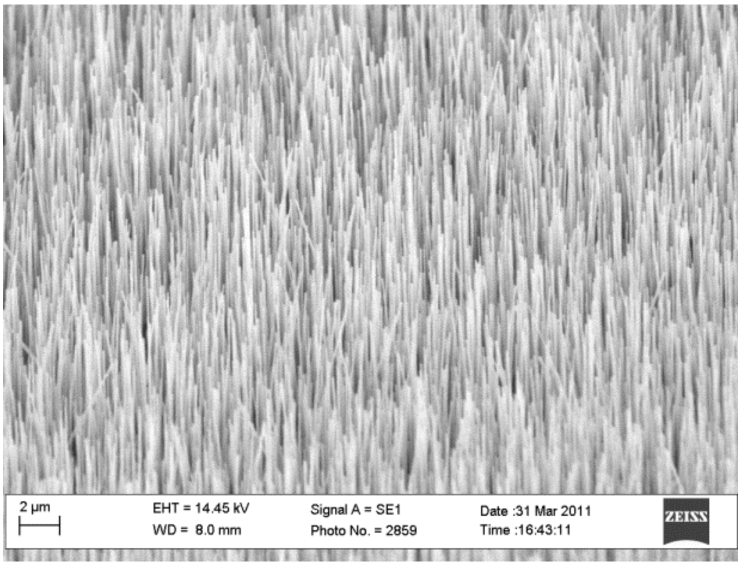

Figure 3.23: Example of ZnO nanowire array grown by CTR-VPT on Zn acetate CBD buffer layers. This sample was grown using typical CTR-VPT parameters (900°C, 60 mins, 60 mg of each ZnO and graphite powders).

Figure 3.24 shows XRD data of the CTR-VPT nanowire sample shown in figure 3.23 above. This is a well textured sample, with a rocking curve FWHM of 5.2°, which is narrower than that of the CBD buffer layer it is grown upon. It is possible that the high temperatures of CTR-VPT deposition allowed for some thermal diffusion, grain coarsening and other effects, resulting in a greater degree of c-axis alignment.

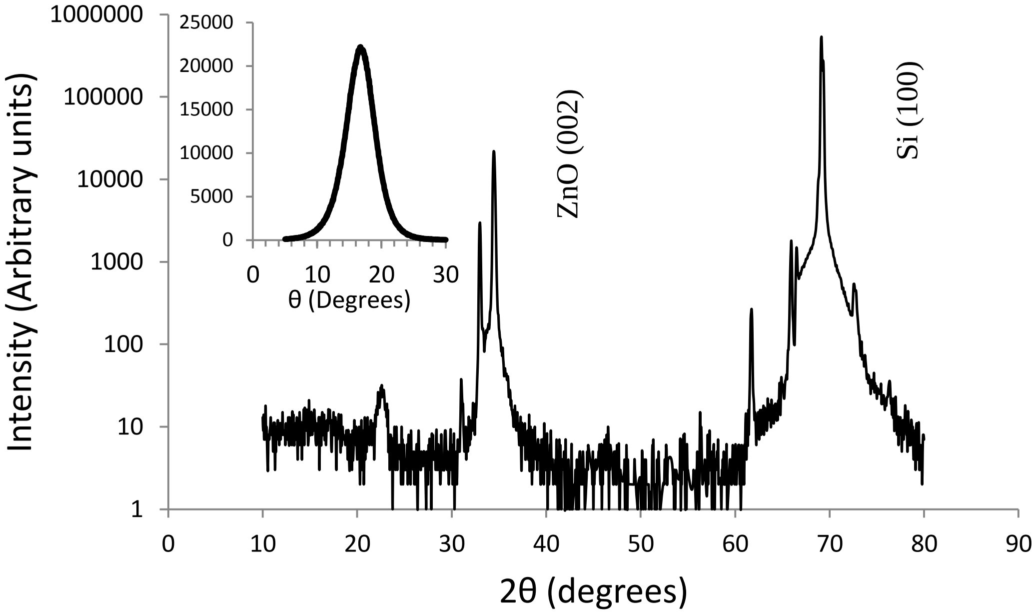

Figure 3.24: XRD θ-2θ scan of CTR-VPT ZnO nanowire array grown on Zn acetate CBD buffer layer. The inset shows the rocking curve data taken using the 34.4° ZnO (002) plane with linear y-axis.

It is important to note that while CTR-VPT may be used to grow arrays of high quality vertically aligned nanowires quite reliably; the reaction taking place is easily poisoned by other chemicals which may be found in a materials preparation laboratory. For this reason it is very important that all equipment associated with the CTR-VPT growth system such as the pestle and mortar, micro-spatulas, alumina boats etc. are washed thoroughly before use and stored separately from other materials. In particular metals may poison the growth reaction such that nanowires are no longer the preferred growth mode.

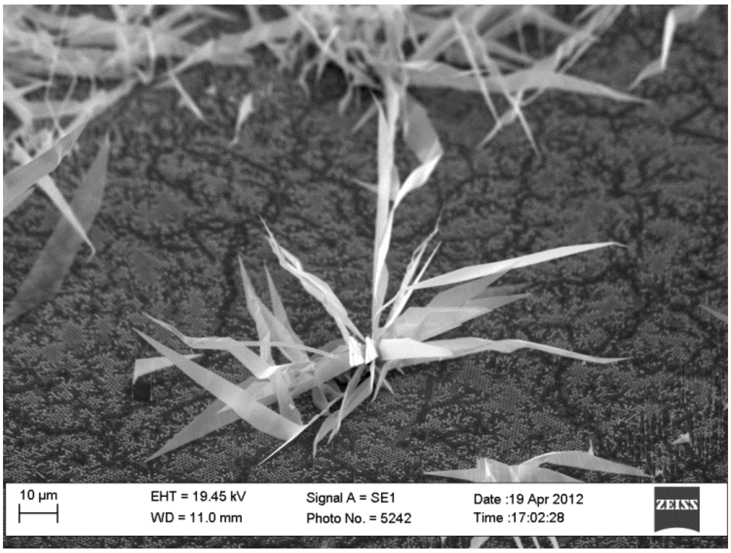

Figure 3.25: SEM image of CTR-VPT deposited structure, believed to be caused by indium contamination in the growth system.

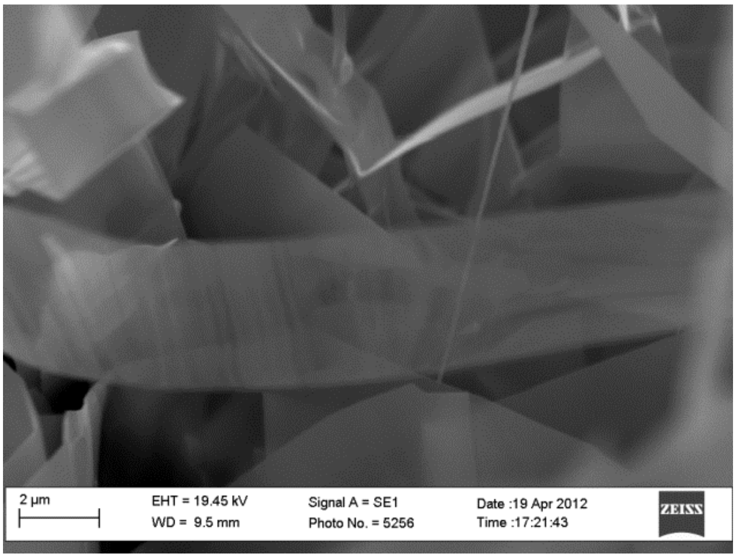

Figure 3.26: SEM image of ZnO nanoribbon, on same sample as figure 3.25 above. This ribbon morphology is consistent with indium contamination

Figures 3.25 and 3.26 show examples of unusual CTR-VPT depositions that are suspected to have been the result of indium entering the growth system. The presence of indium in the growth system is observed to change the preferred mode of growth from nanowire growth to thin nanoribbon growth. This change has been modelled by Fan *et al.* and is explained by a shift from c-axis growth to a-axis growth [34].

3.4 Conclusions

In this chapter, we have examined the deposition of c-axis aligned ZnO buffer layers using two distinct techniques. The first of these techniques is PLD, which allowed for the deposition of well textured ZnO thin films, with relatively uniform thickness and morphology over substrates of areas up to ~ 10 cm^2. We have also seen that morphologically similar ZnO layers may be deposited using a CBD technique, which is deposited using a two step process. The seed layer is deposited first from an alcoholic solution of Zn acetate. This seeded substrate is then deposited upon by any one of a number of possible CBD solutions to achieve the deposition of a ZnO thin film. Out of the different solutions investigated, a Zn acetate derived solution was used predominantly during this work. The choice was made due to the uniformity of deposition and flat morphology which allows for the use of an inverse nanosphere lithography technique which will be explored further in the next chapter.

We have also investigated the use of two separate techniques for the deposition of ZnO nanowires. The first is a CBD technique, using the same solution concentration and temperatures as used for buffer layer deposition. This technique yields arrays of very uniform nanowires, particularly in terms of nanowire length.

Again, as with buffer layer deposition there was a number of other possible CBD solutions that may have also yielded nanowire array growth. However due to incompatibility with the nanosphere lithography technique (to be described in the next chapter) these were not investigated further to any great extent.

The second nanowire deposition technique investigated was CTR-VPT; this allowed for the deposition of arrays of highly uniform and well aligned nanowires with aspect ratios much higher than those produced using the CBD technique. While the method appears straightforward, in practice there are a number of factors that affect the resulting nanowire depositions, including growth temperature, position of the substrate with respect to source materials and quantity of source materials used. When these factors are well controlled, this method yields nanowire arrays with high uniformity and very good *c*-axis alignment. CTR-VPT growths were carried out on ZnO buffer layers produced by CBD and PLD and no significant variation in array morphology was observed.

3.5 References

1. Rajendra Kumar, R.T., et al., *Control of ZnO nanorod array density by Zn supersaturation variation and effects on field emission.* Nanotechnology, 2007. **18**(21).

2. O'Haire, R., et al., *Growth of crystalline ZnO nanostructures using pulsed laser deposition.* Superlattices and Microstructures, 2006. **39**(1–4): p. 153-161.

3. Zhao, J.-L., et al., *Structural, optical and electrical properties of ZnO films grown by pulsed laser deposition (PLD).* Journal of Crystal Growth, 2005. **276**(3–4): p. 507-512.

4. McCarthy, E., et al., *Effects of the crystallite mosaic spread on integrated peak intensities in 2θ–ω measurements of highly crystallographically textured ZnO thin films.* Journal of Physics D: Applied Physics, 2011. **44**(37): p. 375401.

5. Greene, L.E., et al., *General route to vertical ZnO nanowire arrays using textured ZnO seeds.* Nano Letters, 2005. **5**(7): p. 1231-1236.

6. Chu, M.-H., et al., *Catalyst-Free Patterned Growth of Well-Aligned ZnO Nanowires on ITO Substrates Using an Aqueous Solution Method and Lithography Process.* Journal of Nanoelectronics and Optoelectronics, 2010. **5**(2): p. 186-190.

7. Wang, M., et al., *Seed-layer controlled synthesis of well-aligned ZnO nanowire arrays via a low temperature aqueous solution method.* Journal of Materials Science: Materials in Electronics, 2008. **19**(3): p. 211-216.

8. Wu, W.-Y., C.-C. Yeh, and J.-M. Ting, *Effects of Seed Layer Characteristics on the Synthesis of ZnO Nanowires.* Journal of the American Ceramic Society, 2009. **92**(11): p. 2718-2723.

9. Lee, Y.-J., et al., *Tunable Arrays of ZnO Nanorods and Nanoneedles via Seed Layer and Solution Chemistry.* Crystal Growth & Design, 2008. **8**(6): p. 2036-2040.

10. Byrne, D., et al., *A novel, substrate independent three-step process for the growth of uniform ZnO nanorod arrays.* Thin Solid Films, 2010. **518**(16): p. 4489-4492.

11. Deegan, R.D., et al., *Capillary flow as the cause of ring stains from dried liquid drops.* Nature, 1997. **389**(6653): p. 827-829.

12. Stairs, R.A., W.T. Rispin, and R.C. Makhija, *Surface tension of some non-aqueous salt solutions.* Canadian Journal of Chemistry, 1970. **48**(17): p. 2755-2762.

13. Vuilleumier, R., et al., *Tears of wine: the stationary state.* Langmuir, 1995. **11**(10): p. 4117-4121.

14. Byrne, D., et al., *A catalyst-free and facile route to periodically ordered and c-axis aligned ZnO nanorod arrays on diverse substrates.* Nanoscale, 2011. **3**(4): p. 1675-1682.

15. Govender, K., et al., *Understanding the factors that govern the deposition and morphology of thin films of ZnO from aqueous solution.* Journal of Materials Chemistry, 2004. **14**(16): p. 2575-2591.

16. Matijevic, E., *Preparation and properties of uniform size colloids.* Chemistry of Materials, 1993. **5**(4): p. 412-426.

17. Cho, S., et al., *Precursor Effects of Citric Acid and Citrates on ZnO Crystal Formation.* Langmuir, 2009. **25**(6): p. 3825-3831.

18. Zhu, Y.W., et al., *Efficient field emission from ZnO nanoneedle arrays.* Applied Physics Letters, 2003. **83**(1): p. 144-146.

19. Zhang, Z., et al., *The influence of morphologies and doping of nanostructured ZnO on the field emission behaviors.* Solid-State Electronics, 2009. **53**(6): p. 578-583.

20. Liao, L., et al., *Electron field emission studies on ZnO nanowires.* Materials Letters, 2005. **59**(19–20): p. 2465-2467.

21. Garry, S., et al., *Control of ZnO nanowire arrays by nanosphere lithography (NSL) on laser-produced ZnO substrates.* Applied Surface Science, 2011. **257**(12): p. 5159-5162.

22. Peterson, R.B., C.L. Fields, and B.A. Gregg, *Epitaxial Chemical Deposition of ZnO Nanocolumns from NaOH Solutions.* Langmuir, 2004. **20**(12): p. 5114-5118.

23. Verges, M.A., A. Mifsud, and C.J. Serna, *Formation of rod-like zinc oxide microcrystals in homogeneous solutions.* Journal of the Chemical Society, Faraday Transactions, 1990. **86**(6): p. 959-963.

24. Geng, C., et al., *Well-Aligned ZnO Nanowire Arrays Fabricated on Silicon Substrates.* Advanced Functional Materials, 2004. **14**(6): p. 589-594.

25. Biswas, M., E. McGlynn, and M.O. Henry, *Carbothermal reduction growth of ZnO nanostructures on sapphire—comparisons between graphite and activated charcoal powders.* Microelectronics Journal, 2009. **40**(2): p. 259-261.

26. Yang, P., et al., *Controlled Growth of ZnO Nanowires and Their Optical Properties.* Advanced Functional Materials, 2002. **12**(5): p. 323-331.

27. Biswas, M., et al., *Carbothermal reduction vapor phase transport growth of ZnO nanostructures: Effects of various carbon sources.* Journal of Applied Physics, 2009. **105**(9).

28. Dong Jun, P., et al., *Synthesis and microstructural characterization of growth direction controlled ZnO nanorods using a buffer layer.* Nanotechnology, 2006. **17**(20): p. 5238.

29. Li, C., et al., *Effect of Seed Layer on Structural Properties of ZnO Nanorod Arrays Grown by Vapor-Phase Transport.* The Journal of Physical Chemistry C, 2008. **112**(4): p. 990-995.

30. Kumar, R.T.R., et al., *Growth of ZnO nanostructures on Au-coated Si: Influence of growth temperature on growth mechanism and morphology.* Journal of Applied Physics, 2008. **104**(8): p. 084309-11.

31. WangWang, et al., *Density-Controlled Growth of Aligned ZnO Nanowires Sharing a Common Contact: A Simple, Low-Cost, and Mask-Free Technique for Large-Scale Applications.* The Journal of Physical Chemistry B, 2006. **110**(15): p. 7720-7724.

32. Grabowska, J., et al., *Surface excitonic emission and quenching effects in ZnO nanowire/nanowall systems: Limiting effects on device potential.* Physical Review B, 2005. **71**(11): p. 115439.

33. Li, C., et al., *Effect of substrate temperature on the growth and photoluminescence properties of vertically aligned ZnO nanostructures.* Journal of Crystal Growth, 2006. **292**(1): p. 19-25.

34. Fan, H.J., A.S. Barnard, and M. Zacharias, *ZnO nanowires and nanobelts: Shape selection and thermodynamic modeling.* Applied Physics Letters, 2007. **90**(14): p. 143116-3.

Chapter 4: Nanosphere Lithography

4.1 Introduction

This chapter describes a technique for controlling the spacing and morphology of ZnO nanostructures grown by both the CTR-VPT and CBD deposition techniques. It is possible to control both the alignment and spatial ordering of nanorods grown using NSL in combination with these techniques. For a number of possible applications of ZnO nanowires, high crystal quality, high degrees of alignment, and precise control over nanorod array density are required. Examples of such applications include field emission and optoelectronic devices such as solar cells [1-4]. Control of this nature has been previously demonstrated using techniques such as nanosphere lithography, laser interference lithography and carbonised photoresist lithography [2, 5-11]. The work described in this thesis represents advancement in the use of NSL with respect to the growth of ordered arrays of ZnO nanostructures for field emission characterisation. The motivation for using NSL is that it is common for ZnO nanowire samples, even ones grown under similar conditions, to have a large variance in array density, particularly with the CTR-VPT technique. This complicates characterisation as results from techniques such as field emission (FE) where performance may depend on array density due to screening/shielding effects [12]. By removing the variability of nanowire density using NSL we can enable direct comparison between samples of various morphologies or crystal qualities.

To date, the majority of reports using NSL to produce ordered arrays of nanostructures have done so by depositing spatially ordered arrays of metallic catalyst points (such as Au or Ni) [6-8, 13, 14]. This relies on the use of a close packed array of nanospheres. The catalyst material is deposited through the pores of this mask leaving an array of triangular islands on the substrate. A vapour-liquid-solid (VLS) growth technique can then be used to produce an array of nanostructures that follows the pattern produced by the nanosphere shadow mask. However, this method does not offer control over the alignment of nanostructures. In order to achieve vertical alignment a substrate with sufficiently close epitaxial matching must be used [15].

This chapter describes two distinct methods of producing ordered arrays of nanowires using NSL. The first of these uses nanosphere monolayers to produce arrays of Au catalyst points from which spatially ordered arrays of ZnO nanowires are grown using CTR-VPT only, as outlined above. These growths are carried out on both Si and ZnO buffer layers. The second technique was the use of a silica secondary mask, creating a template which allows for both CTR-VPT and CBD deposition of ZnO nanowires.

NSL exploits the tendency of small spheres (micro-/nano-sized) of some materials to self-assemble into close-packed arrangements. It is most often based on the creation of a single close-packed monolayer, although there are reports in the literature that utilise multi-layers to create more intricate shadow masks [16]. When a collection of uniform spheres is forced together into their most dense arrangement the packing fraction is ~0.74. This packing fraction is achieved by both the Hexagonal Close Packed (HCP) and Face-Centred Cubic (FCC) configurations however for a monolayer these configurations are identical and differ only in multilayer stacking., For shadow lithography, the nanosphere layer may be treated as a 2D projection on the substrate surface, since in the majority of cases the catalyst material deposited through the mask will be incident normal to the substrate; the packing fraction of ~0.91, means that ~9% of the substrate will be coated by catalyst material.

NSL is useful for the growth of nanostructure arrays with controllable inter-wire spacing. This is due to the direct relationship between the radius of the spheres used and the size and position of the apertures in the array. Absolute spatial control with respect to fiducial markers on the substrate is not achievable through this method but control of nanostructure position relative to other such structures is achieved. It has been reported that through the combination of NSL with other techniques, such as RIE etching and varying the angle of incidence of catalyst material during deposition, that patterns such as honeycombs, rings, and lines can be produced, in addition to the more normal, close to triangular shapes [17, 18].

There is a wide variety of techniques used in the literature to generate close-packed nanosphere monolayers, including controlled evaporation of colloidal solutions, dip-coating, spin coating, Langmuir-Blodgett deposition, and self-assembly on the surface of water [16, 19-23]. While these methods are distinct from each other, in each case a force acts upon the spheres to push them into their most densely packed configuration. It is the nature of this force that varies between each technique. During nanosphere deposition by spin-coating, it is the centrifugal force of the spinning motion that drives the spheres closer together, generating the HCP structure. Langmuir-Blodgett deposition provides this force mechanically, after dispersing nanosphere solution on the surface of water, a PTFE arm is used to compress the film into the densest packing configuration. In the case of self-assembly on the surface of water, it is the repulsive forces between the spheres and the water, caused by the hydrophobicity of the polystyrene spheres. Nanospheres applied gently to the water surface self-organise and form a close packed monolayer. Self-assembly on the surface of water, developed by Rybczynski et al [22], has been found in this work to be the simplest method, both in terms of quality of monolayers produced and most efficient in terms of materials usage. The close packed monolayer can then be transferred from the surface of the water onto substrates.

4.2 Self-assembly of nanosphere monolayers

Three approaches were taken in this work to produce HCP monolayers. By far the most successful of the three was the self-assembly of monolayers on the surface of water. The other two methods investigated were spin-coating and drop coating. Spin coating was attempted while varying a wide range of parameters, including nanosphere solution concentration, dilution of solution in ethanol, spin speeds, multiple spin stages, and volume of nanosphere solution used. Some success was achieved with this technique; however the areas of monolayer produced were consistently small, with large areas of the sample either covered with multilayers or showing an absence of nanospheres. The addition of the surfactant SDS significantly altered the results of this technique, reducing the incidence of multilayer deposition. However this addition did not achieve full sample coverage. Furthermore, the use of a base piranha solution to produce a more hydrophilic substrate surface was also required. This surface treatment was found to be incompatible with the ZnO buffer layers required to catalyse the growth of nanostructures post-patterning because it etched these buffer layers significantly.

The second technique investigated was drop-coating. This is an evaporation method where the nanosphere solution was diluted with ethanol to various concentrations and deposited on a sample surface. The evaporation of the ethanol, and water ingress due to the hygroscopicity of ethanol, causes a thin film to form over the substrate. This further evaporates and as it recedes it produces the force required to create a close-packed monolayer. This technique yielded considerably better results than spin-coating and is much simpler to implement. The smaller number of parameters affecting this technique meant that results were more consistent. Large areas are covered by monolayer, but with large uncoated areas also found across the sample. Attempts to mitigate the formation of uncoated regions by increasing the quantity and concentration of the solution applied to the sample increased the prevalence of multilayer formation.

The most successful technique investigated was the self-assembly of spheres on the surface of water, a schematic of the process is shown in figure 2.4. Similar to the well known Langmuir-Blodgett technique [23] which is widely used for monolayer deposition of many materials, it involves the gentle application of an ethanol/water/nanosphere solution to the surface of water. The solution then disperses across the surface with the ethanol evaporating from the surface or mixing into the bulk of the water, leaving only nanospheres at the air-water interface. Continued application of solution to the surface of the water increases the density of spheres to a point where they begin to close pack. This can be observed visually due to the opalescent effects of highly periodic arrays on this scale as shown in figure 4.1. At this point a highly multi-crystalline layer with significant defects such as domain boundaries and regions of multilayers has been produced. The size of domains can then be increased by the creation of water surface fluctuations by gently moving the dish. This allows spheres to rearrange into a lower energy configuration which, due to hydrophobic forces, is close packed. Unlike the other techniques, self-assembly on the surface of water also allows for the mitigation of multilayers by creating a gentle current in the water bulk, dispersing extra spheres into the bulk. Further compression can be achieved with the addition of a surfactant such as SDS or Triton-X100. This serves two purposes, firstly it consolidates the monolayer, increasing the domain sizes and secondly the force generated pushes the monolayer against the wall of the containing vessel, thereby anchoring it in place and enabling precise transfer of the monolayer to the substrate. Areas of square packed (i.e. not hexagonally close packed) nanospheres are sometimes observed with all three techniques investigated, however this is not observed in samples created using the self-assembly technique when a surfactant is used to compress the monolayer. The transfer from the air-water interface to substrate surface is carried out by introducing the sample into the water bulk through an area uncovered by nanospheres. The sample is then lifted gently out of the water through the desired area of monolayer. The sphere layer in its close packed state behaves like a film and transfers readily to most substrates without the need for prior surface treatment. Silicon, ZnO, glass, and sapphire have been coated this way without the need for any surface modification. Large areas of monolayer may be created using this technique with the only limitation being the size of the vessel used, with areas on the order of tens of cm^2 readily achievable. The water transfer technique was used to deposit nanospheres of diameter 500 nm, 1 µm and 1.5 µm. For both the 500 nm and 1 µm diameter spheres, large areas of nanosphere monolayer were readily produced with few defects. In both cases, domains would be quite large, in some cases on the order of several square millimetres. Figure 4.2 shows an example of a 500 nm nanosphere array. However in the case of nanospheres of 1.5 µm diameter, while monolayers were produced, their quality was significantly worse than the smaller sizes. Samples coated with 1.5 µm spheres would consistently exhibit significantly smaller domains with considerably more defects. All nanospheres used were produced by Thermo-Fisher Scientific and from the same product line (5000 series polymer particle suspension). There are two reasons for the presence of these defects in the larger sphere size. Firstly, a proprietary surfactant is added by the manufacturer to stabilise the suspension and to prevent clumping for these larger size spheres. Thermo-Fisher would not reveal either the surfactant used or its concentration but it was observed during water transfer that the larger spheres reacted much more strongly to the addition of further surfactant, with the monolayer being compressed to the point of collapse. It is believed that this is due to a variance in concentration by the manufacturer of added surfactant across the product line. Due to this, it was not possible to use further surfactant during deposition in order to compress the monolayer; this resulted in less densely packed layers that were easily damaged during transfer. The second reason for the defects observed was that the larger spheres have a slightly larger range of sphere diameters than those seen for smaller spheres. This creates a number of defects that may propagate through a given domain, further reducing the quality of the deposited layer.

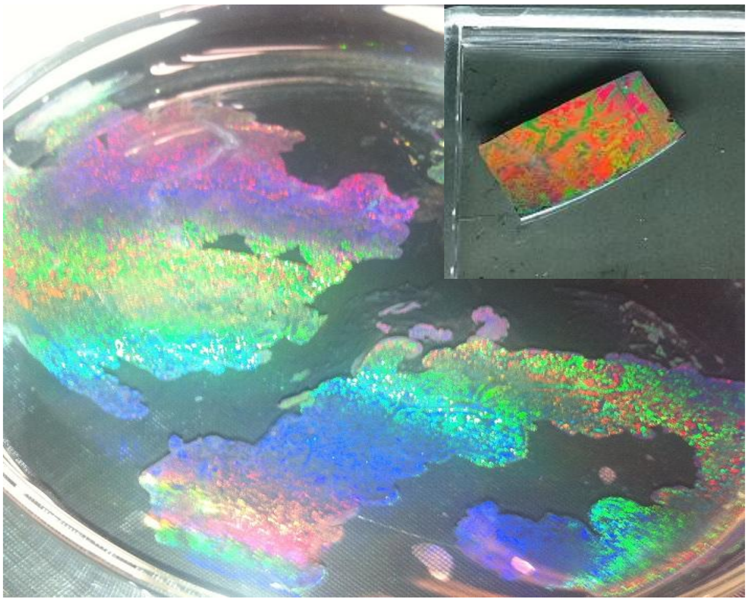

Figure 4.1: Photograph of close packed nanosphere layer on the surface of water, the opalescent effect is indicative of highly period arrays of spheres. Inset is an example of a ZnO buffer layer sample coated with nanosphere layer, also showing opalescent effects.

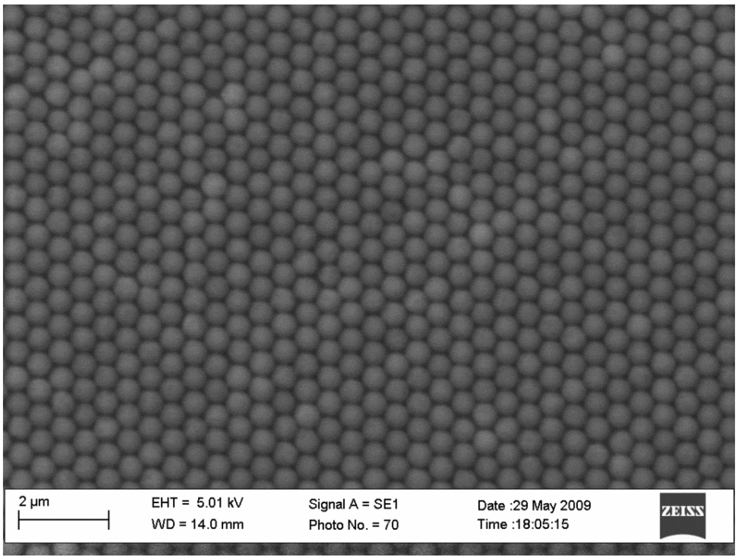

Figure 4.2: SEM image of nanosphere monolayer with spheres of diameter 500 nm.

4.3 Spheres as catalyst mask

In this work, the catalyst used to initiate CTR-VPT growth was Au. This was deposited on the sample surface using thermal evaporation deposition. This technique deposits by line of sight and as the source to sample distance is ~20 cm it is assumed that Au deposited is incident normal to the substrate. Triangular Au islands are deposited, the total area of which represents 9% of the total sample area as this is the area left uncovered by the projection of the hexagonal close packed configuration. After catalyst deposition the spheres are removed revealing the hexagonal array of metal islands as shown in figure 4.3. CTR-VPT growths were then carried out on samples patterned using this technique. Both bare Si wafers and Si wafers coated with ZnO buffer layer by PLD were used.

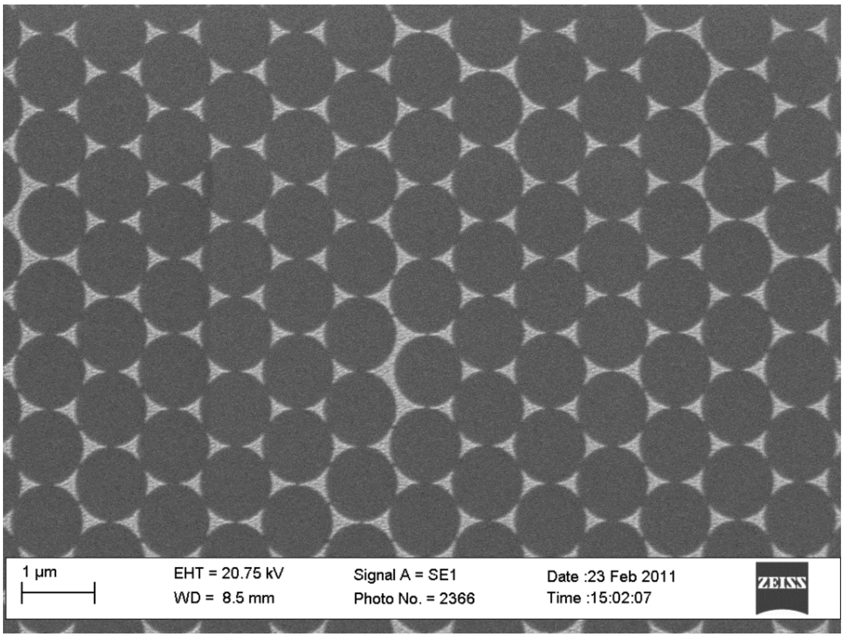

Figure 4.3: SEM image of 5 nm thick Au catalyst pattern as deposited though 1.0 µm diameter nanosphere monolayer.

4.4 NSL on bare Si wafer

CTR-VPT growths in this case were carried out at 900°C for 60 mins. ZnO nanowires growth was achieved; however the patterning was not observable post-deposition. Nanowires grown this way were randomly oriented as Si and ZnO are not closely lattice matched.

Figure 4.4 shows an example of nanowires grown in this way; they are not vertically aligned due to the lattice mismatch between Si/SiO_2 and ZnO. Unexpectedly the positioning of nanowires grown also appears to be random. Annealing Au patterned samples at temperatures achieved during CTR-VPT deposition revealed that the Au islands bead up and become mobile on the sample surface, as shown in Figure 4.5, moving from a hexagonal array to a random distribution. This precluded the possibility of growing ordered arrays on bare Si/SiO_2 with this method.

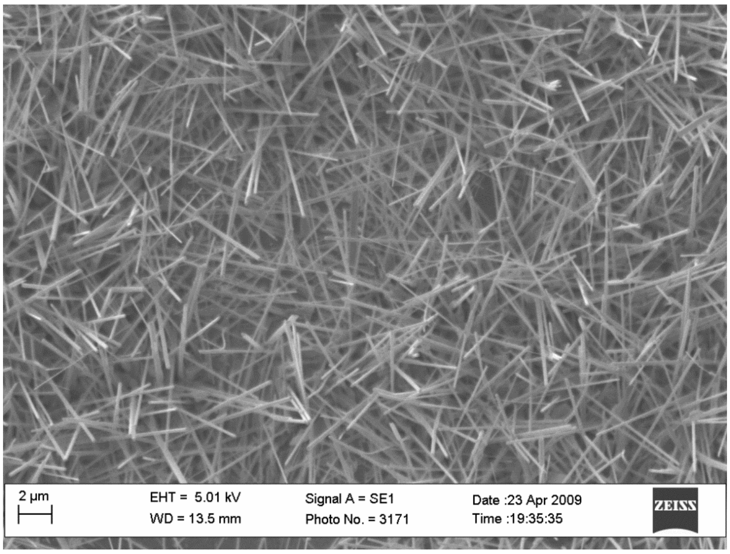

Figure 4.4: SEM image of nanowires grown on bare Si/SiO_2 using an NSL patterned Au catalyst layer.

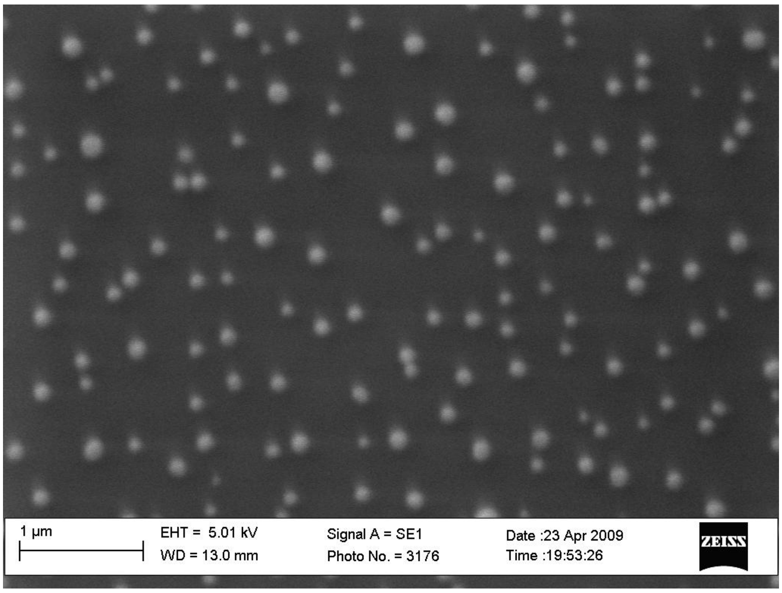

Figure 4.5: Example of an initially NSL hexagonally patterned Au catalyst layer after annealing at growth temperatures. The Au has beaded up and become mobile and thus has not retained the hexagonal patterning. Figure 4.2 shows an example of such a pattern pre-annealing.

4.5 NSL on ZnO buffer layers

CTR-VPT growths carried out on Au patterned ZnO buffer layers produced by PLD were carried out. Growth of vertically aligned nanowires was achieved, however, the desired hexagonal ordering was not observed. The density of growth was very high, as shown in figure 4.6, with more nanowires observed per unit area than the number of Au catalyst points. This was noted for samples produced using spheres of 500 nm and 1 µm diameter. Growth was not confined to the Au patterned regions and occurred across the entire substrate. It was concluded that the Zn pressure was such that nucleation was energetically favourable over the entire surface (both Au and ZnO). While Au provides an energetically favourable nucleation site for ZnO on Si/SiO_2 substrates, nucleation will readily occur on the ZnO buffer layer without the presence of a catalyst given the generally high Zn pressure present during CTR-VPT depositions. This brought about the requirement of control over the Zn pressure in the area immediately around the sample.

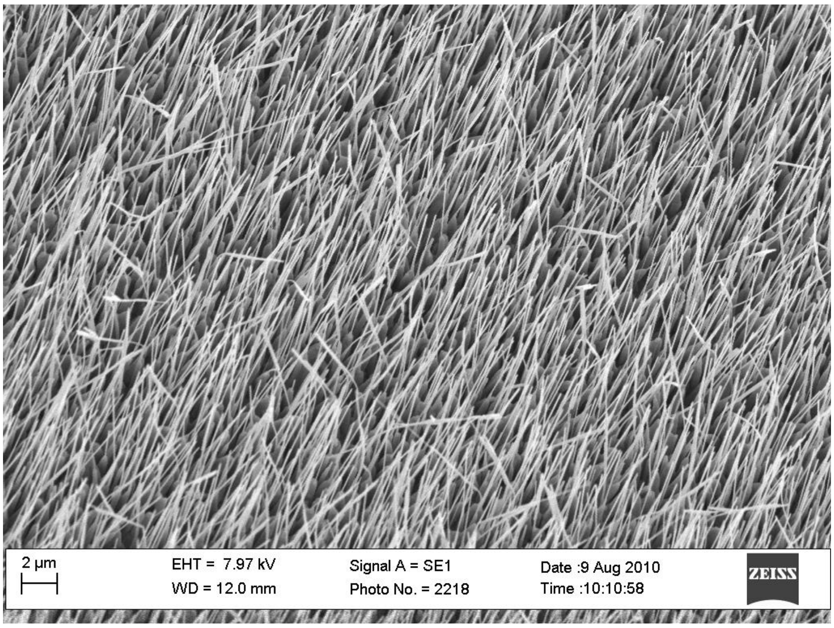

Figure 4.6: Nanowires grown by CTR-VPT on an NSL patterned Au catalyst pattern deposited on a ZnO buffer layer. It is clear in this case that spatially selective deposition has not occurred.

Given the relative simplicity of the CTR-VPT equipment used, no means of directly controlling Zn vapour pressure was available. However two indirect methods of reducing the pressure were investigated. Firstly the orientation of the sample over the source powders was changed. Whereas in the standard procedure for CTR-VPT growth the sample is placed directly over, and facing towards, the powders, in an effort to reduce the vapour at the sample, it was placed in the same position with the ZnO buffer layer facing away from the source material. This resulted in a significant reduction in density of nanowire growth; with much more selective deposition. However a large variance in density of growth occurred over the sample. Predominantly the areas of each sample nearest the edges were covered with significant deposition and long nanowires with deposition not solely occurring at catalyst points. The Zn pressure in these regions is still too high for selective deposition to occur, as shown in figure 4.6. This is in contrast to the deposition observed towards the centre of the sample where nanowire deposition is much more controlled and for the most part maintaining the catalyst pattern, as shown in figure 4.7.

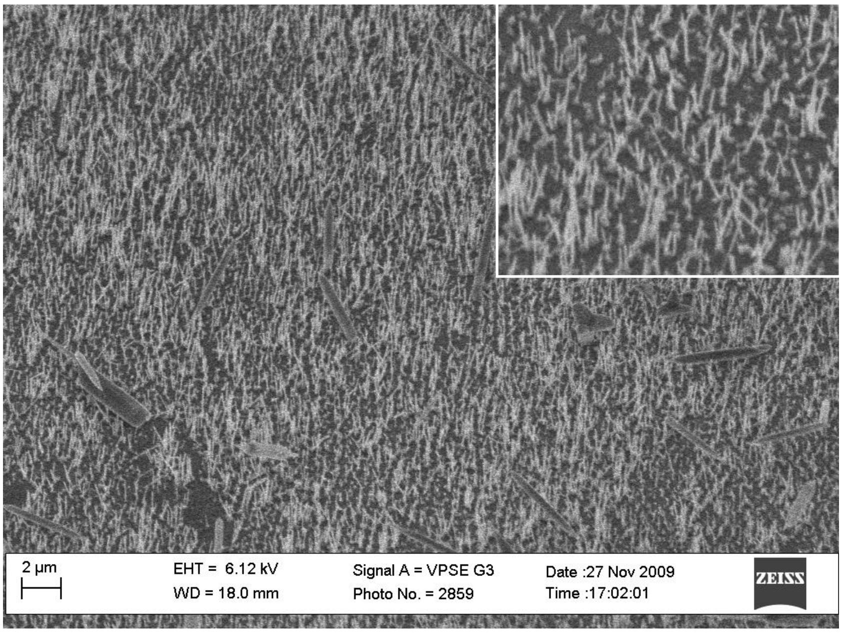

Figure 4.7: Nanowires generally maintaining the NSL pattern, but with multi-wire nucleation at some points. Inset shows an area exhibiting multi-wire nucleation.

The second method investigated was the placement of the sample downstream from the source powders. The sample was placed facing downwards approximately 1 cm from the powders. As in the case where the sample is placed facing away from the powders, this yielded more selective growth. But the areas covered by the desired growth mode were quite small and could generally be divided into three distinct regions described by the density of growth observed. The area of the sample closest to the source powders would invariably have the densest growth, with very long nanowires not maintaining the Au catalyst pattern, once again due to a high Zn pressure which leads to nucleation on the entire ZnO buffer layer. Beyond this region of high density growth there is an area, a few mm in length (~5 mm typically), where the desired growth mode occurs. Here, growth only takes place at Au catalyst points and nanowire growth is close to the desired density. The final distinct region on each sample is furthest away from the source materials. Here, the Zn vapour pressure is too low to initiate any significant nucleation on either the ZnO buffer layer or the Au catalyst covered regions.

While noting that these regions are not absolutely distinct, since there is no definite line between them, there is a significant difference between them and it is worth noting that the region closest to the source material is where the majority of ZnO deposition took place. In this region, VS and VLS deposition takes place on the ZnO buffer layer and on Au catalyst points. Since there is a high Zn vapour concentration here, all ZnO deposited here provides sites for further VS nucleation to occur, leading to a runaway deposition. Beyond this region, the Zn vapour is sufficiently depleted that VS deposition no longer takes place, only VLS deposition will take place on areas pre-coated with Au catalyst points; leading to well patterned nanowire growth. Due to the low percentage of the substrate area being covered with catalyst material, this VLS only growth does not deplete the Zn vapour as completely and allows for an area of acceptable growth much larger than the area of runaway deposition.

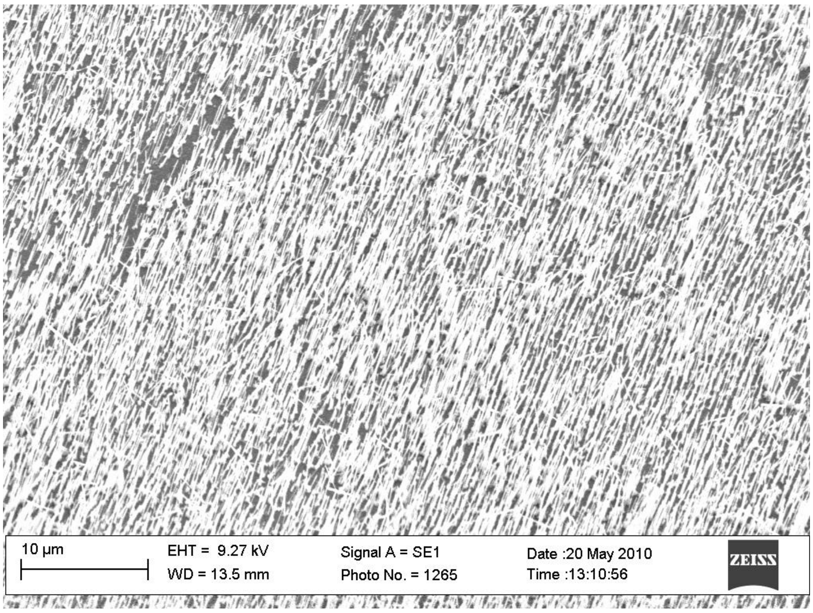

Figure 4.8: NSL patterned nanowire array grown downstream from source material. Generally well ordered but with multiple wires from each nucleation point.

4.6 Angle resolved nanosphere lithography

While providing for reasonably sized areas of selective growth, the size of the Au catalyst point deposited using conventional shadow NSL allows for the growth of multiple nanowires from each point in the catalyst pattern as is apparent in figure 4.8. Samples patterned using nanospheres of diameter 500 nm and 1 µm were grown in this way, however due to the issue of multiple nanowire nucleation, only the larger 1 µm spheres yielded acceptable results since in the smaller 500 nm spacing, the bases of the nanowires grown tended to be on the same scale as the inter-wire separation. This resulted in neighbouring nanowire bases to coalesce, obscuring the pattern.

Further control over the Au catalyst pattern is possible by both varying the angle of Au incidence and by rotating the sample throughout deposition [24]. Due to limitations of equipment at hand, rotation of the sample during deposition was not attempted; however the angle of incidence was varied and was found to have a large impact on the subsequent CTR-VPT growths. Since Au deposition by thermal evaporation is by line of sight, altering the angle of deposition reduces the area of the sample coated and thus limits the Au-coated area available for CTR-VPT deposition. This is illustrated in figure 4.9, where the white areas show where Au will be deposited. θ = 0° is deposition normal to the substrate depositing Au over the largest area possible, while at θ = 45° the nanospheres shadow the entire surface area, blocking all incident Au.

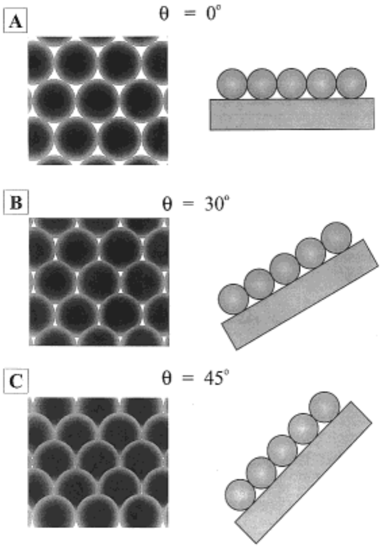

Figure 4.9: Schematic showing area of substrate on to which it is possible to deposit Au depending on angle of incidence. Figure from Haynes *et al.* [24].

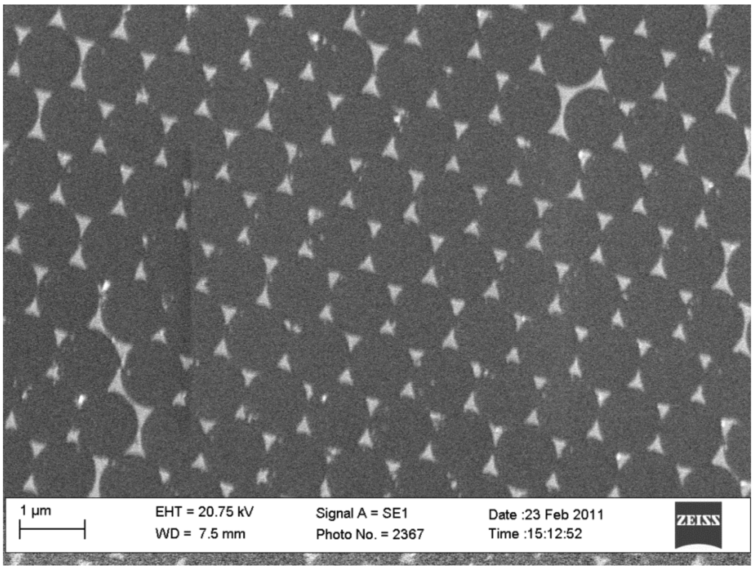

Figure 4.10: SEM image of Au catalyst pattern deposited through 1.0 µm nanosphere mask at angle of ~10°.

Using this angle resolved technique it was possible to greatly reduce the incidence of multi-wire nucleation. Figure 4.10 shows an SEM image of an Au catalyst array deposited using angle resolved NSL showing a reduction in Au island size compared to figure 4.3. The most consistent results were achieved when the angle of incidence was ~ 12°. This compares very favourably to samples grown using normally incident Au, as shown above in figure 4.7. Figure 4.11 and 4.12 show nanowire arrays produced using this technique using nanospheres of diameter 1 µm. This technique was also applied to nanosphere arrays of diameter 500 nm, however the same results were not observed. CTR-VPT growths carried out in this fashion tended to have wide bases that tapered into nanowires as the growth took place. Under the growth conditions used in this work, the bases produced tended to be larger than the spacing between the Au nucleation points when the nanosphere diameter was

500 nm. This produced disordered nanowire growth as the bases of adjacent nanowires tended to coalesce, preventing growth from following the catalyst pattern.

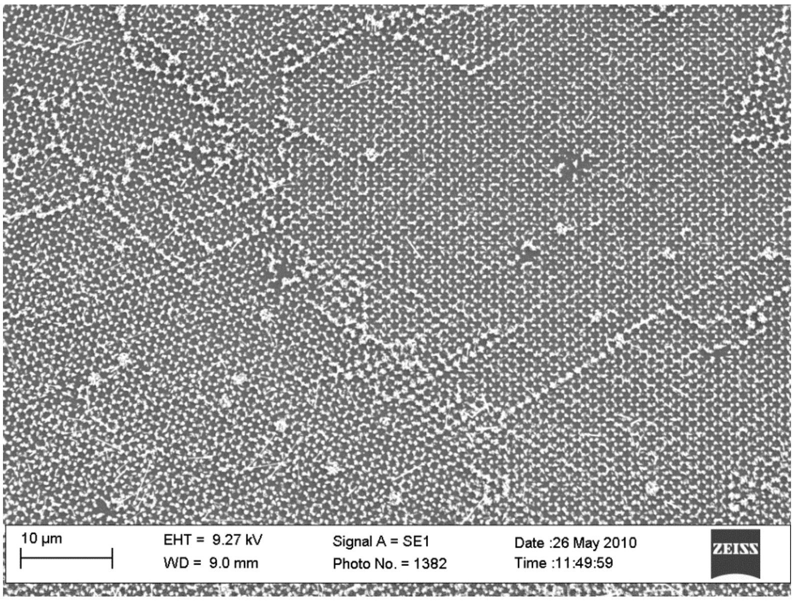

Figure 4.11: SEM image showing single wire nucleation from majority of catalyst points on sample patterned using 1 µm diameter spheres using angle-resolved NSL with an angle of incidence of ~ 12°.

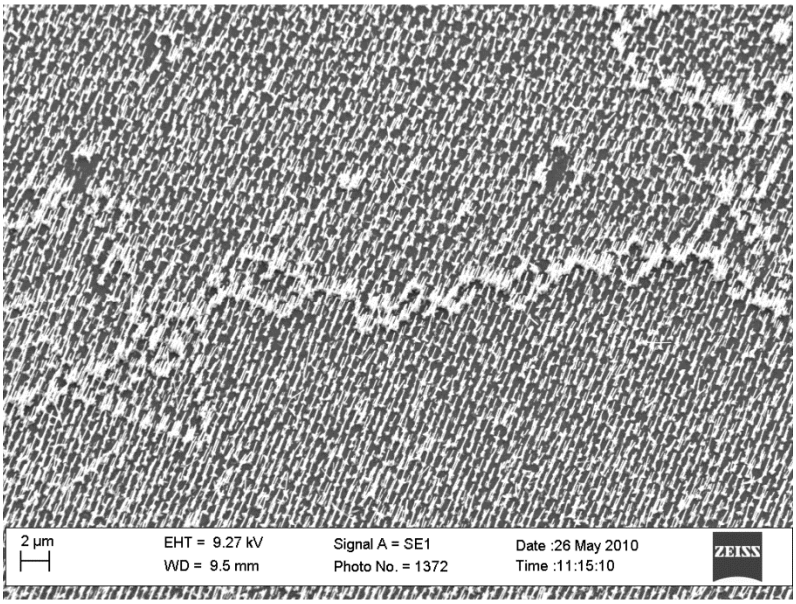

Figure 4.12: SEM image showing single wire nucleation from majority of catalyst points on sample patterned using 1 μm diameter spheres using angle-resolved NSL with an angle of incidence of ~ 12°.

4.7 Inverse nanosphere lithography

Metal catalyst assisted nanosphere lithography allows the growth of ordered nanowire arrays only by using the CTR-VPT technique. Also, while it has been shown to produce highly periodic and uniform arrays, it is prone to defects such as grain boundaries in the nanosphere pattern due to the continuous deposition of catalyst material in areas not directly masked by the nanosphere layer; this is clearly visible in figure 4.12. An inverse nanosphere lithography technique, as developed by Byrne *et al.* [25], was used and further adapted in this work using silica as the secondary mask material. This technique is not prone to as many defects as the Au catalyst technique, since grain boundaries in the nanosphere pattern are effectively masked from ZnO growth. This masking prevents areas of uncontrolled growth occurring, so for this reason, the inverse NSL technique was the focus of the rest of the work into the production of ordered nanowire arrays. A schematic representation of this technique is shown in figure 4.13:

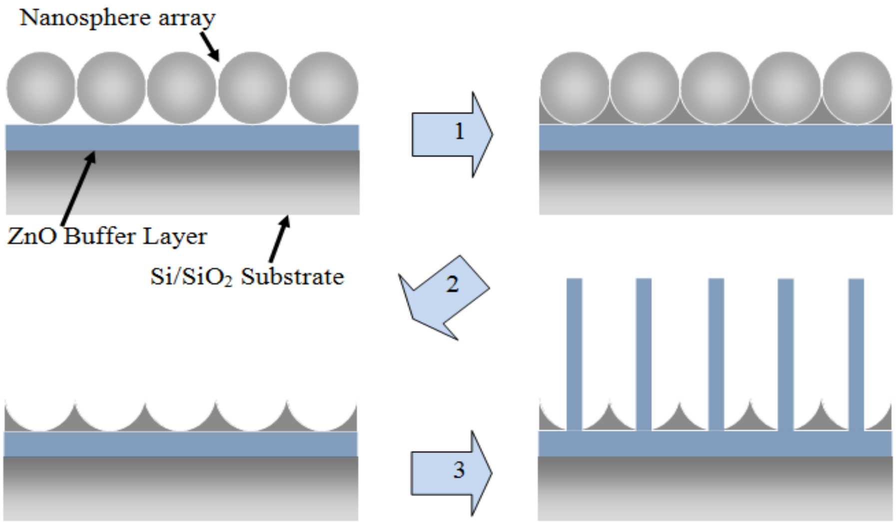

Figure 4.13: Schematic representation of the inverse NSL technique. Starting with a nanosphere coated ZnO substrate, the indicated steps are 1) silica deposition through nanosphere layer, 2) nanosphere removal to reveal patterned silica mask, and 3) nanowire growth through apertures in silica mask by CBD or CTR-VPT.

In addition to the benefit of reduced defects in the nanowire arrays produced, this technique has another possible benefit. In the case of metal catalyst assisted deposition (VLS mechanism) a metal cap is often observed on the tip of nanowires grown. The effect of metal tips on the field emission properties of the arrays produced is not known but their presence at nanowire tips may be detrimental to FE efficiency as sharp facet edges are crucial for FE performance [26]. Furthermore, metal tips are not observed on all nanowires grown in this way and this adds another uncontrolled degree of variability to any field emission studies. By removing this possibility the silica secondary template using VS growth reduces the number of variables to be considered while examining field emission data.

4.8 Deposition of silica secondary mask

The silica sol, as prepared in chapter 2, is dropped onto the nanosphere coated substrate and allowed to dry in air. The sol was prepared using acid as the catalyst. Both HCl and H_2SO_4 were used and no variation was observed between these cases. Once the silica coated nanosphere monolayers had been dried in air and the nanosphere layer removed by ultrasonication in toluene the silica is densified by annealing at a temperature of 450°C. The ramp rate used is of importance here, the silica layer at this point is fragile and prone to cracking. The ramp rate used was 15°C per minute and prevented cracking in the silica layer in the majority of cases. When higher ramp rates were used, the silica layer was observed to crack and delaminate from the sample. The underlying ZnO buffer layer was also observed to delaminate in this case, exposing the Si/SiO_2 substrate. Thickness of the deposited layer is also of critical importance in relation to the issue of cracking and delamination, an example of delamination is shown in figure 4.14, where the right side of the image shows cracking of the mask and the left shows a delaminated area, where the Si/SiO_2 substrate is exposed. If an insufficient volume was not added the centre of the substrate would be covered with a very thin layer which would then be subject to cracking during densification and CTR-VPT growth. In this case delamination would not occur, but the cracks formed in the silica pattern leave underlying ZnO buffer layer exposed, and subsequently lead to unwanted nanowire growth during CBD or CTR-VPT deposition. If, on the other hand, the volume of silica sol applied to the substrate was too great, other defects were observed to occur. Upon drying, spots would appear, predominantly at the substrate edge which would then subsequently crack and delaminate during densification or growth. In addition to this, if too much silica sol is applied, the silica layer will entirely cover the nanosphere layer in places preventing any growth from occurring in that area. Furthermore, the volume of sol required depended on the diameter of nanosphere used, with larger spheres requiring more than smaller ones. Finally, the shape of substrate used also had an effect on the volume of sol required. In all cases it was observed that in drying, the silica layer deposited would be thickest towards the sample edge, the wider the substrate used, the more sol was required to ensure that the centre of the sample had sufficient coverage. This placed a limit on the width of substrates used at ~1 cm. At this width, a variance in silica thickness is observed across the sample but is not great enough to interfere with subsequent ZnO depositions. The volume of sol used per cm^2 was approximately 20µl for nanospheres of 1 µm diameter and would be adjusted up or down, *pro-rata*, for sphere diameters of 1.5 µm or 500 nm respectively.

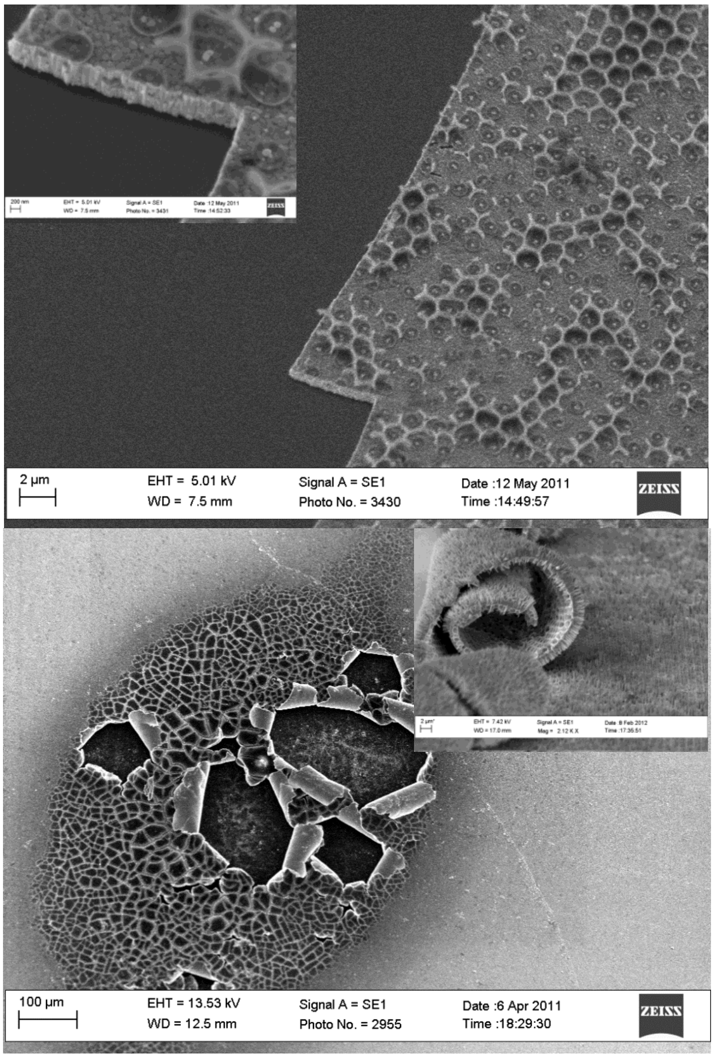

Figure 4.14: SEM image of a typical example of delamination, the ZnO buffer layer has been removed, exposing the Si/SiO$_2$ substrate (top). Bottom shows a drying spot where silica layer is too thick, inset is example of edges of such a spot peeling away.

It was observed that silica deposited in this way was generally quite uniform and importantly in the majority of cases the point of contact between the nanosphere and the underlying ZnO buffer layer was left uncoated. This allowed for subsequent

ZnO deposition at these points. However in some cases, the point of contact between sphere and the buffer layer was coated by silica. This suggested that in some places the nanosphere is in fact not making contact with the substrate underneath. This may be caused by a number of factors. Firstly it is possible that a number of nanospheres are being lifted slightly away from the substrate when the sol is being applied, allowing the sol to seep underneath. The second possibility is that the underlying buffer layer is not perfectly flat and there is space underneath the nanosphere for silica sol to seep in. For this reason it is essential that the nanospheres make good contact with the substrate. In order to ensure this contact, before the silica sol is applied to the nanosphere monolayer the substrate is heated to 110°C for 30 seconds in order to slightly deform the nanospheres, causing them to adhere to the substrate and to expand them slightly in order for those spheres not touching the substrate to make contact.

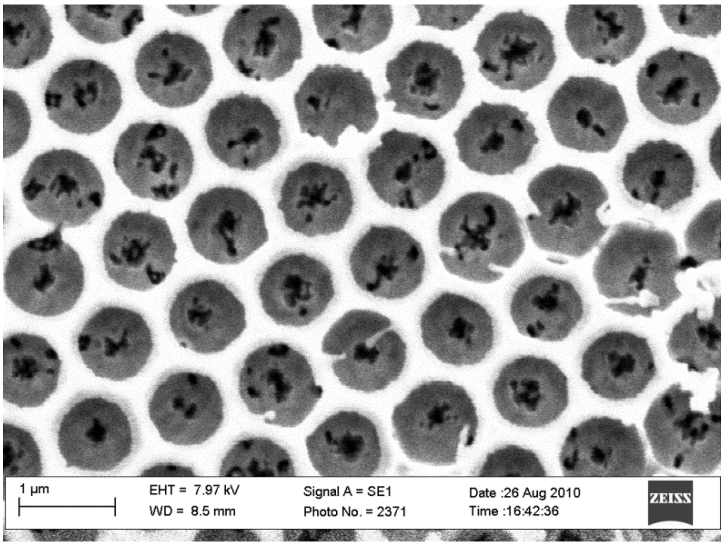

Figure 4.15: SEM image of typical silica mask, the contact points between spheres and buffer layer may be seen at the centres of the circular regions.

It was found that while using sphere diameters of 500 nm and 1 µm that the techniques outlined above were successful and produced high quality silica honeycomb masks with relatively few defects. Figure 4.15 shows an example of a 1 µm mask. However, due to the lower quality of nanosphere monolayer produced while using spheres of 1.5 µm diameter, silica mask quality was also not optimal. In general there are two types of defect seen on these samples. Firstly, within nanosphere domains, cracks in the silica mask in the region between adjacent nanospheres are observed leaving the underlying ZnO buffer layer uncoated. This occurs even in regions where nanosphere packing is of high quality. It is believed that this cracking, rarely seen on samples with smaller nanospheres, is due to the size of spheres used. Larger spheres require much more silica to fill the interstitial spaces between spheres. The higher volumes of silica deposited are much more prone to cracking than with smaller spheres. Secondly, monolayers of 1.5 µm spheres are not as densely packed as the smaller spheres due to the lack of additional surfactant to further pack the spheres during deposition. This leads to domain boundaries with slightly larger spaces between domains than would be expected. This then leads to cracks along the boundary, since the thickness of the silica layer at this point makes it particularly susceptible to defects of this nature. Figure 4.16 shows a SEM image where a number of the possible issues mentioned above may be seen, including areas where the spheres did not make contact with the buffer layer and defects at domain boundaries.

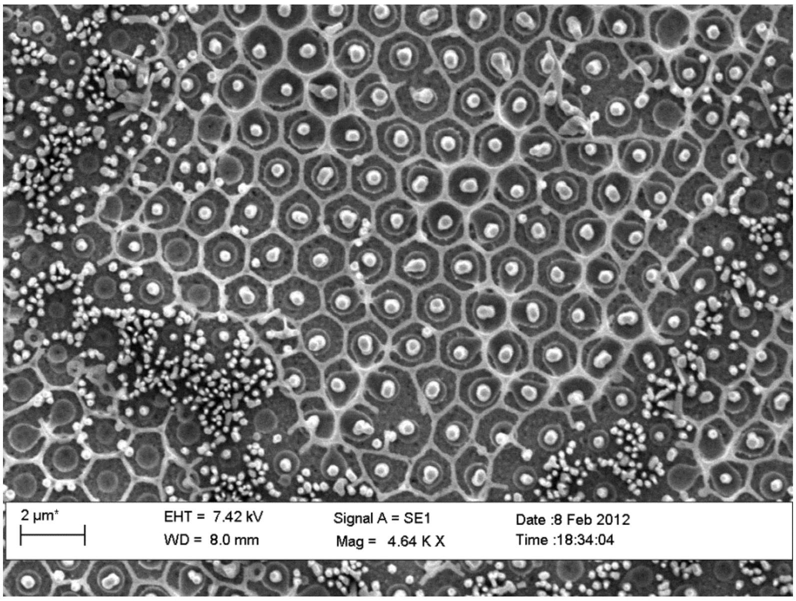

Figure 4.16: SEM image of sample patterned using 1.5 µm diameter spheres exhibiting quite small domains and cracks along domain boundaries.

4.9 ZnO deposition through silica secondary masks

Once the silica mask has been densified, the sample is ready for the deposition of ZnO nanowires. This is carried out using both the CBD and CTR-VPT techniques, both producing good results with distinctly different array morphologies.

4.9.1 Inverse nanosphere lithography CBD

In addition to CTR-VPT nanowire growths through silica honeycomb masks, CBD growths were also carried out. Growths were carried out using the Zn acetate method only, as the silica layer is etched by the solutions used in the other two methods.

Growths were carried out under the same conditions as with ZnO buffer layers. That is, an aqueous solution of Zn acetate of 5 mM concentration heated to approximately 65°C was used. Depositions were carried out under these conditions for approximately 90 minutes; it was observed that the length of the nanostructures deposited was approximately proportionate to the time spent in solution.

As shown in figures 4.17 - 19 below, this technique yields arrays of highly periodic and uniform nanostructures. In particular the height of each structure on all samples produced is very uniform and influenced solely by the deposition time. The diameter of nanowires grown is solely determined by the area left uncovered by the silica mask. Due to nanosphere annealing before the silica mask is applied to the sample, the nanosphere-substrate contact area, and the subsequent nanowire diameters tend to be relatively large. In addition to this, due to the capping nature of Zn acetate depositions, nanowires grown tend to get wider as they grow. This places a limit on the possible height of nanowires grown, since at some point the structures will coalesce and form a continuous film.

In this growth mode, any failure in the silica mask will result in the growth of a film in that region. There is no uncontrolled growth to speak of in this case, as all nanostructures grown under the same conditions have the same height.

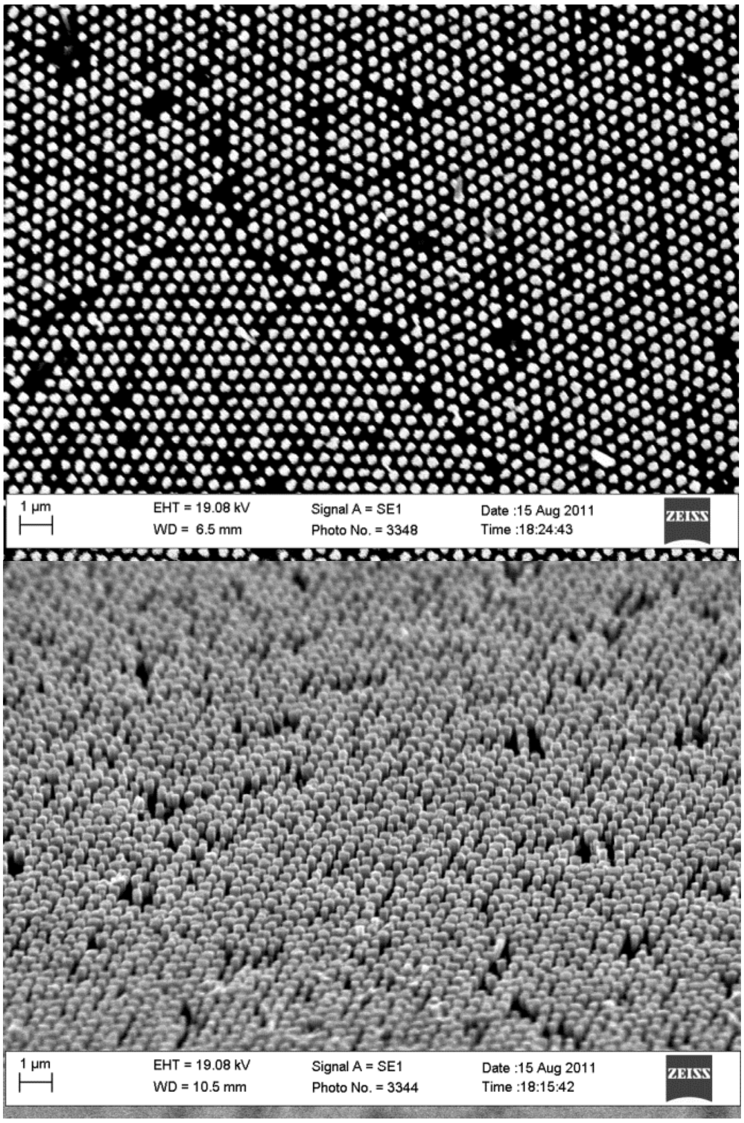

Figure 4.17: ZnO nanowires grown by CBD through silica honeycomb mask with 500 nm inter-wire spacing. Top shows view from above and bottom shows same sample at an angle of 45°.

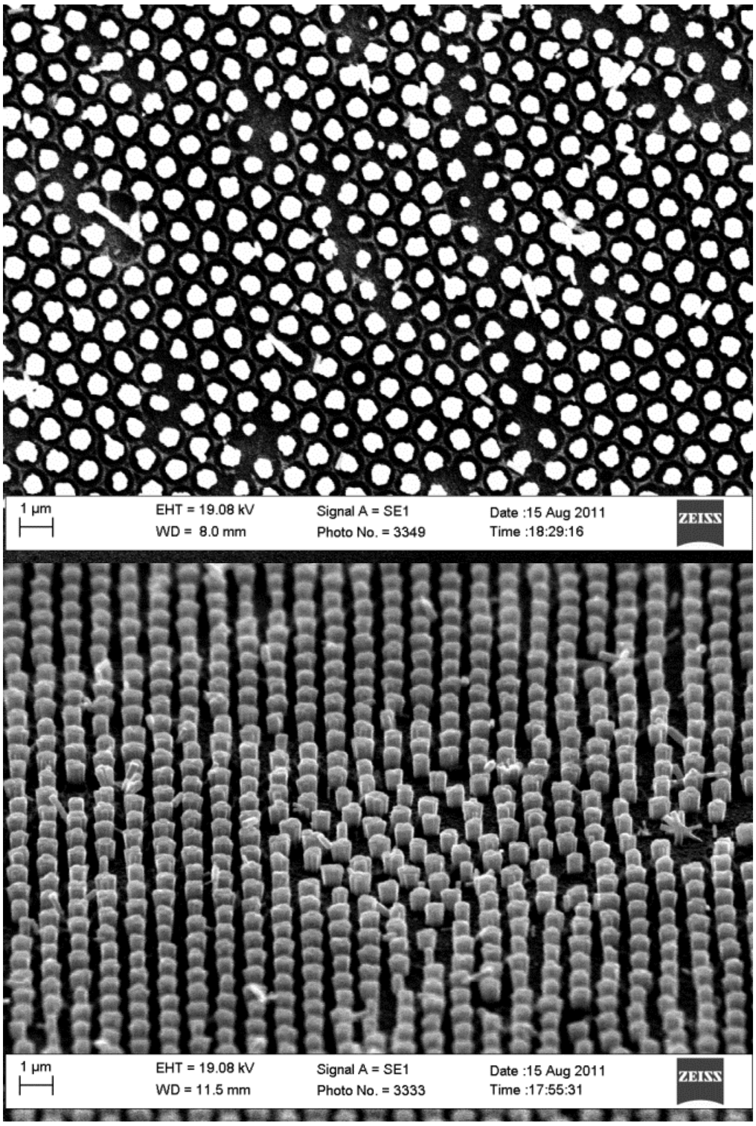

Figure 4.18: ZnO nanowires grown by CBD through silica honeycomb mask with 1 µm inter-wire spacing. Top shows view from above and bottom shows same sample at an angle of 45°.

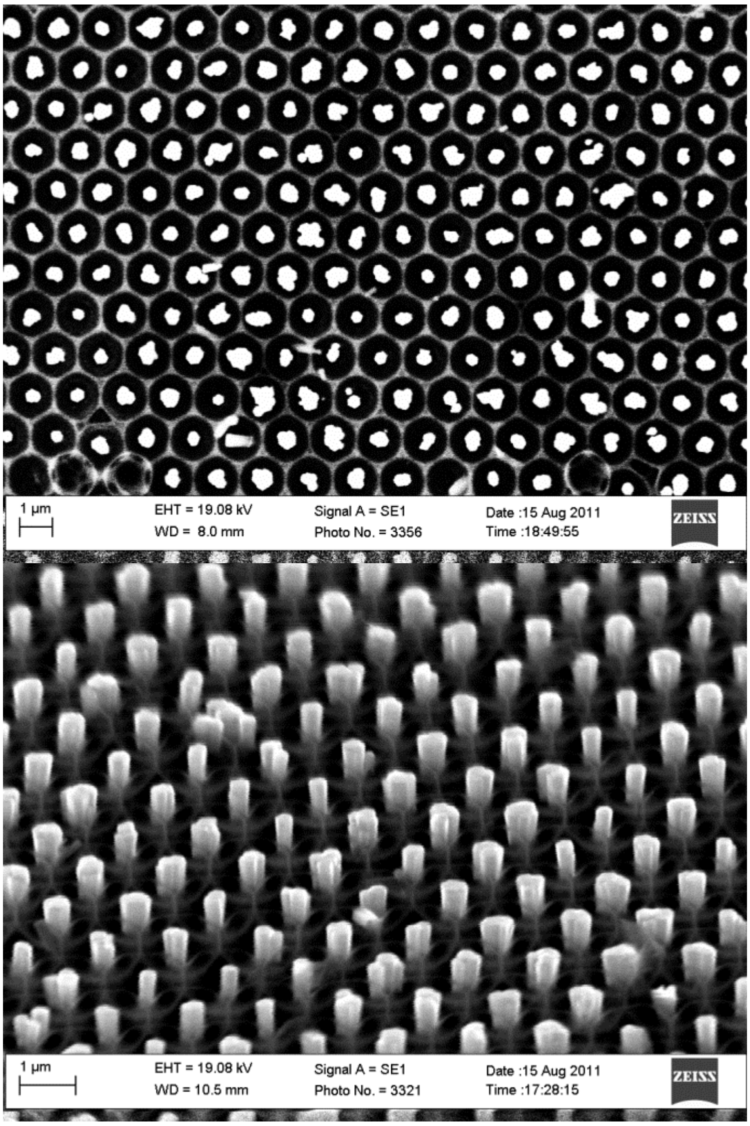

Figure 4.19: ZnO nanowires grown by CBD through silica honeycomb mask with 1.5 µm inter-wire spacing. Left shows view from above and right shows same sample at an angle of 45°.

4.9.2 Inverse nanosphere lithography CTR-VPT

Initially, once the silica template has been densified, the sample was then immediately grown upon by CTR-VPT with no intermediate CBD step. This resulted in well aligned and ordered nanowire growth for all nanosphere sizes. Differences in the morphology between samples where different nanosphere sizes were used were observed. The smaller sphere sizes generally lead to narrower and taller nanowires with the location of nanowires generally confined to the locations where nanospheres were in contact with the underlying buffer layer. However, while nanowire arrays grown in this way were generally well ordered they were not completely uniform over the sample area, with many examples of multiple nanowires nucleating from the same location and sharing the same base, an example of which is shown in figure 4.20. In many cases these multiple nucleation nanostructures have an angle of approximately 60° between them. It is thought that these are due to defects and grain boundaries within in the underlying ZnO buffer layer. These defects are unavoidable in a polycrystalline ZnO buffer layer. This morphology is not observed in unmasked CTR-VPT growths, so while their exact cause is not known it is reasonable to suggest that the presence of the silica template is contributing to their growth. It is possible that since the choice of nucleation sites in this growth mode are severely constrained by the presence of the mask, nucleation is forced to occur at points that would not otherwise be energetically favourable and would not be grown upon in a non-templated growth. In order to improve the uniformity of growth across the sample, before growth by CTR-VPT, a CBD nanorod deposition was performed on the templated substrate using zinc acetate as the source material.

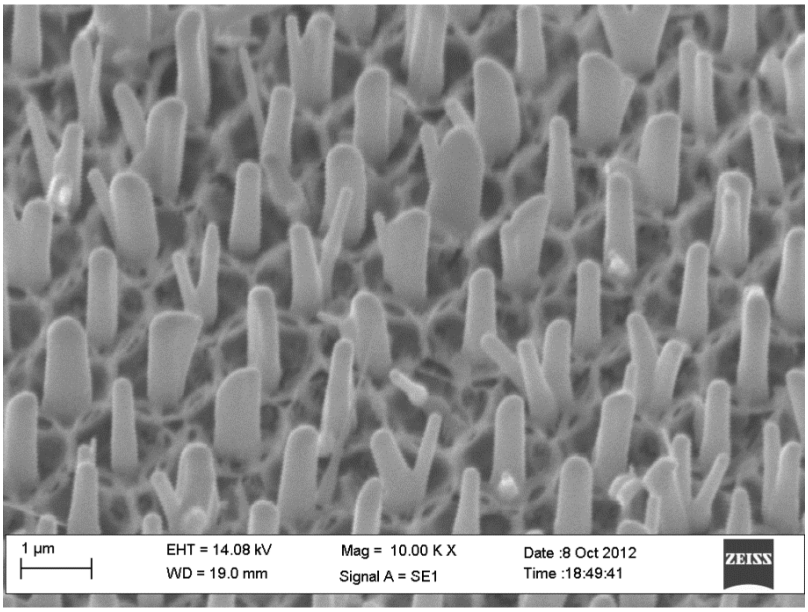

Figure 4.20: Examples of multiple structures growing from individual points.

Irrespective of the size of the nanospheres used to create the silica pattern or whether an intermediary CBD was undertaken, growths by CTR-VPT on silica patterned substrates are prone to excessive ZnO growth in a manner similar to that observed in the metal catalyst assisted growths. In this case the overgrowth issue is due to the fact that while initially growth is limited to areas uncovered by the silica mask, once nanowire growth begins, further possible nucleation sites are created, leading to further deposition until the Zn vapour is depleted. This process generally results in very long nanowires (many tens of microns). These long nanowires, while being vertically aligned at their bases are too tall to stand vertically and in most cases lean randomly to one side such that the initial nanosphere pattern is entirely obscured, as shown in figure 4.21.

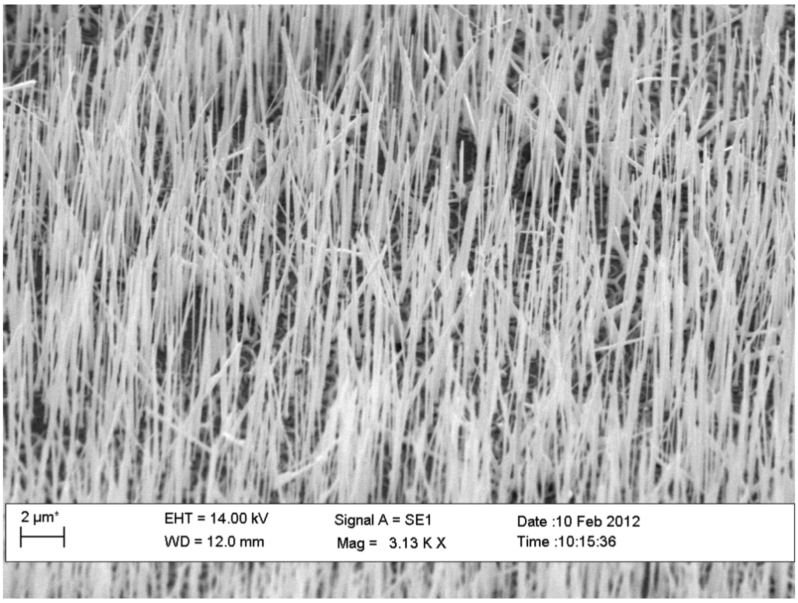

Figure 4.21: Example of nanowire overgrowth almost entirely obscuring underlying silica patterning.

In order to alleviate this issue, two methods were investigated. Firstly to reduce the quantity of Zn vapour present in the furnace less source material was used. 60 mg of each source powder is the quantity used in conventional growths but this was reduced down to 10 mg while still observing ZnO deposition. Reducing the amount of source materials used did prevent the issue of overgrowth with large areas of successful ordered growth being achieved. However, this was not uniform over the entire sample area with nanowire morphologies not seen in other growth modes observed in some areas. As seen in figure 4.22 the conventional nanowire morphology is replaced by a teardrop shaped nanostructure in this case. This was observed in all cases where the amount of source powders used was greatly reduced. This morphology is likely due to an initial high Zn supersaturation due to a temperature overshoot in the furnace which is then quickly depleted by deposition. As shown by R T Rajendra Kumar *et al*. [2], as vapour saturation reduces, a 1D growth mode is favoured; in their case since vapour saturation reduces to a constant level nanowires of constant diameter are grown. In the case of the teardrop shaped structures produced in this work it is clear that Zn vapour does not reduce to some constant level but is instead completely removed after some time during growth.

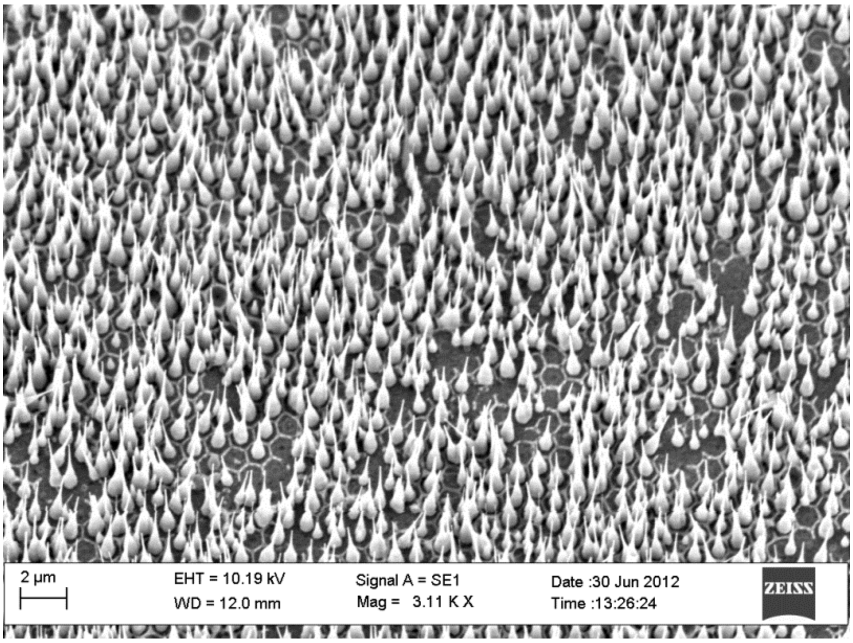

Figure 4.22: SEM image of teardrop shaped nanostructures. This morphology is generally observed when small amounts of CTR-VPT precursor material are used.

The second technique investigated was to change the temperature regime in which growths are carried out; in this case the normal 60 mg of each source powder was used in all growths. In typical CTR-VPT depositions the temperature set-point is set at the start of the growth and not altered until the growth time has elapsed.

However in order to reduce the occurrence of temperature overshoot and consequent overgrowth as mentioned above, the temperature was ramped slowly to the desired growth temperature. The rationale for this course of action is that since the furnace tends to overshoot the temperature set-point by approximately 100°C before slowly cooling to the set-point (as outlined in Chapter 3), it is possible that a large amount of subsequent ZnO deposition occurs while the temperature is considerably higher than the set-point. This hypothesis is supported by the observation of nanowires with wide bases on non-patterned CTR-VPT samples. In the case of nanowires grown through a silica mask, the diameter is limited by the area of underlying ZnO left exposed. Due to this limitation in diameter, deposition occurs mostly in the c-axis and given the high Zn saturation during this time, leading to very long nanowires. The temperature regime that yielded the best results, over all nanosphere sizes was achieved by setting the initial temperature set-point to 800°C, then after 10 minutes, increasing this by a rate of 10°C per minute until 900°C is reached. After 40 minutes at this temperature the furnace is slowly cooled to room temperature. The temperature is initially held for 10 minutes as this is approximately the amount of time taken for the measured furnace temperature to reach the set-point. Figure 4.23 shows the furnace temperature with respect to time along with the temperature profile of when no ramp rate is used. In both cases the desired temperature is 900°C, and the data shows that the initial temperature peak is reduced by approximately 50°C, while also showing that after approximately 20 minutes the temperature is the same in each case. This made a significant difference in nanowires produced. Overly long nanowires are not observed on samples produced in this way and since the full 60 mg of source materials are used the nanowires are not subject to the tapering as seen in the case where less powder is used. Examples of nanowires produced in this way are shown in figures 4.24 - 26, in general they are extremely uniform over the sample area and are readily reproducible during growth on nanosphere templated substrates, over all nanosphere sizes.

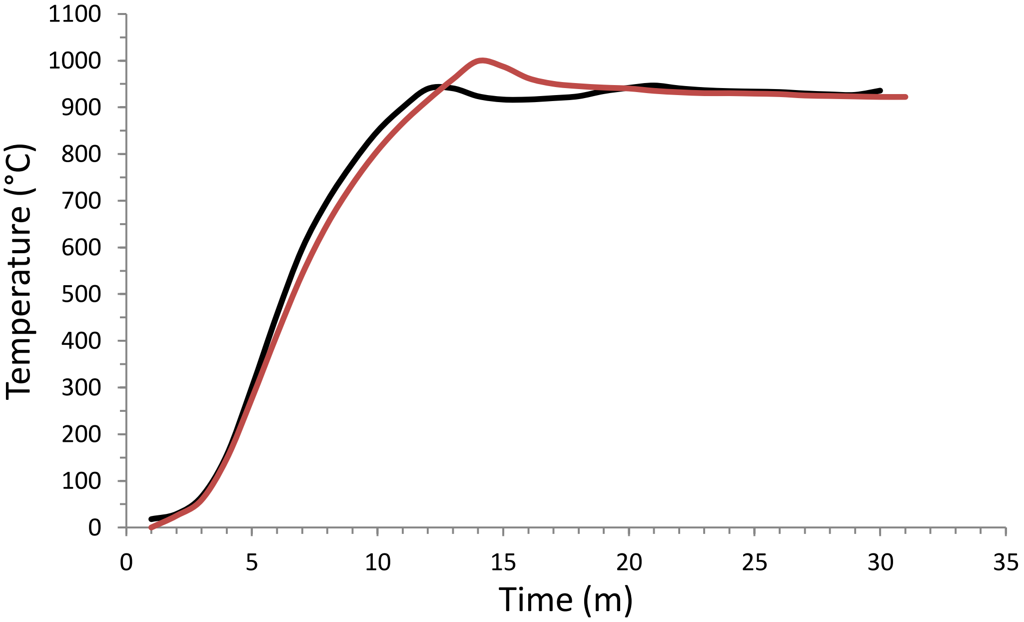

Figure 4.23: Graph of measured furnace temperature vs. time for ramped temperature regime in black and non-ramped in red. The initial temperature spike is lowered by 50°C in the ramped regime, but temperatures converge at ~20 minutes.

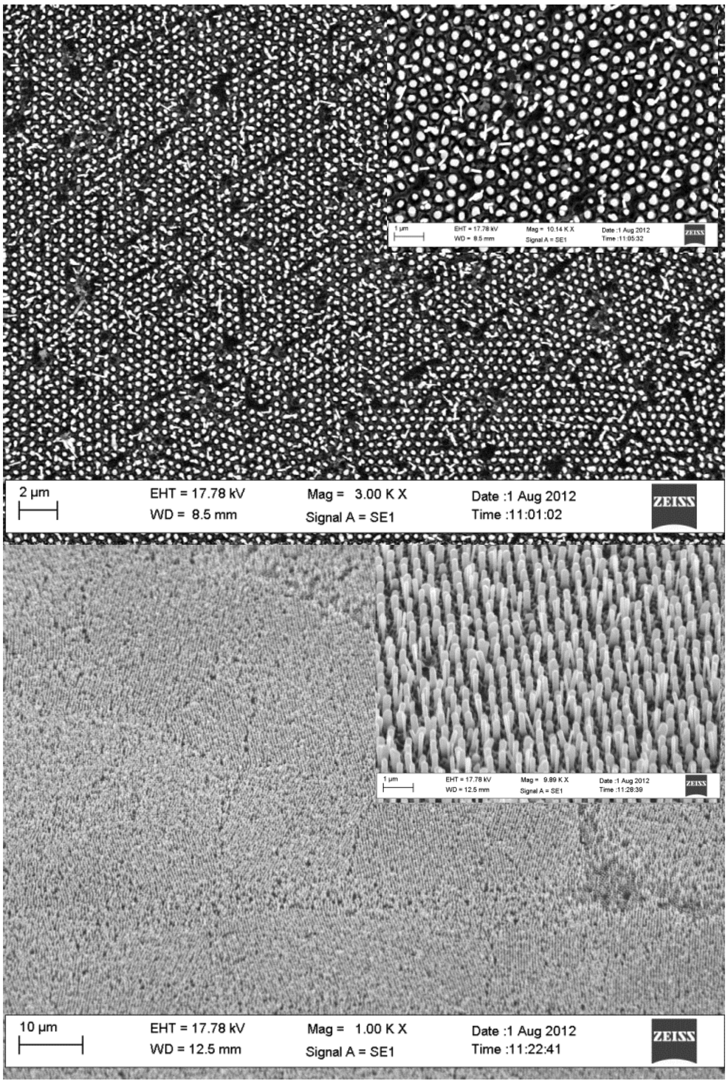

Figure 4.24: ZnO nanowire array grown through silica mask by CTR-VPT with 500 nm inter-wire spacing. Top shows array from above with inset image showing higher magnification. Bottom shows array from angle of 45° with higher magnification image inset.

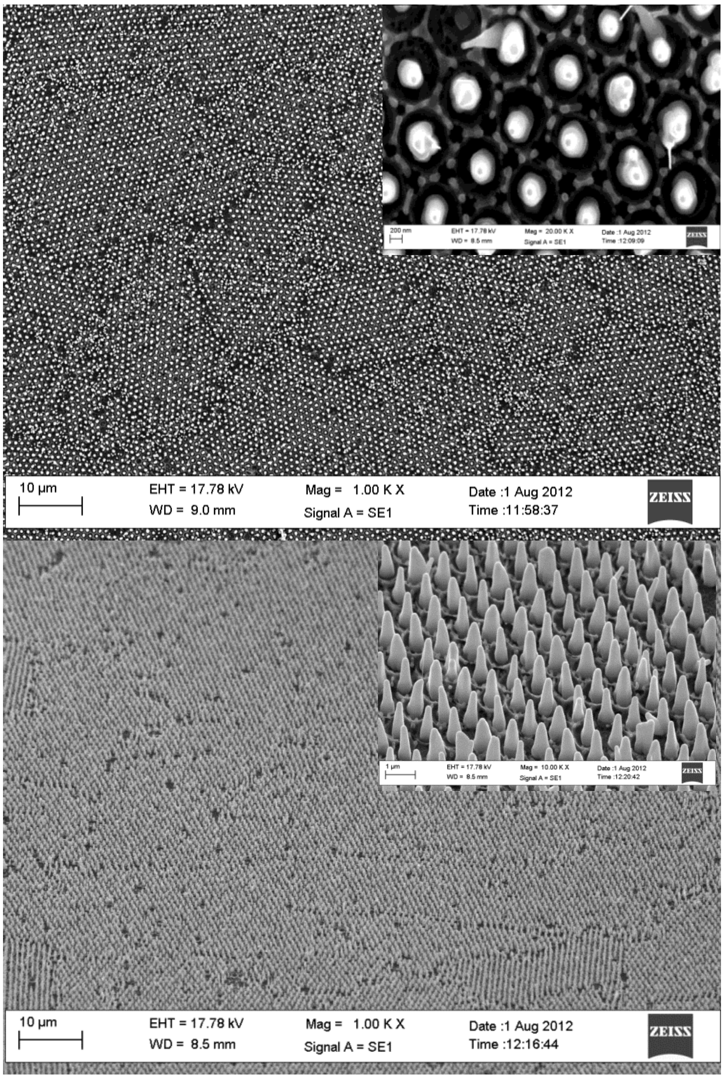

Figure 4.25: ZnO nanowire array grown through silica mask by CTR-VPT with 1 µm inter-wire spacing. Top shows array from above with inset image showing higher magnification. Bottom shows array from angle of 45° with higher magnification image inset.

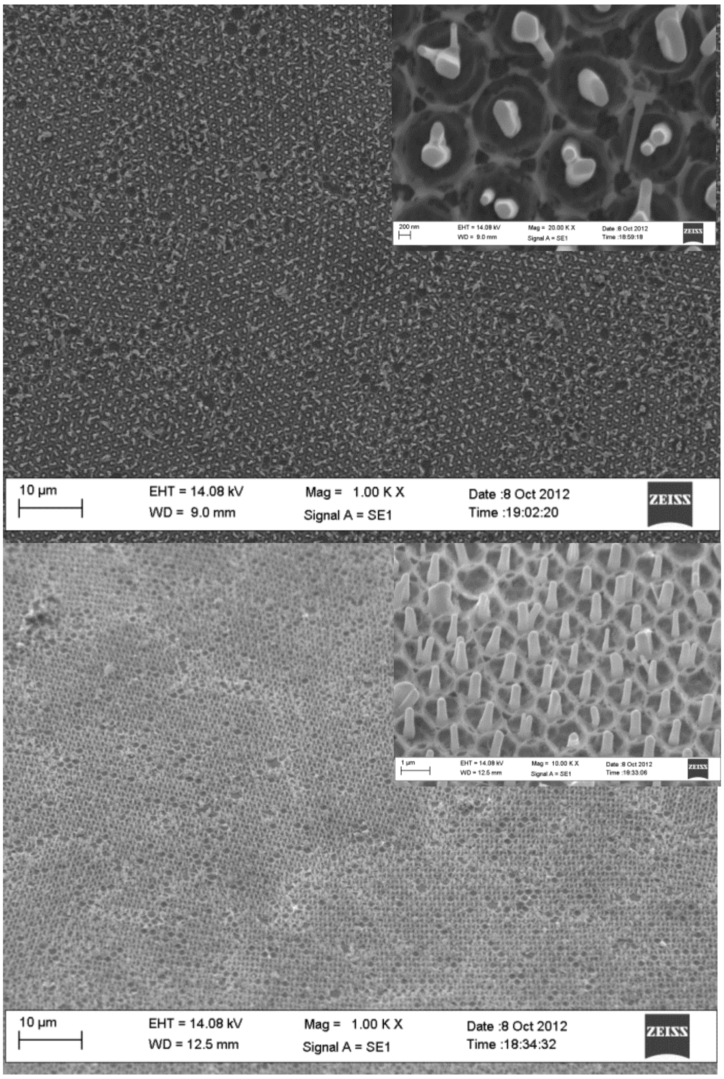

Figure 4.26: ZnO nanowire array grown through silica mask by CTR-VPT with 1.5 µm inter-wire spacing. Top shows array from above with inset image showing higher magnification. Bottom shows array from angle of 45° with higher magnification image inset.

4.10 Conclusions

In this chapter we have examined the use of nanosphere lithography for the deposition of spatially ordered ZnO nanowire arrays. This was carried out successfully using two distinct techniques. Firstly it was found that by depositing a metal catalyst material through the apertures of a hexagonally close packed nanosphere layer it is possible to create an array of metallic islands on the substrate which may then be used to initiate CTR-VPT deposition to form a well ordered nanowire array. It was found that spatial ordering could be achieved on substrates pre-coated with a ZnO buffer layer, however it was not possible to implement this technique on uncoated Si/SiO_2 substrates.

The second technique investigated was that developed by Byrne *et al.*, where a HCP nanosphere layer was used as a template to deposit a secondary mask. The material used was silica, and the interstitial spaces in the nanosphere array were filled with this material by drop coating a silica sol through the layer. Removing the sphere layer revealed a silica honeycomb pattern underneath. The honeycomb pattern was then used as a template for nanowire depositions, both by CBD and CTR-VPT techniques. Nanowire arrays with inter-wire spacings of 500 nm, 1 µm, and 1.5 µm were grown in this way.

In the next chapter, the field emission properties of these samples will be discussed, particularly with respect to inter-wire spacing and growth methods.

4.11 References

1. Liu, D.F., et al., *Periodic ZnO nanorod arrays defined by polystyrene microsphere self-assembled monolayers.* Nano Letters, 2006. **6**(10): p. 2375-2378.

2. Rajendra Kumar, R.T., et al., *Control of ZnO nanorod array density by Zn supersaturation variation and effects on field emission.* Nanotechnology, 2007. **18**(21).

3. Garry, S., et al., *Control of ZnO nanowire arrays by nanosphere lithography (NSL) on laser-produced ZnO substrates.* Applied Surface Science, 2011. **257**(12): p. 5159-5162.

4. Kannan, B., K. Castelino, and A. Majumdar, *Design of Nanostructured Heterojunction Polymer Photovoltaic Devices.* Nano Letters, 2003. **3**(12): p. 1729-1733.

5. Tsung-Yen, T., et al., *The fabrication of a carbon nanotube array using a catalyst-poisoning layer in the inverse nano-sphere lithography method.* Nanotechnology, 2009. **20**(30): p. 305303.

6. Liu, D.F., et al., *A simple route to scalable fabrication of perfectly ordered ZnO nanorod arrays.* Nanotechnology, 2007. **18**(40): p. 405303.

7. Zhang, X., et al., *Synthesis of large-scale periodic ZnO nanorod arrays and its blue-shift of UV luminescence.* Journal of Materials Chemistry, 2009. **19**(7): p. 962-969.

8. Fan, H.J., et al., *Well-ordered ZnO nanowire arrays on GaN substrate fabricated via nanosphere lithography.* Journal of Crystal Growth, 2006. **287**(1): p. 34-38.

9. Cheng, C., et al., *High-Quality ZnO Nanowire Arrays Directly Fabricated from Photoresists.* ACS Nano, 2008. **3**(1): p. 53-58.

10. Kim, T.-U., et al., *Creation of Nanoscale Two-Dimensional Patterns of ZnO Nanorods using Laser Interference Lithography Followed by Hydrothermal Synthesis at 90 °C.* Crystal Growth & Design, 2010. **10**(10): p. 4256-4261.

11. Wei, Y., et al., *Wafer-Scale High-Throughput Ordered Growth of Vertically Aligned ZnO Nanowire Arrays.* Nano Letters, 2010. **10**(9): p. 3414-3419.

12. Zhao, Q., et al., *Morphological effects on the field emission of ZnO nanorod arrays.* Applied Physics Letters, 2005. **86**(20): p. 203115.

13. Yu, C.-W., et al., *Patterned Fabrication of Single ZnO Nanorods and Measurement of Their Optoelectrical Characteristics.* Journal of Nanoscience and Nanotechnology, 2008. **8**(9): p. 4377-4381.

14. Zhou, H., et al., *Ordered n-type ZnO nanorod arrays.* Applied Physics Letters, 2008. **92**(13): p. 132112-3.

15. Zhong Lin, W., *Zinc oxide nanostructures: growth, properties and applications.* Journal of Physics: Condensed Matter, 2004. **16**(25): p. R829.

16. Rybczynski, J., et al., *Formation of super arrays of periodic nanoparticles and aligned ZnO nanorods - Simulation and experiments.* Nano Letters, 2004. **4**(10): p. 2037-2040.

17. Kosiorek, A., et al., *Shadow Nanosphere Lithography: Simulation and Experiment.* Nano Letters, 2004. **4**(7): p. 1359-1363.

18. Kosiorek, A., et al., *Fabrication of Nanoscale Rings, Dots, and Rods by Combining Shadow Nanosphere Lithography and Annealed Polystyrene Nanosphere Masks.* Small, 2005. **1**(4): p. 439-444.

19. Burmeister, F., et al., *Colloid Monolayers as Versatile Lithographic Masks.* Langmuir, 1997. **13**(11): p. 2983-2987.

20. Fu, Y., et al., *Preparation of ordered porous SnO2 films by dip-drawing method with PS colloid crystal templates.* Journal of the European Ceramic Society, 2007. **27**(5): p. 2223-2228.

21. Ogi, T., et al., *Fabrication of a large area monolayer of silica particles on a sapphire substrate by a spin coating method.* Colloids and Surfaces A: Physicochemical and Engineering Aspects, 2007. **297**(1–3): p. 71-78.

22. Rybczynski, J., U. Ebels, and M. Giersig, *Large-scale, 2D arrays of magnetic nanoparticles.* Colloids and Surfaces A: Physicochemical and Engineering Aspects, 2003. **219**(1–3): p. 1-6.

23. Hsu, C.-M., et al., *Wafer-scale silicon nanopillars and nanocones by Langmuir--Blodgett assembly and etching.* Applied Physics Letters, 2008. **93**(13): p. 133109-3.

24. Haynes, C.L., et al., *Angle-resolved nanosphere lithography: Manipulation of nanoparticle size, shape, and interparticle spacing.* Journal of Physical Chemistry B, 2002. **106**(8): p. 1898-1902.

25. Byrne, D., et al., *A catalyst-free and facile route to periodically ordered and c-axis aligned ZnO nanorod arrays on diverse substrates.* Nanoscale, 2011. **3**(4): p. 1675-1682.

26. Li, C., et al., *Field electron emission improvement of ZnO nanorod arrays after Ar plasma treatment.* Applied Surface Science, 2007. **253**(20): p. 8478-8482.

Chapter 5: Field Emission

5.1 Introduction

This chapter describes the characterisation by field emission (FE) of samples produced using the methods described in chapters 2 to 4. FE is measured from ZnO nanowire arrays grown both by CTR-VPT and CBD. FE from spatially ordered ZnO nanowire arrays produced using NSL is also studied to enable insight into how array density impacts emission uniformity; it will be shown that nanowire array morphology and uniformity have a large effect on FE performance.

In some cases FE is a destructive characterisation technique; it is observed for many samples that nanowires may melt slightly but in some case there are more extreme surface disruptions. These disruptions negatively and permanently impact the quality of the nanowire array as emitters. The nature of these disruptions will be discussed and possible array morphologies that may avoid their occurrence will be suggested.

By examining *I*-*V* data from the various samples studied, and considering similarities between samples which have been damaged during characterisation, it is possible to prescribe array morphologies which will be less liable to damage and which will maximise FE emission currents, making ZnO nanowire arrays a more attractive materials option for the various technological application areas of field emission.

5.2 Electron emission

Electron emission is the process by which electrons near the top of the conduction band of a metal or semiconductor escape from the surface. For this to occur, an electron must either undergo thermal excitation or tunnelling.

5.2.1 Thermionic emission

Energy may be transferred from vibrations in the crystal lattice structure to electrons. If the energy transferred to the electrons is greater than the work function of the material then thermionic election emission may occur.

At zero Kelvin the electron distribution may be represented by a step function, since the probability of finding an electron at an energy level above the Fermi energy is zero, while the probability for an electron to occupy a state below the Fermi energy is unity. At temperatures above zero Kelvin, electrons can be excited to states with higher energies than the Fermi level. The probability that a particular energy level is occupied by an electron is given by:

$$f(E) = \frac{1}{exp\left(\frac{-\phi}{k_B T}\right)+1} \tag{5.1}$$

Where μ is the Fermi level, E is the energy of the state in question, k_B is Boltzmann's constant and T is the temperature. Assuming that $(E - \mu)$ stays constant it can be seen that the probability of an electron occupying a particular state increases with temperature and with it the probability of thermionic electron emission also increases.

In 1913 it was first reported that cold discharges, electron emission at temperatures below which significant thermionic emission takes place, could be made to pass through evacuated tubes [1]. The current density of these discharges was later described using the following equation [2]:

$$J = \lambda_R \left[\frac{4\pi m k_B^2 e}{h^3}\right] T^2 exp\left(\frac{-\phi}{k_B T}\right) \tag{5.2}$$

Where J is the current density (A/m^2), λ_R is a material specific correction factor, m is the mass of an electron (kg) and e is its charge (C). Φ is the work function of the material, h is Planck's constant (m^2 kg s^{-1}) and k_B is the Boltzmann constant (m^2 kg s^{-2}).

This was further developed with a publication in 1928 by Lothar W. Nordheim which replaced λ_R with a term (1 – D), where D is the emission coefficient, which is the proportion of the electrons reaching the emitter surface that overcome the barrier [3]. This results in the emitted current density being described by the following equation:

$$J = (1 - D)\left[\frac{4\pi m k_B^2 e}{h^3}\right] T^2 exp\left(\frac{-\phi}{k_B T}\right) \tag{5.3}$$

In the presence of a strong electric field the emission process becomes more complicated. The effect of the applied electric field is to lower the work function of the material, as illustrated in figure 5.1, and thermionic emission over the reduced barrier is known as Schottky emission [4]. The increased emission due to this influence can be described by replacing the (ϕ) term in the equation above with (ϕ - $\Delta\phi$), where $\Delta\phi = \phi - V_{max}$, where V_{max} is the Schottky lowering potential energy given by $\left(\frac{e^3 F}{4\pi\varepsilon_o}\right)^{1/2}$,where F is the applied field (V m^{-1}).

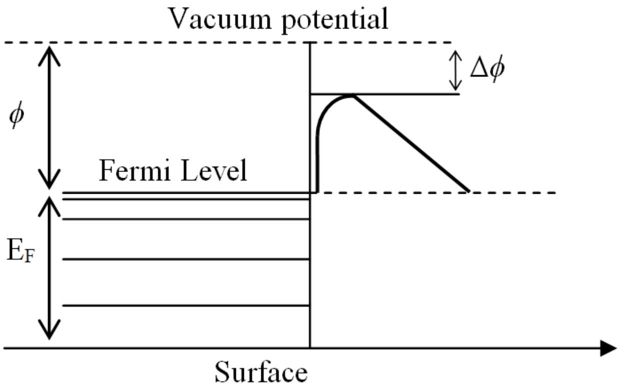

Figure 5.1: Lowering of work function due to applied electric field.

This description of current density holds for electric fields lower than ~ 10^8 V/m. For electric field strengths above this Fowler-Nordheim quantum tunnelling becomes the dominant source of electron emission.

5.2.2 Fowler-Nordheim tunnelling

In field emission, electrons do not gain enough energy to exceed the work function. Instead electrons are emitted by tunnelling through the potential barrier at the material surface. As shown in figure 1.5, the potential barrier is deformed into a triangular shape, to such an extent that it is possible for electrons to tunnel through. Figure 1.5 also shows that the potential barrier at the material surface is not a sharp step but is rounded by the presence of a positive image charge inside the material. This potential is given by,$-e^2/16\pi\varepsilon_o x$ [5]. Field emission was first described mathematically by Ralph H. Fowler and Lothar W. Nordheim in 1928 [6]. The derivation of the Fowler-Nordheim equation makes a number of assumptions: (i) the temperature of the metal is 0 K; (ii) the electrons in the material follow the free-electron approximation; (iii) the surface is smooth and planar; (iv) the potential barrier consists of both the image force and the applied electric field. According to the Fowler-Nordheim model, electrons at the surface of a conductor obey Fermi-Dirac statistics and penetrate the barrier with a probability determined by a solution of the Schrodinger equation [7]. The following derivation is presented in cgs units, as these were the units used in the original, and much of the subsequent work. The final equations are converted to SI units, and SI units were used in all the analysis.

As shown schematically in figure 1.5, the potential at a distance x from a material surface under an electric field F is given by [8]:

$$V(x) = -\frac{e^2}{4x} - Fex \tag{5.4}$$

And the total energy of an electron subject to this energy potential *V(x)* is given by:

$$\varepsilon = \frac{P_x^2}{2m} + \frac{P_y^2}{2m} + \frac{P_z^2}{2m} + V(x) \tag{5.5}$$

It is assumed that only the x component of momentum contributes to the probability of an electron penetrating the barrier. The x part of the energy is defined by the following [7]:

$$U = \varepsilon - \frac{P_y^2}{2m} + \frac{P_z^2}{2m}$$

$$= \frac{P_x^2}{2m} + V(x) \tag{5.6}$$

A supply function *N(U)dU* is defined as the number of electrons incident on the surface with energies in the range U to $U + dU$ per unit area and time. The probability of an electron penetrating the barrier is defined as *D(U)*. The product of these two functions gives the number of electrons tunnelling from the metal into the vacuum:

$$P(U) = N(U)D(U)dU \tag{5.7}$$

The current density is then given by:

$$J = \int_{-\infty}^{\infty} P(U)dU \tag{5.8}$$

The supply function is derived from the Fermi-Dirac energy distribution [6]:

$$N(U)dU = \frac{4\pi m_e kT}{h^3} \ln\left(1 + exp\left[-\frac{U-\phi}{k_B T}\right]\right) dU \tag{5.9}$$

Where k is Boltzmann's constant, T is the temperature, m_e is mass of the electron, ϕ is the work function, and h is Planck's constant.

For temperatures of $[(U - \phi) / k_B T] \gg 1$ and $U \ll \phi$:

$$kT \ln\left[1 + exp\left[-\frac{U-\phi}{k_B T}\right]\right] = \phi - U \tag{5.10}$$

The barrier penetration probability is calculated with a WKB approximation [9] using *V(x)* from eqn. 5.4 as the potential energy:

$$D(U) = exp\left[-c + \frac{U-\phi}{d}\right] \tag{5.11}$$

Where

$$c = \frac{4\left(2m_e\phi^3\right)^{\frac{1}{2}}}{3\hbar eE}v(y), \tag{5.12}$$

$$d = \frac{\hbar eE}{2(2m_e\phi)^{\frac{1}{2}}t(y)}, \tag{5.13}$$

$$t(y) = v(y) - \frac{2}{3}y\left[\frac{dv(y)}{dy}\right], \tag{5.14}$$

$$v(y) = 2^{-1/2}[1 + (1 - y)^{1/2}]^{1/2}\left[E(k^2) - \left(1 - (1 - y)^{\frac{1}{2}}\right)K(k^2)\right], \tag{5.15}$$

$$k^2 = \frac{2(1-y^2)^{1/2}}{1+(1-y^2)^{1/2}}, \tag{5.16}$$

$$y = \frac{(e^3E)^{1/2}}{\phi} \tag{5.17}$$

Substituting equations 5.9 and 5.11 into equation 5.7 gives:

$$P(U)dU = \frac{4\pi m_e kT}{h^3}exp\left[-c + \frac{U-\phi}{d}\right]dU \tag{5.18}$$

Inserting this into equation 5.8 and integrating over all U gives:

$$J = \frac{e^2E^2}{8\pi h\phi(t(y))^2}exp\left[-\frac{4(2m_e)^{\frac{1}{2}}\phi^{\frac{3}{2}}}{3\hbar eE}v(y)\right] \tag{5.19}$$

Finally, converting the equation to SI units, expressing J in Am^{-2}, E in Vm^{-1}, and Φ in eV, and applying the relevant constants, a final equation is obtained:

$$J = 1.54 \times 10^{-6}\frac{E^2}{\phi(t(y))^2}exp\left[-6.83 \times 10^9\frac{\phi^{\frac{3}{2}}}{E}v(y)\right] \tag{5.20}$$

This equation describes the current density from a flat emission surface and assumes the local field is the same as the applied macroscopic field. To take into account for the fact that local field may vary from the macroscopic value due to features such as sharp emission tips, a geometric factor, β, was introduced which is determined by the local and large-scale geometries of the sample.

Rewriting this in terms of current I, and including the geometric factor $\beta = F_S/V$ (m^{-1}), where F_S is the field strength at the surface, and assuming an area of A, gives:

$$I = 1.54 \times 10^{-6} \frac{\beta^2 V^2 A}{\phi(t(y))^2} exp\left[-6.83 \times 10^{9} \frac{\phi^{\frac{3}{2}}}{\beta V} v(y)\right] \; in\ A \qquad (5.21)$$

The data taken during FE experiments is analysed by plotting a Fowler-Nordheim plot, which is done by plotting $\log_{10}(I/V^2)$ vs $1/V$. This plot will be linear when field emission is the dominant process. Its slope is given by:

$$m = -2.97 \times 10^{7} \frac{\phi^{\frac{3}{2}}}{2.3\beta} s(y) \qquad (5.22)$$

where $s(y)$ is a function of the variable y in eqn. (5.17) which may be approximated by:

$$s = 1 - \left(\frac{1}{6}\right) y^2 \qquad (5.23)$$

Finding the slope of the Fowler-Nordheim (FN) plot allows the geometric factor β to be calculated. From this, a dimensionless quantity γ may be calculated by $\gamma = \beta \times d$, where d is the anode/sample separation (m). This quantity is known as the field enhancement factor and takes into account both the morphology of the nanowire array and the distance between the sample and anode and is used as an indicator of FE performance, with higher values of γ being preferable.

5.3 Field emission results

In this work (FE) *I-V* data is gathered from ZnO nanowire arrays produced using both the CBD and CTR-VPT growth techniques as outlined in chapters 2 to 4. In total, FE data from ten ZnO nanowire samples are presented here, seven of which are CTR-VPT deposited nanowires while the remaining three are CBD deposited nanowires. Table 5.1 lists the samples examined in order of their production. The CTR-VPT(1) sample set does not contain a 1.5 μm spaced sample as this set was produced prior to the successful implementation of the 1.5 μm NSL technique. The CBD sample set does not contain an unspaced sample as in Zn acetate derived CBD growth this would result in the deposition of a film. CBD data will be presented first, followed by data from CTR-VPT(1) and CTR-VPT(2) sample sets.

These data are analysed by plotting both *I-V* curves and FN plots, allowing the geometric factor β and the turn on voltage, i.e. the voltage at which FE is the dominant emission type, given by the voltage at which the FN plot becomes linear, to be calculated. In subsequent FN plots only the linear portion is shown. An example of an FN plot covering the full voltage range is seen in figure 5.2, this shows the linear part where FE is occurring and the logarithmic part corresponding to low voltages before FE begins. In all cases the detailed calculation of these quantities was carried out in conjunction with Mr. Éanna McCarthy using techniques developed by him and described in McCarthy *et al.* [10]. The following section gives SEM images of each sample before examination by FE and the corresponding *I-V* and FN plots.

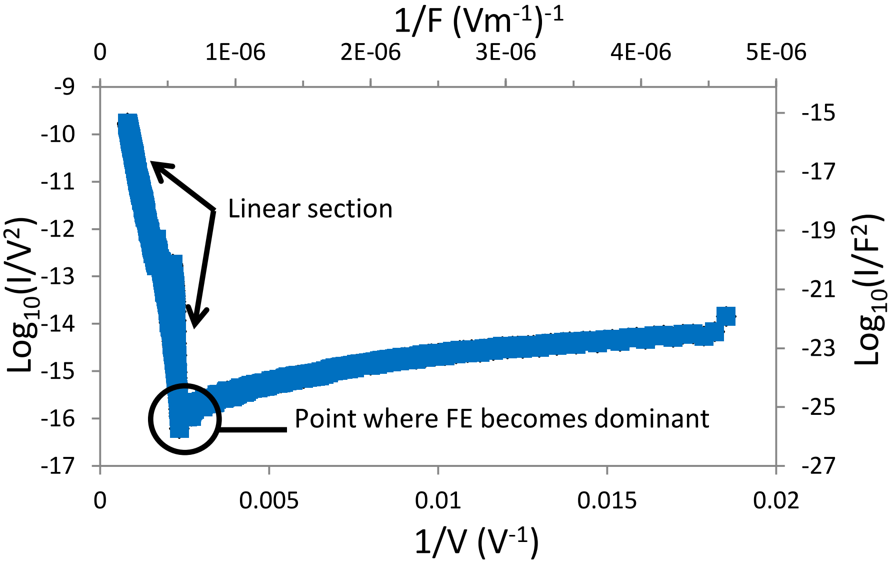

Figure 5.2: Example FN plot over full voltage range taken from CTR-VPT(1) 1.0 μm sample. Linear section corresponds to FE while the logarithmic section corresponds to voltages where FE is not occurring. The voltage at which the graph changes to linear is taken as the turn on voltage (489 V).

5.3.1 Samples examined by FE

Sample Type	Inter-wire spacing
CTR-VPT(1)	Unspaced, 500 nm, 1.0 μm
CBD	500 nm, 1.0 μm, 1.5 μm
CTR-VPT(2)	Unspaced, 500 nm, 1.0 μm, 1.5 μm

Table 5.1: Sample types and associated inter-wire spacing for samples to be examined by FE.

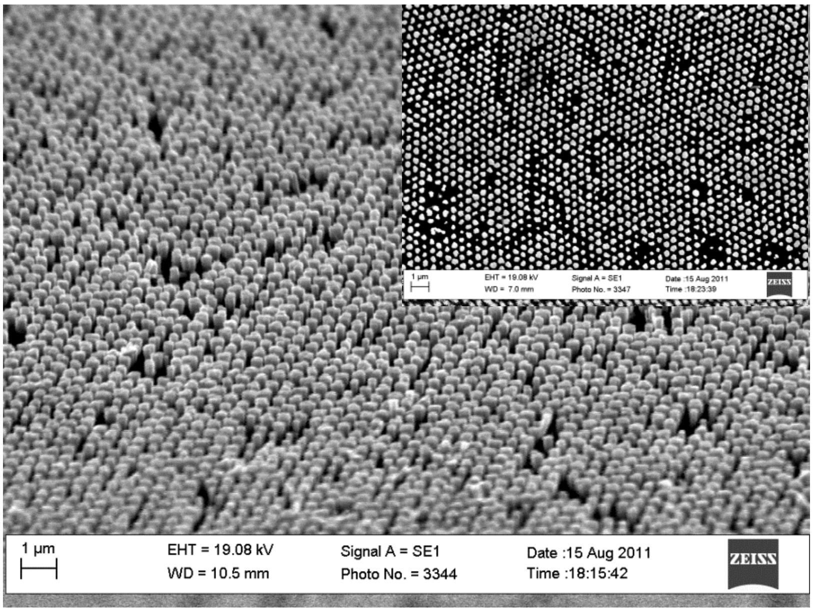

Figure 5.3: SEM image of CBD nanowire array with 500 nm inter-wire spacing. Inset shows same sample from above.

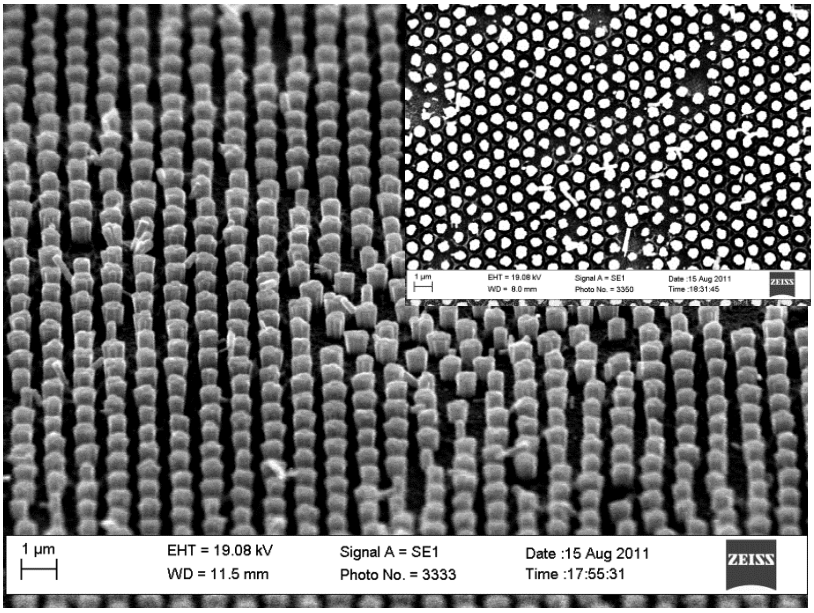

Figure 5.4: SEM image of CBD nanowire array with 1.0 µm inter-wire spacing. Inset shows same sample from above.

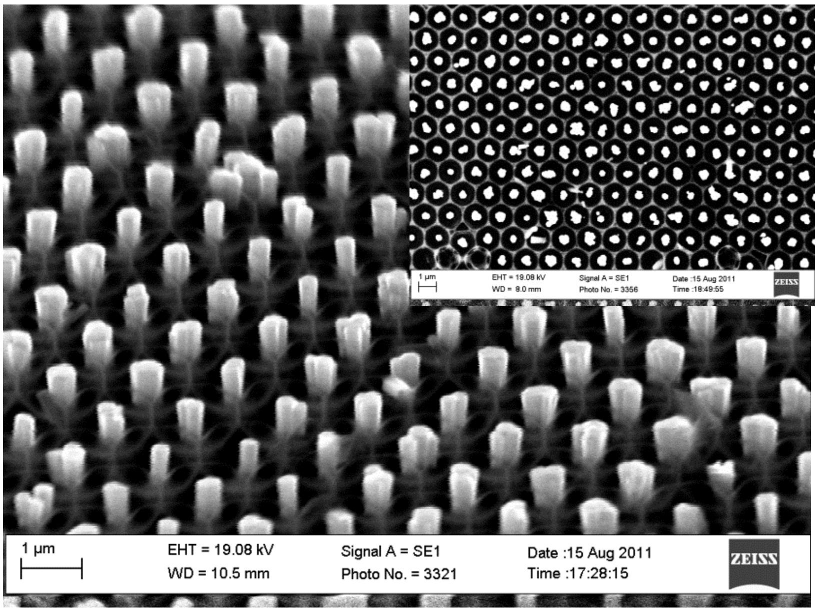

Figure 5.5: SEM image of CBD nanowire array with 1.5 µm inter-wire spacing. Inset shows same sample from above.

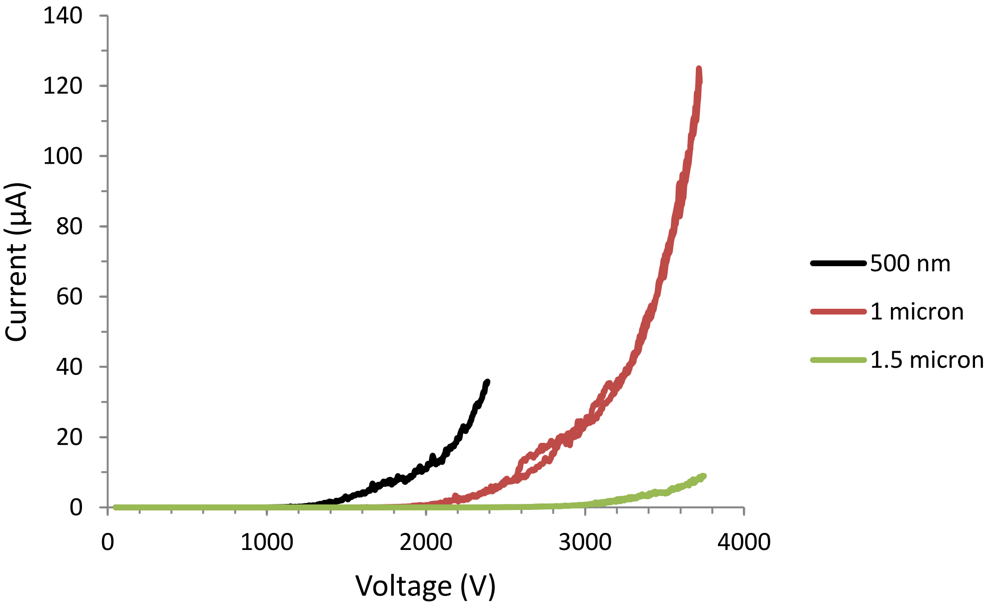

Figure 5.6: *I*-*V* curves for samples in CBD sample set, as shown in figures 5.3 – 5.5.

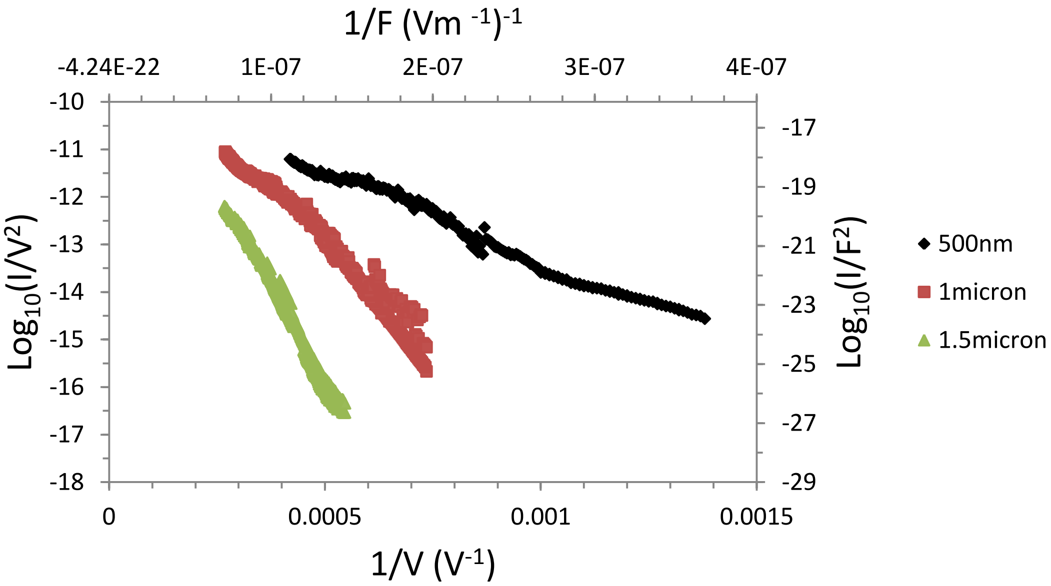

Figure 5.7: FN plots of the *I-V* data from samples in CBD sample set, as shown in figures 5.3 – 5.5. Linear behaviour shows that FE is the dominant emission type.

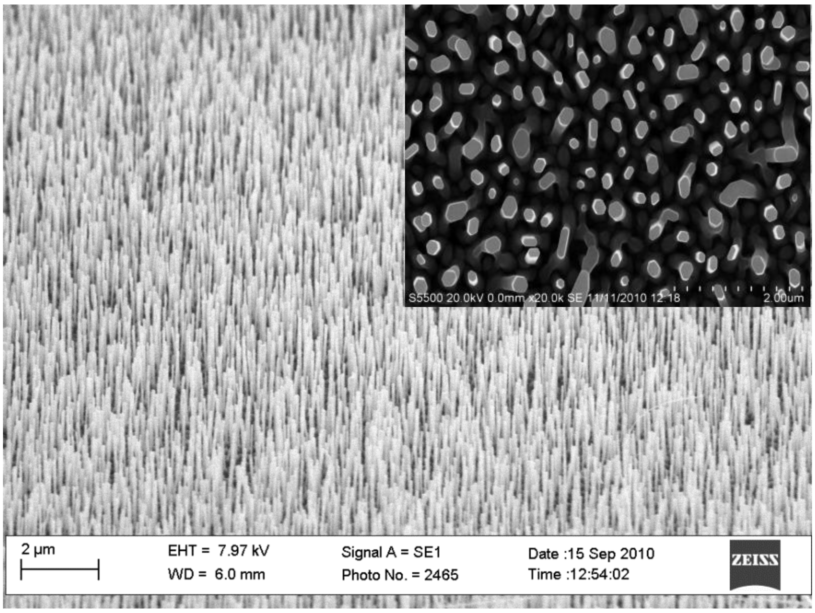

Figure 5.8: SEM image of CTR-VPT(1) nanowire array without controlled inter-wire spacing. Inset shows same sample from above.

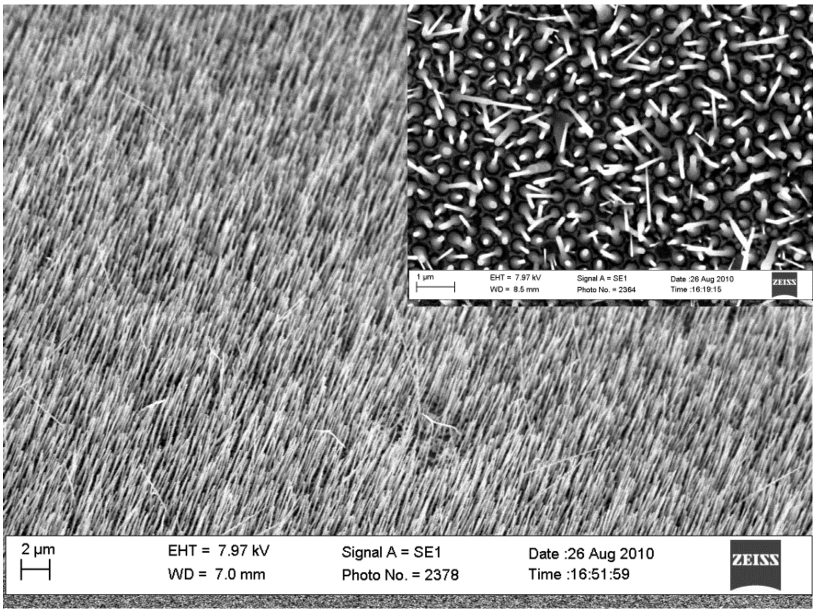

Figure 5.9: SEM image of CTR-VPT(1) nanowire array with 500 nm inter-wire spacing. Inset shows same sample from above.

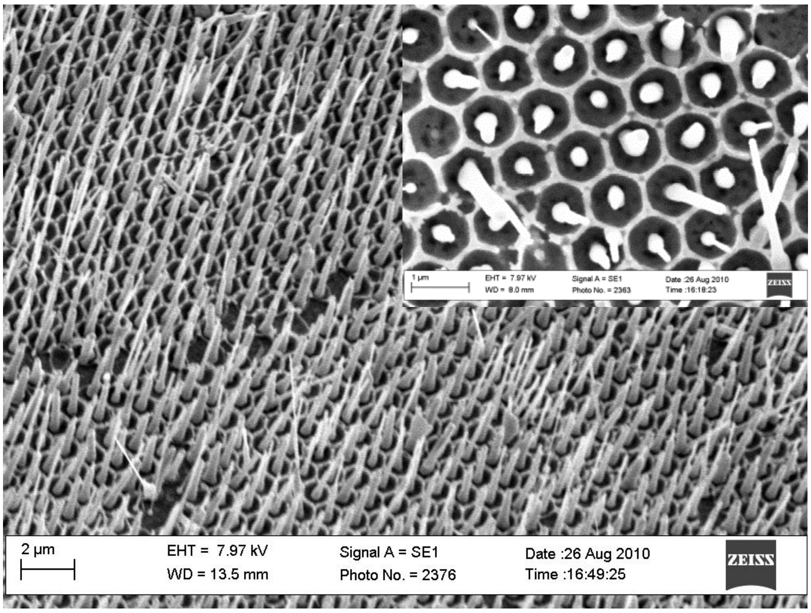

Figure 5.10: SEM image of CTR-VPT(1) nanowire array with 1.0 µm inter-wire spacing. Inset shows same sample from above.

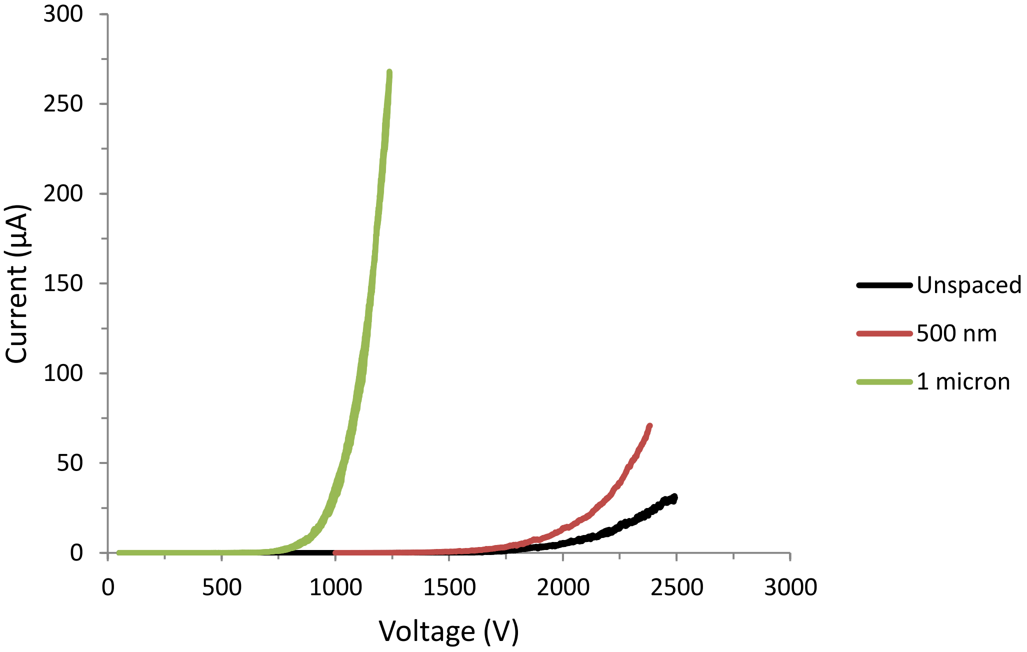

Figure 5.11: I-V curves for samples in VPT1 sample set, as shown in figures 5.8 – 5.10.

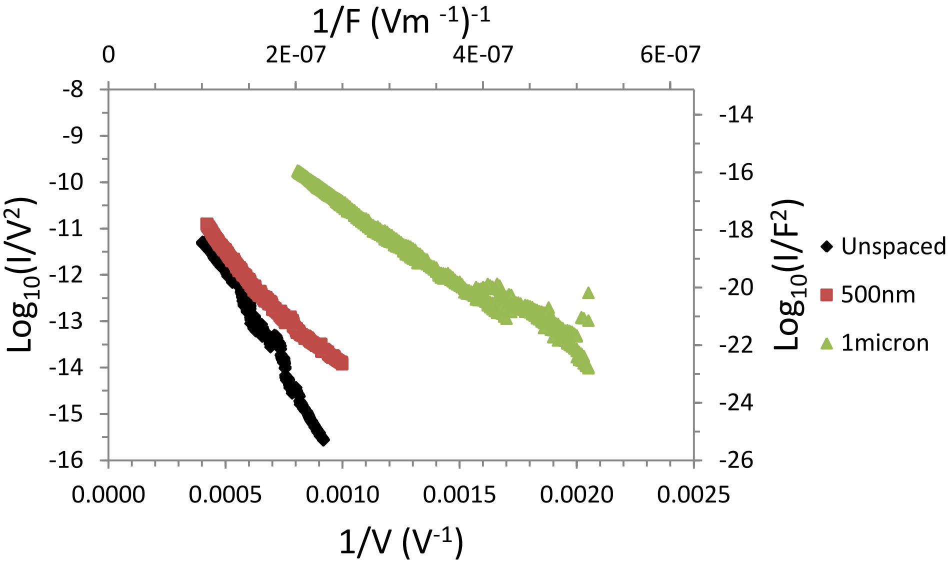

Figure 5.12: FN plots of the *I-V* data from samples in VPT1 sample set, as shown in figures 5.8 – 5.10. Linear behaviour shows that FE is the dominant emission type.

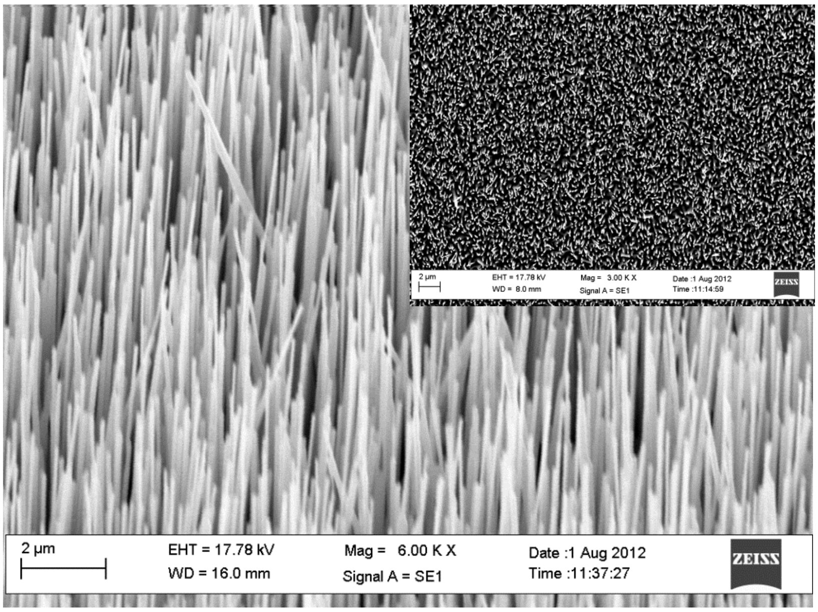

Figure 5.13: SEM image of CTR-VPT(2) nanowire array without controlled inter-wire spacing. Inset shows same sample from above.

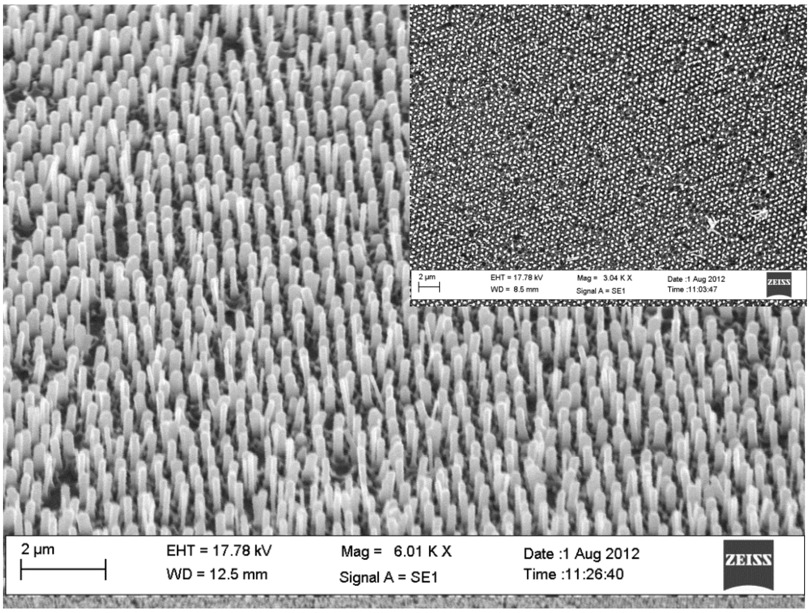

Figure 5.14: SEM image of CTR-VPT(2) nanowire array with 500 nm inter-wire spacing. Inset shows same sample from above.

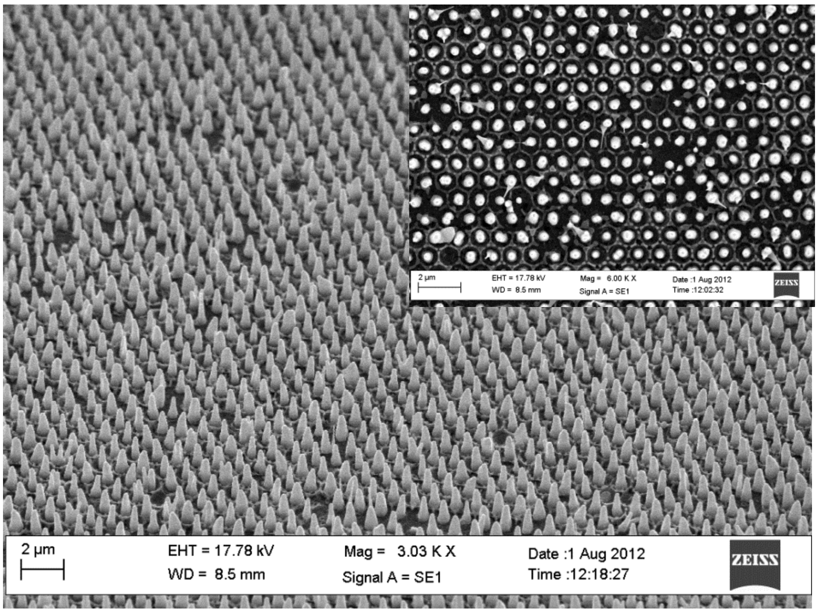

Figure 5.15: SEM image of CTR-VPT(2) nanowire array with 1.0 µm inter-wire spacing. Inset shows same sample from above.

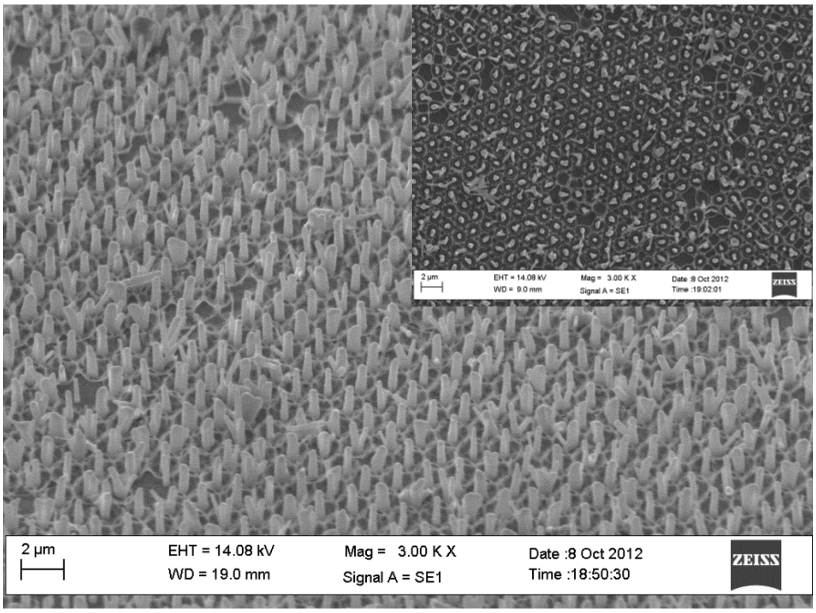

Figure 5.16: SEM image of CTR-VPT(2) nanowire array with 1.5 µm inter-wire spacing. Inset shows same sample from above.

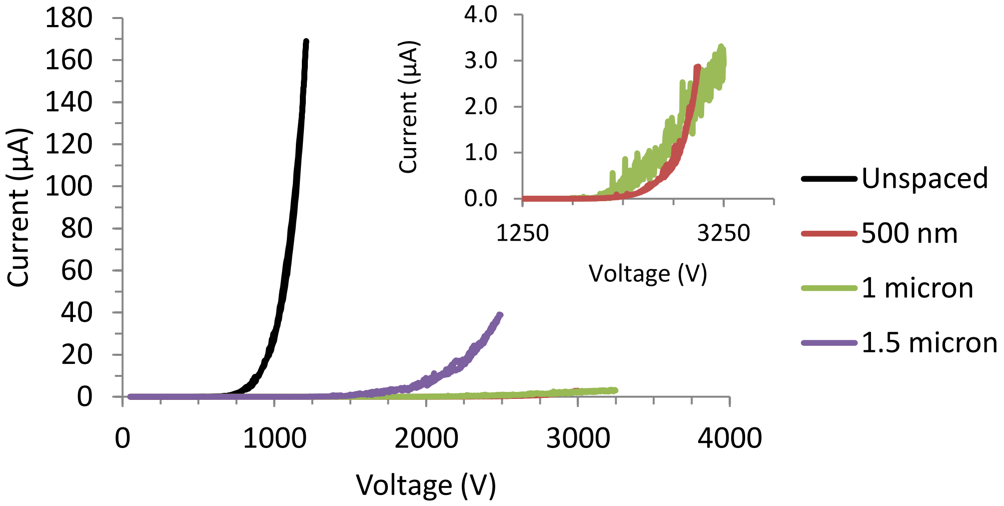

Figure 5.17: *I*-*V* curves for samples in CTR-VPT(2) sample set, as shown in figures 5.13 – 5.16. The inset shows the voltage range 1500 – 3500 V for 500 nm and 1 μm samples.

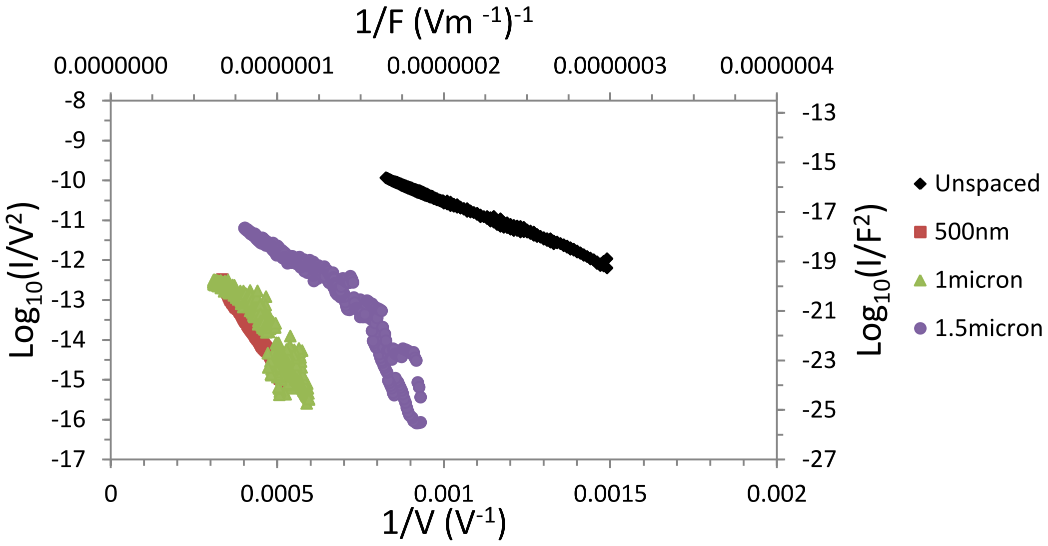

Figure 5.18: FN plots of the *I*-*V* data from samples in VPT2 sample set, as shown in figures 5.13 – 5.16.

5.3.2 Analysis

The data captured from these samples is summarised in table 5.2, sample type refers to CBD or CTR-VPT methods and between CTR-VPT(1) and CTR-VPT(2) samples, which were grown under similar conditions but at different stages of this work. Where no intentional inter-wire spacing is introduced using NSL, the sample is referred to as ‘unspaced’.

Sample type	**Spacing**	**Field enhancement factor γ**	**Turn on voltage (V)**
CBD	500 nm	1229	724
CBD	1.0 μm	554	1360
CBD	1.5 μm	307	1830
CTR-VPT(1)	Unspaced	597	1091
CTR-VPT(1)	500 nm	882	1002*
CTR-VPT(1)	1.0 μm	1528	489
CTR-VPT(2)	Unspaced	1539	671
CTR-VPT(2)	500 nm	385	1905
CTR-VPT(2)	1.0 μm	477	1680
CTR-VPT(2)	1.5 μm	681	1075

Table 5.2: Field enhancement factor γ and turn on voltages for each sample studied. (* The low voltage part of this *I-V* curve was not collected; the turn on voltage indicated is a maximum value, the actual value is most likely lower)

This data is also shown in figure 5.19 and 5.20 as graphs of the field enhancement factor γ vs. array density (the number of nanowires per μm^2). In figure 5.20 the data is represented as 4 graphs, one for each set of samples, these sets are CBD, CTR-VPT(1), CTR-VPT(2), and Unspaced CTR-VPT samples. The unspaced samples are considered separately as the randomness in nanowire distribution means they are morphologically dissimilar to the ordered nanowire arrays.

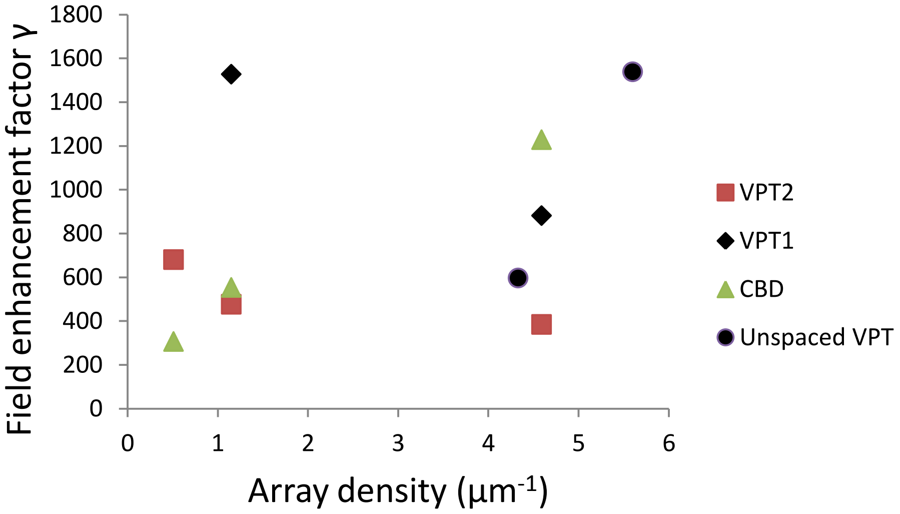

Figure 5.19: Plot of field enhancement factor γ vs. array density for all samples examined.

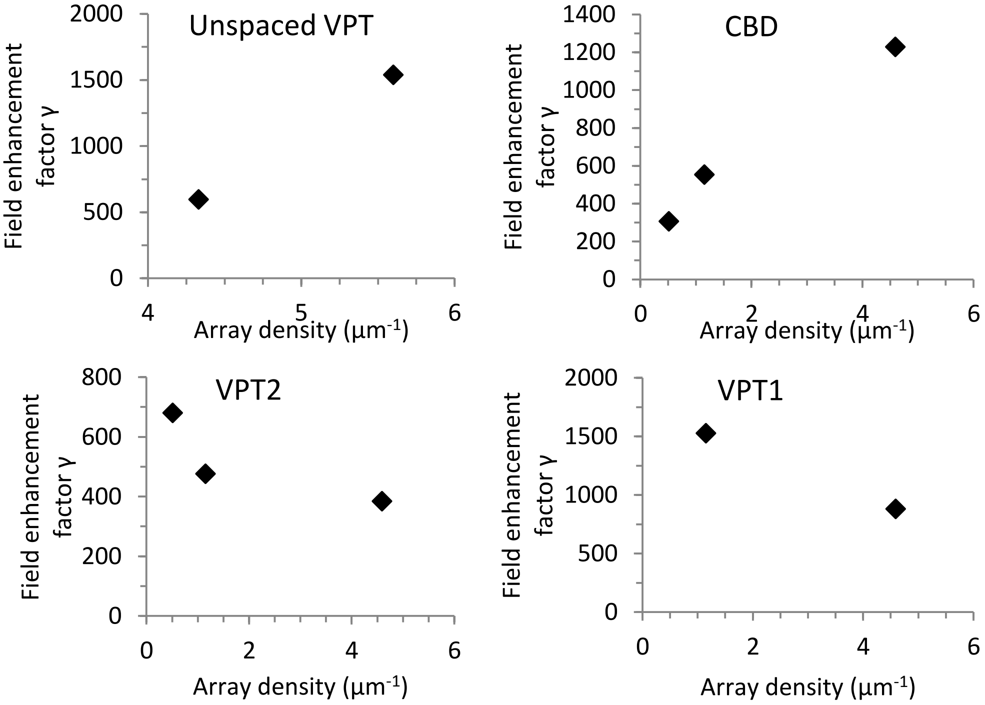

Figure 5.20: Graphs of field enhancement factors γ vs. array density, broken down by sample type.

It was anticipated that the data gathered from these samples would show a trend of increasing γ factors along with decreasing turn on voltages when the inter-wire spacing was increased as numerous reports have concluded that lower nanowire density lead to preferable FE characteristics, due to a reduction in the incidence of closely adjacent nanowires “shielding” each other and thus effectively reducing the high aspect ratio advantages (such as a larger field enhancement factor) expected from such structures [11-14]. While this is the case with the CTR-VPT(1) and the CTR-VPT(2) sets, it is not seen in the CBD or Unspaced VPT sets as seen in figure 5.20. Comparatively poor FE performance by samples produced using CBD methods may be explained by their generally flat tips; it has been reported that nanowires with sharp [15] or narrow [16] tips perform preferably to those with wider or less tapered tips. In order to gain a fuller understanding of the process occurring here, the samples were examined by SEM after FE was carried out.

Significant morphological changes found post-FE, these may be broken down into two categories; melting, likely due to Joule heating in each nanowire during emission, and a significant structural disruption of the substrate such that ZnO nanowires, buffer layer, and Si/SiO_2 substrate apparently violently ‘exploded’ over the surrounding area.

5.3.3 Post-FE morphology

Melting was observed on almost all samples examined post-FE, on most samples this melting was confined to the tips of individual nanowires as shown in figure 5.21. Figure 5.22 shows an area of more extreme melting, with whole nanowires being melted away. This type of damage, again, was observed on most samples examined but was not dominant, and accounted for only a small portion of total sample area in all cases. Melting of this nature has been reported by Semet *et al.* and it attributed to a surface diffusion process caused by the high temperatures during FE [17]; that report deduces that the temperatures occurring during emission are > 1600K.

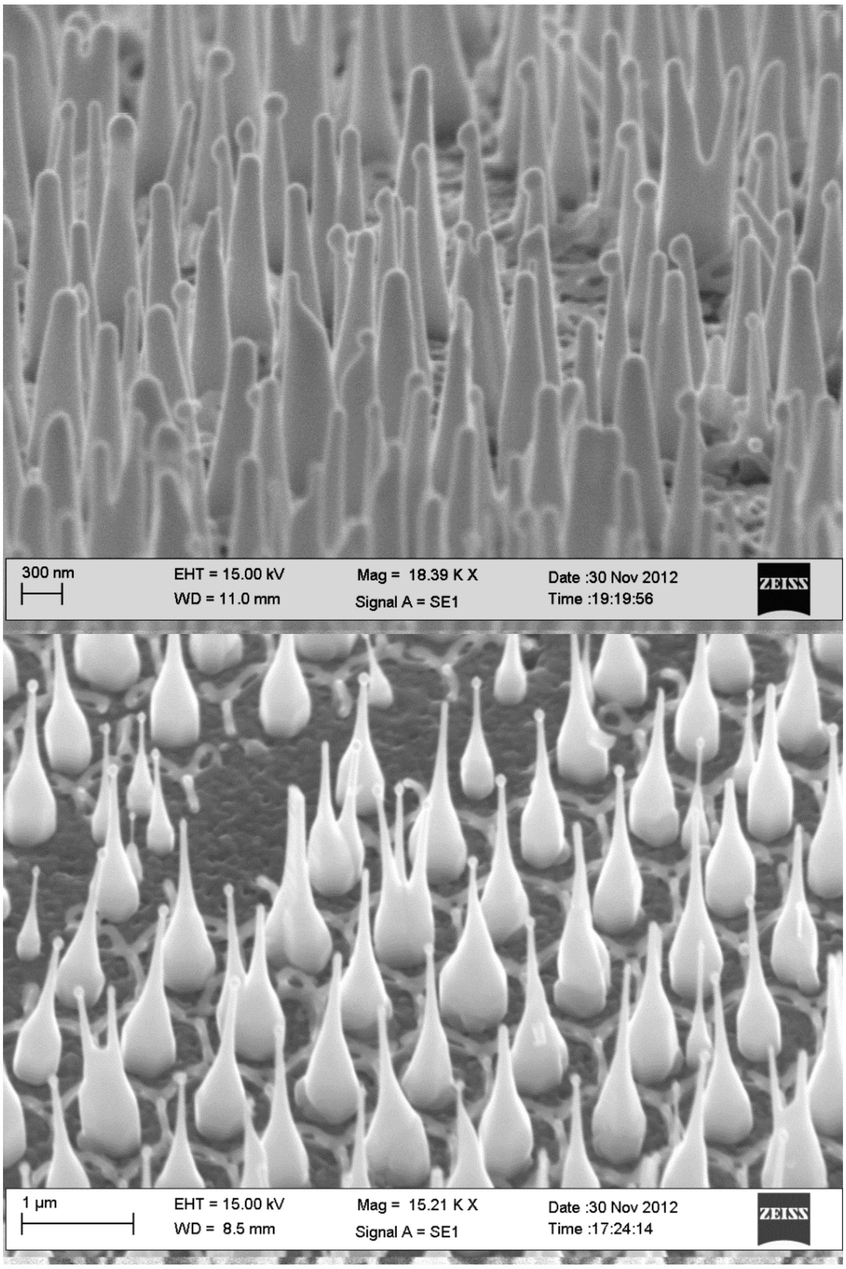

Figure 5.21: Examples of tip melting effects observed on most samples examined. Images here from CTR-VPT(2) 1.0 µm spaced sample.

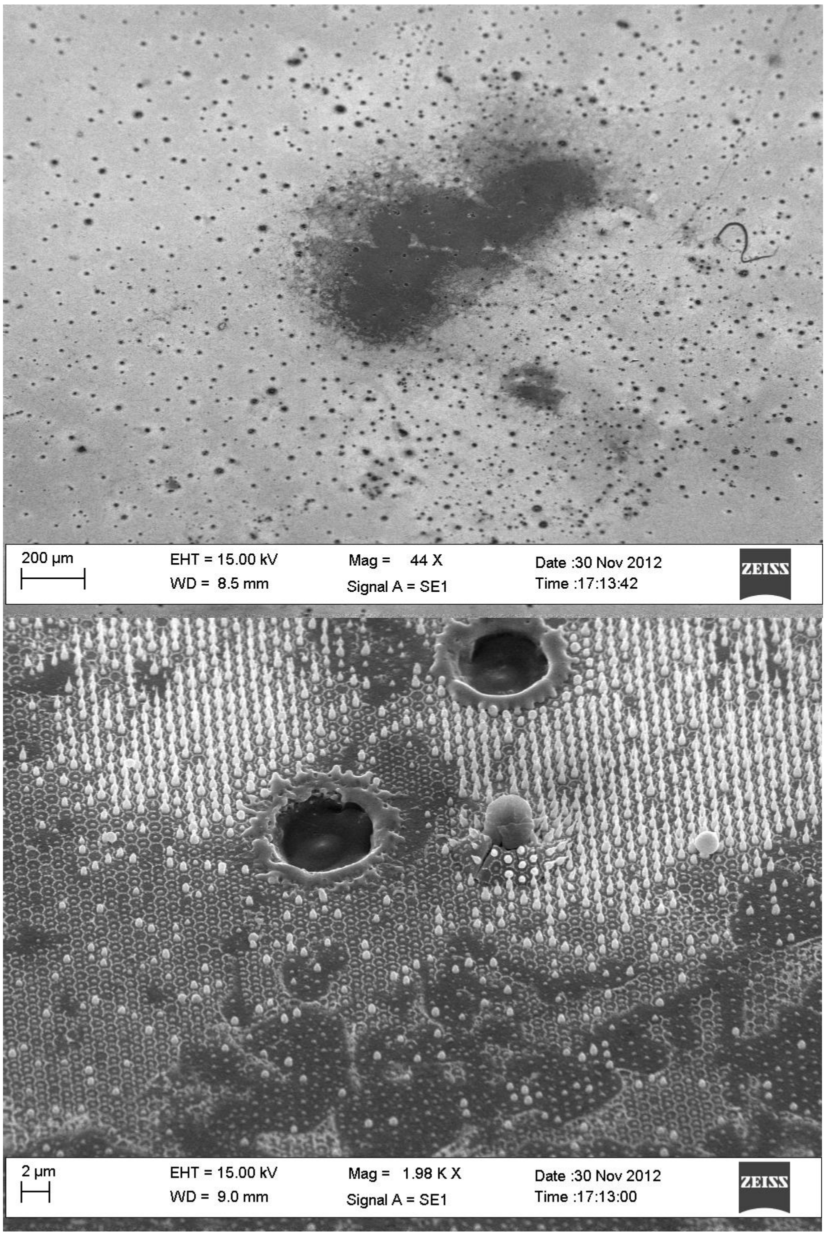

Figure 5.22: Examples of melting damage, the top image shows a large dark contrast area where all nanowires have been melted. This is also observed in lower section of bottom image. The bottom image also shows substrate disruptions due to arcing. Both images from CTR-VPT(2) 1.0 µm spaced sample.

Figure 5.22 shows examples of the second type of damage mentioned, where all ZnO nanowires and buffer layer have been melted entirely and the underlying Si-SiO_2 substrate shows signs of melting and almost explosive damage, figures 5.23 and 5.24 show further examples of this type of morphology. It was observed that damage of this kind tended to occur in clusters, as is seen in the upper part of figure 5.22. It is believed that this damage is caused by arcing during sample conditioning; during the conditioning process the voltage is ramped up and down but many times during this process there will be an electrical arc between sample and anode.

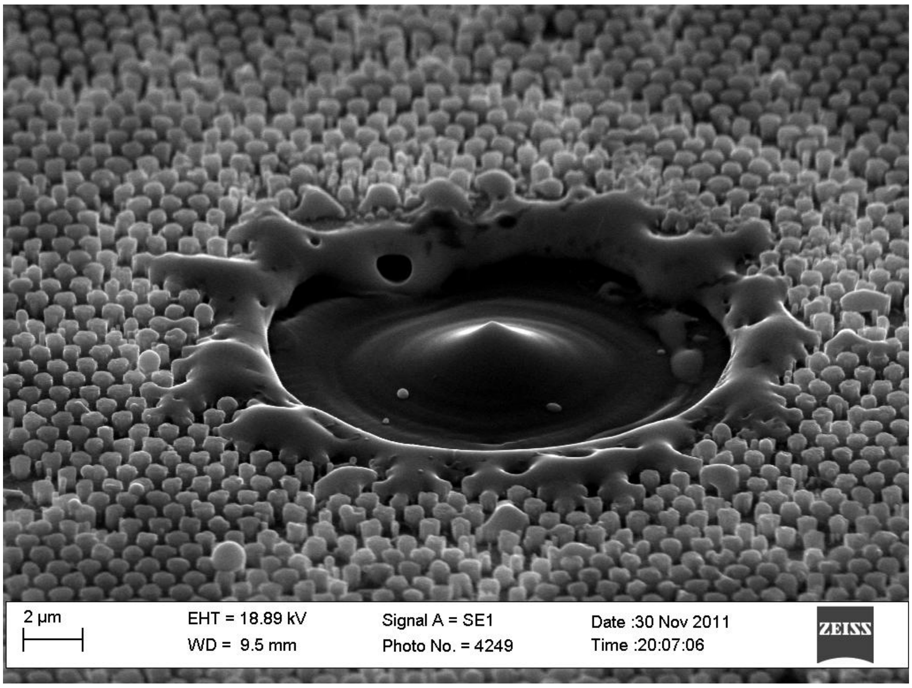

Figure 5.23: Example of substrate damage caused by arcing. Image from CBD 1.0 µm spaced sample.

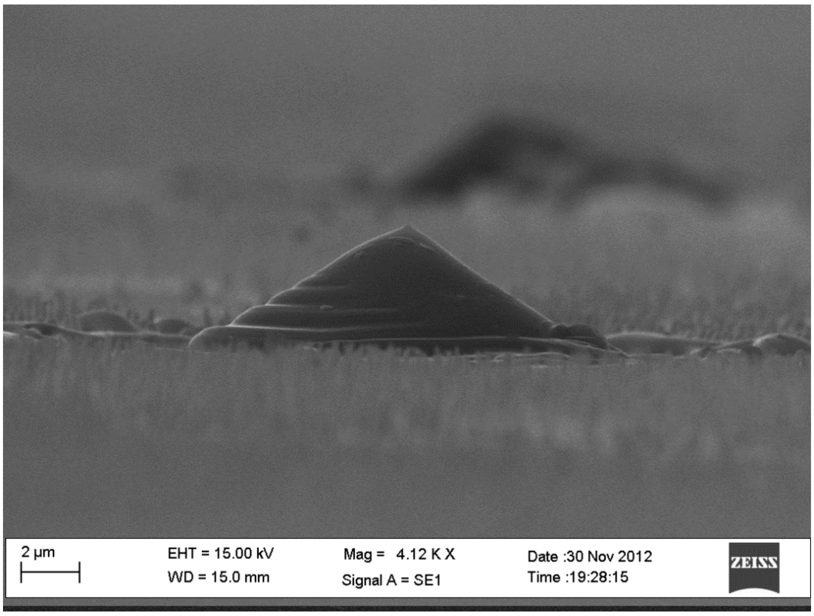

Figure 5.24: Example of substrate damage caused by arcing. The peak is several microns higher than the surrounding nanowires. Image from CTR-VPT(2) 1.0 µm spaced sample.

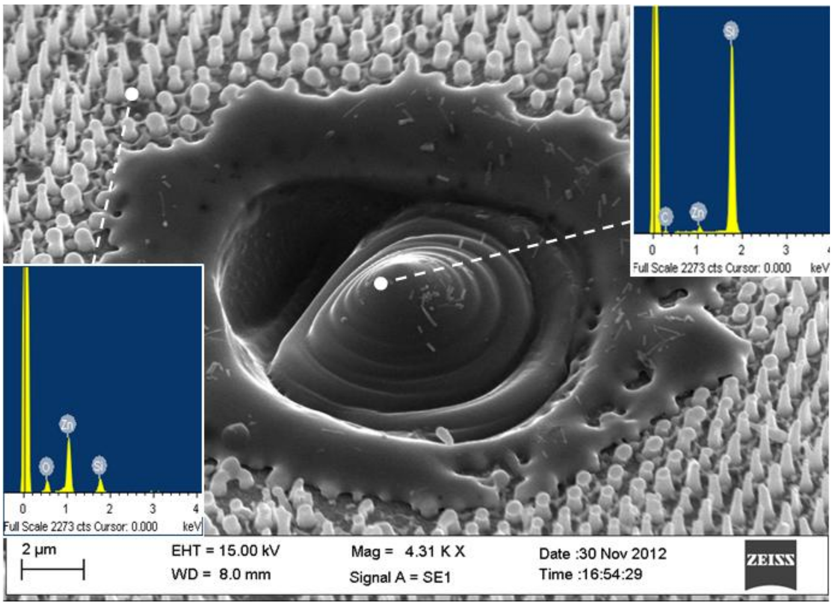

Figure 5.25: EDX data shows that the material forming the peak in this type of damage is composed of silicon. Image from CTR-VPT(2) 1.0 µm spaced sample.

Figure 5.25 shows, using EDX, that the conical structures that are left in the disrupted area are Si which has been melted due to high current density during an arcing event. This type of disruption was described in 1976 by Spindt *et al*. as a runaway gasification effect similar to the case of an exploding wire [18]. This has significant implications on the nature of the *I-V* data gathered and presented above. Since figure 5.24 shows that in some cases these structures may be several μm above the tops of the surrounding ZnO nanowires, it is likely that following their formation, significant emission occurs from these points and reduced emission from the surrounding ZnO nanowires is to be expected. Additionally since these conical structures consist of Si and not ZnO, any Fowler-Nordheim analysis carried out on their *I-V* data will lead to incorrect values for the field enhancement factors β and γ since their calculation is critically dependent on work function.

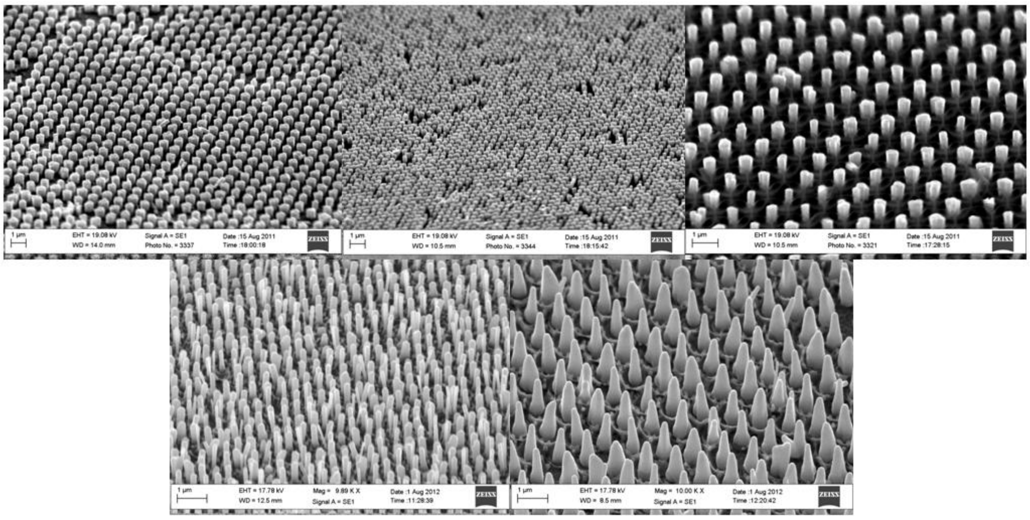

Figure 5.26: Pre-FE SEM images of samples which showed significant damage Post-FE. The top row shows CBD samples of spacing 500 nm, 1.0 μm, and 1.5 μm while the bottom row shows CTR-VPT(2) samples with spacing 500 nm, and 1.0 μm.

For these reasons the *I-V* data gathered from samples which later showed signs of this type of disruption were deemed unsuitable for further analysis. All three CBD samples examined exhibited these structures, along with samples with 500 nm and 1.0 µm inter-wire spacing from the CTR-VPT(2) set of samples.

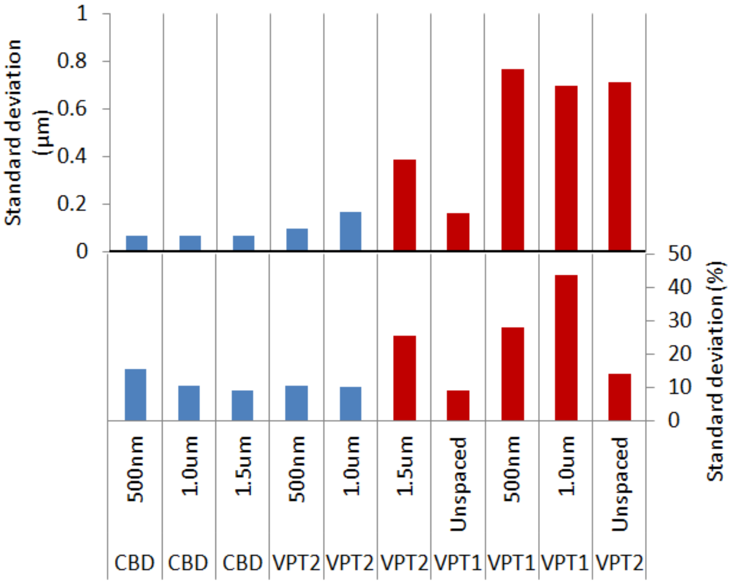

Figure 5.27: Standard deviation in nanowire height for each sample examined. The top shows standard deviation in µm, while the bottom bar chart shows the same information presented as a percentage of nanowire height. In both cases, samples which exhibited disruptions are presented in blue, while those without such damage are red.

As can be seen from the pre-FE SEM images of these samples as shown in figure 5.26, all of the samples that exhibited this kind of damage were extremely uniform, particularly in terms of nanostructure height, while all other samples which were not damaged in this way had significantly greater variance in nanowire height.

The influence of uniformity in height is further shown evidenced by figure 5.27 where the standard deviation in nanowire height is presented. In blue, we can see that those samples which were damaged by arcing events have smaller variations in height than those without. Exceptions to this are the unspaced VPT samples, which have low standard deviations as a percentage of wire height, but yet do not exhibit arcing damage, it is possible that the large degree of randomness in nanowire distribution has a protective effect, much in the same way that a degree of randomness in nanowire height has prevented damage to other samples.

In the case of extremely uniform samples it is possible that a defect in one area, such as precipitate or a slightly taller nanowire, results in a site that emits at a lower voltage and is likely to melt sooner than its surrounding nanowires resulting in the runaway effect described by Spindt *et al.* [18]. It's possible that this form of damage may be avoided by introducing an annealing step under vacuum prior to characterisation to remove any adsorbates from the sample, which may contribute to arcing during FE.

5.3.4 Nanowire array morphology

After disregarding data from samples showing damage of the type shown in figure 5.23 we are left with five samples to examine further. Information from FN analysis along with information about the array morphology is given in table 5.3. Plots of current and current density against voltage are shown in figures 5.28 and 5.29.

Sample type	**Spacing**	**Field enhancement factor γ**	**Turn on voltage (V)**	**Average tip area (μm^2)**	**Average height (μm)**
CTR-VPT(1)	Unspaced	597	1091	0.0195	1.8
CTR-VPT(1)	500 nm	882	1002*	0.0130	2.8
CTR-VPT(1)	1.0 μm	1528	489	0.0171	1.6
CTR-VPT(2)	Unspaced	1539	671	0.0132	5.1
CTR-VPT(2)	1.5 μm	681	1075	0.1092	1.5

Table 5.3: Summary of FE and morphological characteristics of samples not damaged during field emission. (* The low voltage part of this *I-V* curve was not collected; the turn on voltage indicated is a maximum value, the actual value is most likely lower)

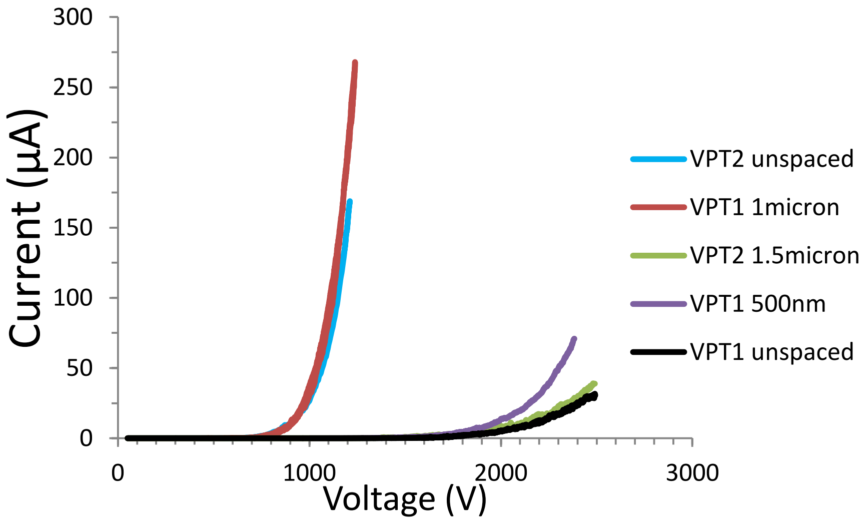

Figure 5.28: *I-V* curves from samples which did not exhibit arcing damage.

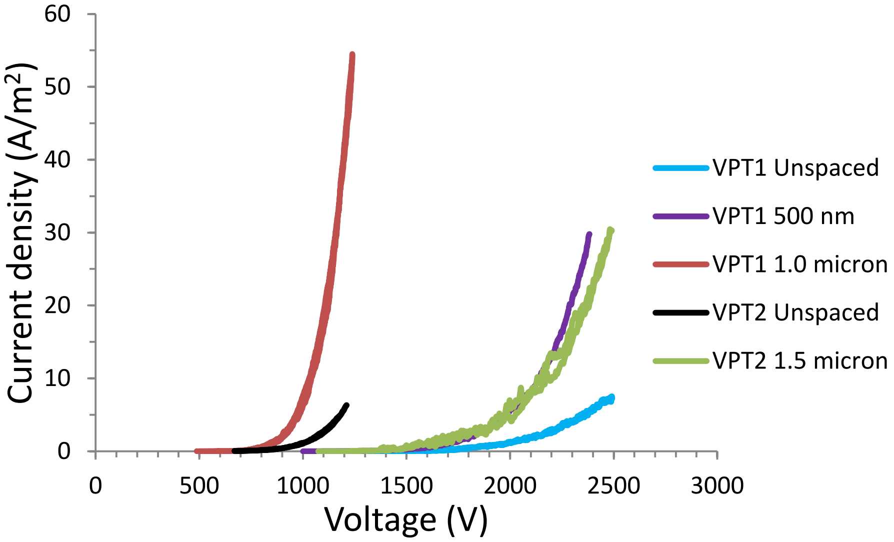

Figure 5.29: Graph of current density *J* against voltage *V*, for samples which did not exhibit arcing damage. Current density is calculated using the calculated total tip area for each sample.

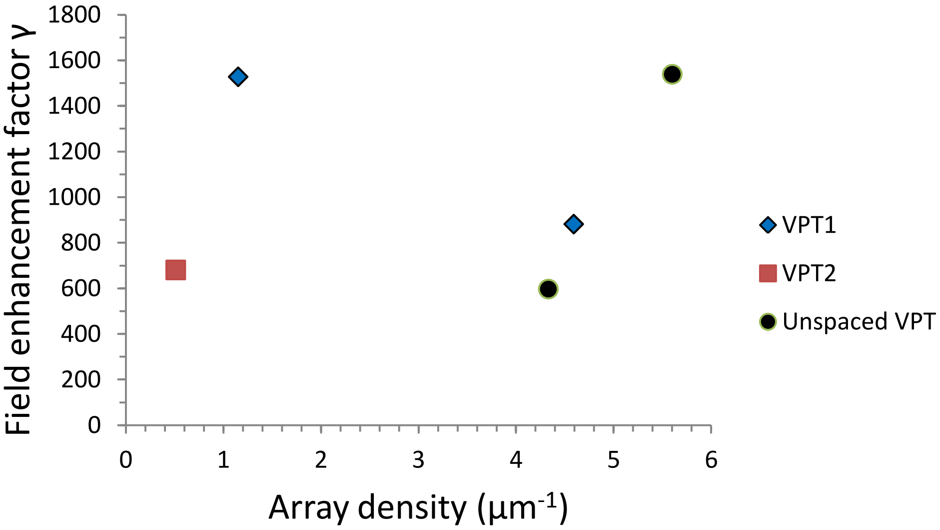

Figure 5.30: Graph of field enhancement factor γ against array density.

Figure 5.30 gives a plot of the field enhancement factor against the array density for those samples which did not suffer extreme damage during FE. Even after disregarding those samples not considered reliable, there is still no clear trend which relates the array density to indicators of FE performance such as the field enhancement factor.

Figure 5.20 showed that within each of the two CTR-VPT sample sets FE performance improved with lower array densities. However, the trend does not hold when these sets are considered all together. It is likely that other differences in morphology are responsible, for example CTR-VPT(1) nanowires are consistently taller than CTR-VPT(2) nanowires. This leads to the conclusion that while nanowire array density is a significant factor in determining FE properties of similar samples, it cannot be used to compare morphologically dissimilar arrays. For this reason, an approach which includes other morphological factors such as nanowire height and tip area must be considered.

Numerous attempts to model the field enhancement factor have been reported in the literature, Forbes *et al.* summarises a selection of these [19]. These models range in complexity from simply taking the nanowire aspect ratio, to modelling nanowire tips as hemispherical, hemi-ellipsoidal, or hyperboloidal emitters [20]. Attempts to model the field screening effect due to the presence of neighbouring emitters have also been reported in the literature , particularly field emission from carbon nanotubes [21, 22] with claims that the ideal emitter separation occurs when nanotube height is approximately one half of the inter-tube distance [23]. The application of such detailed models was not carried out in the work presented here. However, a suggestive trend in the data given above may be found by carrying out a quite simple analysis incorporating the average nanowire morphology in a given array along with the density of nanowires. This analysis will lead only to qualitative results but may be useful in guiding the design of future experiments.

By dividing the average nanowire tip area of a given array by the average nanowire height, a geometric factor with units of µm related to the nanowire aspect ratio is found. The product of this geometric factor and the nanowire array density incorporates both the aspect ratio of the individual nanowires and their number density. We will call this the array geometric factor and it has unit µm^{-1}. Table 5.4 shows the calculated array geometric factor and the array density used:

Sample type	**Spacing**	**Average tip area (µm^2)**	**Average height (µm)**	**Array density (µm^{-2})**	**Array geometric factor (µm^{-1})**
CTR-VPT(1)	Unspaced	0.0195	1.8	4.33	0.0478
CTR-VPT(1)	500 nm	0.0130	2.8	4.59	0.0216
CTR-VPT(1)	1.0 µm	0.0171	1.6	1.15	0.0122
CTR-VPT(2)	Unspaced	0.0132	5.1	5.6	0.0145
CTR-VPT(2)	1.5 µm	0.1092	1.5	0.51	0.0366

Table 5.4: Calculation of array geometric factor for each of the samples not damaged by arcing during field emission.

The array geometric factor may then be plotted against both the field enhancement factor γ and the turn on voltage:

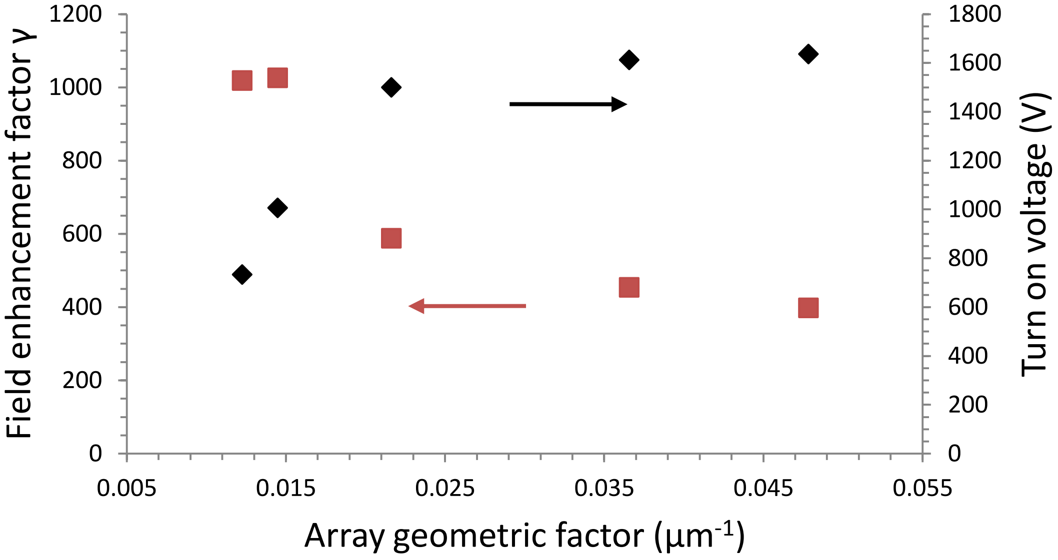

Figure 5.31: Graphs of field enhancement factor (diamonds) and turn on voltage (squares) versus array geometric factor.

Figure 5.31 shows that the array geometric factor is positively correlated to the turn on voltage and negatively correlated to the field enhancement factor. This means that a low array geometric factor is desirable to achieve optimum field emission characteristics and also a useful parameter in characterising such materials for field emission applications.

Since the geometric factor is not based solely on either nanowire aspect ratio or array density it allows for the prediction of array morphologies that may offer greater FE performance than those currently produced. It was previously anticipated that nanowire array density would be the dominant factor in determining the FE properties, but here we see that this remains true only when considering morphologically similar arrays. An example of this is that out of the samples examined, those with the highest field enhancement factors have significantly different array densities of 1.15 and 5.6 μm^{-2}. However this can be explained by the difference in morphology of the individual nanowires in these arrays, which results in these two particular arrays having very similar array geometric factors.

5.4 FE imaging

FE imaging as described in section 2.10.1 was carried out on all samples. Figure 5.32 shows three images taken from the sample VPT1-1μm. The images from left to right are taken at voltages of 1250, 1500, and 1750 V respectively. This sample had the highest enhancement factor and lowest turn on voltage of all samples examined.

Figure 5.32 also shows that as the voltage increases the number of sites emitting increases with it. The turn on voltage of this sample is < 500 V, meaning that at 500 V, field emission is the dominant electron emission process. However, it is seen in the phosphor images that significant light emission from the phosphor screen is not observed until the voltage reaches ~ 1750 V.

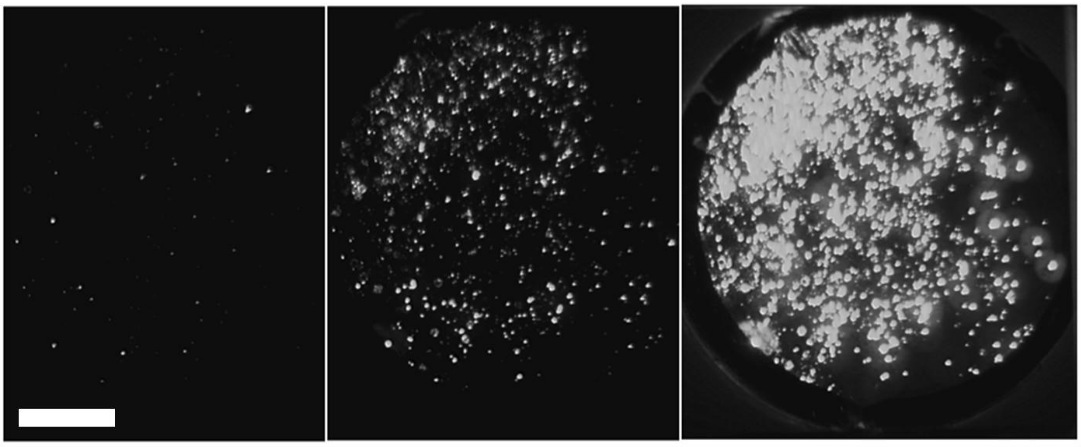

Figure 5.32: Phosphor images taken by using a phosphor coated electrode. Bright areas indicate electron emission. From left, images are taken at voltages of 1250, 1500, and 1750 V. The scale bar indicates 2 mm.

There is a large difference between the turn on voltage for this sample (489 V) and the voltage at which significant light emission is observed. This result is also significant for the other samples, as no other sample produced images which showed significant phosphorescence, for these samples, even at high voltages, only very spotty patterns similar to the low voltage image above were observed. This may be due to the difference between the voltage required for field emission and that required to achieve phosphorescence. When ramping the voltage for imaging purposes, in order to protect the phosphor electrode from damage the voltage is not increased so high that an arc might occur. For this reason, the range of voltages used for most of the samples may have been too narrow to achieve phosphor images for these samples.

5.5 Conclusions

In this chapter we have examined the FE properties of samples produced using both CBD and CTR-VPT techniques. It was found that nanowire array morphology plays a large role in determining FE properties. In almost all cases, the samples under investigation were observed to melt slightly during field emission. On certain samples however, significant damage was caused during the FE experimental procedure. Regions of the sample were covered with crater-like marks which in most cases are occupied by a central conical structure. EDX measurements carried out on these structures determined that they were formed from silicon. It is believed that these structures are formed by a runaway emission process (arcing) in which high currents are emitted leading to the high temperatures required to melt the Si/SiO_2 substrate. Due to concerns about the quality of subsequent *I-V* data produced by these samples, they were not examined further.

The five remaining samples, which were not damaged during the course of FE measurements, were examined and reveal no obvious trend in either the turn on voltages or field enhancement factor γ with respect to the array inter-wire spacing by itself, as had been anticipated. However when an array geometric factor which includes the average nanowire height, tip area, and array density is calculated, a correlation is seen with both the field enhancement factor (negative correlation) and the turn on voltage (positive correlation).

The correlation between FE performance and this array geometric factor will inform any work carried out in the future in our laboratory on what types of array morphologies are most desirable for FE purposes. The data and analysis presented in this chapter strongly suggests that FE is not solely dependent on the nanowire array density but also the aspect ratio of the nanowires in the array, as no trend is found between dissimilar samples when only considering array density. Design of future experiments will also be guided by the morphology of the samples on which destructive melting of the underlying substrate took place. It is observed that the samples that were damaged in this way were extremely uniform prior to FE, particularly in terms of nanowire height. The CBD growth technique deposits nanowire arrays with very consistent nanowire height, all three CBD samples examined by FE were destroyed in this way. The other two samples destroyed were CTR-VPT samples of 500 nm and 1 μm inter-wire spacing. These particular samples were unusually uniform in terms of height when compared to other CTR-VPT samples examined.

It appears, based on the work presented in this chapter, that in order to achieve optimum FE properties from an array of ZnO nanowires, a sample should be designed such that its array geometric factor is as low as possible while also maintaining a small non-uniformity in nanowire height to help protect from arcing damage. This present work offers evidence that while lateral ordering is an important factor in similar samples, while comparing samples with varying nanowire morphologies, consideration must be given to other factors such as nanowire height and tip area. Furthermore, and quite unexpectedly, it appears that strong uniformity in height is extremely detrimental to FE from such ZnO nanowire array structures, as it encourages arcing and sample disruption because a defect in one area, such as a precipitate or one (or a small number of) slightly taller nanowire(s), results in a site where a large current flows locally, causing significant heating and damage there.

Finally, all samples examined were imaged using a phosphor electrode to determine the uniformity of emission. All but one sample resulted in phosphor images where only a small number of points were lit up. Significantly, this sample had the lowest turn on voltage and highest field enhancement factor. However, even still, the voltage required to cause phosphorescence over a large area of the electrode was significantly higher than its turn on voltage using the metallic *I-V* electrode. This suggests that a current high enough to cause phosphorescence using the other samples with poorer FE characteristics may be out of the range of voltages scanned.

5.6 References

1. Richardson, O.W., *On the Extraction of Electrons from Cold Conductors in Intense Electric Fields.* Proceedings of the Royal Society of London. Series A, 1928. **117**(778): p. 719-730.

2. Richardson, O.W., *Nobel lecture on thermionics*, 1929.

3. Nordheim, L.W., *The Effect of the Image Force on the Emission and Reflexion of Electrons by Metals.* Proceedings of the Royal Society of London. Series A, 1928. **121**(788): p. 626-639.

4. de Bruyne, N.A., *The Action of Strong Electric Fields on the Current from a Thermionic Cathode.* Proceedings of the Royal Society of London. Series A, 1928. **120**(785): p. 423-437.

5. Sahni, V. and K.P. Bohnen, *Image charge at a metal surface.* Physical Review B, 1985. **31**(12): p. 7651-7661.

6. Fowler, R.H. and L. Nordheim, *Electron Emission in Intense Electric Fields.* Proceedings of the Royal Society of London. Series A, 1928. **119**(781): p. 173-181.

7. Young, R.D. and E.W. Müller, *Experimental Measurement of the Total-Energy Distribution of Field-Emitted Electrons.* Physical Review, 1959. **113**(1): p. 115-120.

8. Murphy, E.L. and R.H. Good, Jr., *Thermionic Emission, Field Emission, and the Transition Region.* Physical Review, 1956. **102**(6): p. 1464-1473.

9. Miller, S.C., Jr. and R.H. Good, Jr., *A WKB-Type Approximation to the Schrödinger Equation.* Physical Review, 1953. **91**(1): p. 174-179.

10. McCarthy, E., et al., *Field emission in ordered arrays of ZnO nanowires prepared by nanosphere lithography and extended Fowler-Nordheim analyses.* Journal of Applied Physics, 2011. **110**(12): p. 124324-124324.

11. Rajendra Kumar, R.T., et al., *Control of ZnO nanorod array density by Zn supersaturation variation and effects on field emission.* Nanotechnology, 2007. **18**(21).

12. Jo, S.H., et al., *Field-emission studies on thin films of zinc oxide nanowires.* Applied Physics Letters, 2003. **83**(23): p. 4821-4823.

13. Lee, J.-H., et al., *Density-controlled growth and field emission property of aligned ZnO nanorod arrays.* Applied Physics A, 2009. **97**(2): p. 403-408.

14. Banerjee, D., S.H. Jo, and Z.F. Ren, *Enhanced Field Emission of ZnO Nanowires.* Advanced Materials, 2004. **16**(22): p. 2028-2032.

15. Yang, Y.H., et al., *Field emission of one-dimensional micro- and nanostructures of zinc oxide.* Applied Physics Letters, 2006. **89**(4): p. 043108-3.

16. Zhang, Z., et al., *The influence of morphologies and doping of nanostructured ZnO on the field emission behaviors.* Solid-State Electronics, 2009. **53**(6): p. 578-583.

17. Semet, V., et al., *Field emission behavior of vertically aligned ZnO nanowire planar cathodes.* Journal of Applied Physics, 2011. **109**(5): p. 054301-5.

18. Spindt, C.A., et al., *Physical properties of thin-film field emission cathodes with molybdenum cones.* Journal of Applied Physics, 1976. **47**(12): p. 5248-5263.

19. Forbes, R.G., C.J. Edgcombe, and U. Valdrè, *Some comments on models for field enhancement.* Ultramicroscopy, 2003. **95**(0): p. 57-65.

20. Yuasa, K., et al., *Modified Fowler–Nordheim field emission formulae from a nonplanar emitter model.* Surface Science, 2002. **520**(1–2): p. 18-28.

21. Chen, G., et al., *Screening effects on field emission from arrays of (5,5) carbon nanotubes: Quantum mechanical simulations.* Physical Review B, 2007. **76**(19): p. 195412.

22. Suh, J.S., et al., *Study of the field-screening effect of highly ordered carbon nanotube arrays.* Applied Physics Letters, 2002. **80**(13): p. 2392-2394.

23. Nilsson, L., et al., *Scanning field emission from patterned carbon nanotube films.* Applied Physics Letters, 2000. **76**(15): p. 2071-2073.

Chapter 6: Conclusions and further work

6.1 Conclusions

In this thesis, we have presented the results of investigations into the production of spatially ordered arrays of ZnO nanowires and their use in FE applications. As described in chapter 1, there are numerous other potential applications for which ordered nanowire arrays would be beneficial. In this work, the process of producing these arrays, starting from bare Si/SiO_2 substrate to characterisation of final product, is described. SEM is the technique used predominantly to characterise the morphology of samples produced and each step in the process is described in detail. Once produced, the FE characteristics of these arrays were measured, revealing a significant dependency of FE performance on nanowire array morphology. The bulk of the experimental work and analysis carried out in this thesis is presented in three results chapters (chapters 3 to 5), each of which is summarised briefly below in terms of main outcomes.

6.1.1 Deposition techniques

In this chapter deposition of ZnO buffer layers and nanowires is examined. Two techniques are investigated for the purpose of depositing ZnO buffer layers and two techniques for the deposition of ZnO nanowires.

Since ZnO will not readily nucleate on bare Si/SiO$_2$ substrates it was necessary to deposit a buffer layer of ZnO prior to any nanowire deposition and this was done using both PLD and CBD methods. This layer is required for two reasons, firstly to provide energetically favourable sites for nucleation and secondly to ensure that subsequent depositions are vertically aligned.

PLD was used to deposit buffer layers of ZnO with high crystal quality and uniformity using techniques developed previously in our group while in order to deposit ZnO buffer layers on Si/SiO$_2$ substrates using CBD, an initial seeding step was required. This involved drop coating ZnO seeds on the substrate prior to immersion in the ZnO precursor solution. CBD growth yielded layers with thicknesses similar to those produced using PLD (200 – 300 nm) and also with good c-axis alignment as confirmed by XRD. ZnO nanowire growth was then carried out on buffer layers produced using both techniques with no significant differences in subsequent nanowire morphology noted.

CBD nanowire depositions were carried out resulting in arrays with highly uniform nanowire length which was found to be proportional to the deposition times. The Zn precursor material used predominantly in this work is Zn acetate, which yields nanowire tips which are wider at the tip than at the base. Due to this lateral growth the height of wires grown in this way is limited as adjacent nanowires will ultimately coalesce and form a thin film.

CTR-VPT depositions were carried out in a single zone tube furnace at temperatures of approximately ~ 900°C, which yielded arrays of highly uniform and relatively high aspect ratio nanowires. There are a large number of variables which must be controlled while using this technique, including temperature, quantities of source materials, substrate position, carrier gas flow, etc. Small changes to these variables lead to significant changes in array morphology produced and must be tightly controlled. However this does provide the opportunity to tailor conditions to achieve a particular desired morphology. The knowledge and understanding gained during efforts to produce these structures, and the production of the structures, are the major outcomes of this chapter.

6.1.2 Nanosphere lithography

In this chapter the deposition of spatially ordered arrays of ZnO nanowires by both CBD and CTR-VPT techniques was achieved using NSL. This technique relies on the tendency of nano-scale polystyrene spheres to self assemble into a close packed monolayer. When this layer is deposited onto a substrate using a water-transfer technique it may be used as a template for subsequent nanowire growth. This was achieved using two distinct techniques: one that deposited catalyst material (Au) through the apertures in the mask creating a hexagonal pattern on the substrate which may be grown upon using CTR-VPT and one that deposited a silica sol through the spheres leaving a honeycomb silica mask through which both CBD and CTR-VPT growth may occur.

Growth was carried out on the Au catalysed samples using the VLS growth mechanism, this leads to the growth of highly ordered and uniform nanowire arrays. However difficulty in controlling the Zn vapour concentration during deposition resulted in relatively small areas of the substrate being grown upon as desired, with other areas being covered in uncontrolled growth due to VS growth occurring at points not catalysed by Au.

CBD depositions carried out through the silica mask yielded very uniform arrays, particularly with respect to nanowire height. However due to the lateral growth of the Zn acetate derived CBD technique the distance between adjacent wires is reduced.

CTR-VPT deposition through the silica mask yielded arrays of high quality wires; however issues including multi-wire nucleation and poor uniformity were experienced. Both these issues however were removed through the implementation of a hybrid CBD/CTR-VPT technique. Nanowire arrays with inter-wire distances of 500 nm, 1 µm, and 1.5 µm were produced in this manner and these arrays with controlled distances, and the knowledge and understanding gained during efforts to produce these, are the major outcomes of this chapter.

6.1.3 Field emission

In this chapter the field emission properties of samples produced using both CBD and CTR-VPT techniques were examined. Three sets of samples were examined; two produced using CTR-VPT and one by CBD. Each set contained samples of various inter-wire distances using NSL methods to control these distances.

The FE performance observed varied significantly and was found to be related to the morphology of each sample. Nanowire arrays consisting of tall narrow wires with a low average density performed the best with turn on voltages and field enhancement factors significantly better than those with shorter or wider nanowires and more densely packed arrays.

Significant changes in morphology were observed post-FE, with nanowires which had been melted leaving a bulbous tip at the top of each wire. It is not understood fully what affect this has on the emission properties or at what current density this occurs. While most samples examined exhibited this type of melting it was not considered deleterious to the results. However a number of samples exhibited more significant damage where regions of nanowires and the underlying ZnO buffer layer were melted in their entirety revealing the Si/SiO_2 substrate underneath. In these cases the underlying substrate also shows signs of extreme melting and the formation of conical Si structures which in some cases are taller than the nanowires being examined. Samples exhibiting this form of damage were not considered in further analysis.

SEM images of the nanowire arrays allowed for the calculation of an array geometric factor which incorporates nanowire length, tip area, and inter-wire distance. This is shown to correlate with both the turn on voltage and field enhancement factor, which are both commonly used measures of FE characteristics. The two best performing samples had significantly different inter-wire distances but yet performed quite similarly. Results such as this may now be reconciled by calculating the geometric factor for each array. The results in this chapter provide strong evidence that nanowire array density is only one of a number of morphological factors impacting on FE performance, and indicate that a degree of randomness in nanowire height may contribute to sample robustness during FE. This is a different perspective to that generally reported in the literature and is the major outcome from this chapter.

6.2 Further work

The main conclusion of this thesis is that the relative FE performance of the samples examined show a trend where the calculated array geometric factor is correlated with both the turn on voltage and enhancement factors. This suggests that it is possible to design ZnO nanowire arrays such that their FE performance is maximised. Realising this goal will require further refinement in the techniques used in this thesis.

The use of NSL has allowed for the growth of spatially ordered arrays of nanowires. However the morphology of nanowires grown using CTR-VPT is subject to a great deal of variation with respect to wire length and diameter. In this work arrays of various inter-wire distances are presented but inconsistencies in both length and average nanowire diameter complicate analysis of FE data. In order to identify a quantifiable relationship between array density and FE data these parameters need to be controlled more tightly. In both CBD and CTR-VPT depositions, the diameter of nanowires grown is to some extent related to the diameter of nanospheres used to pattern the substrate, as the size of the contact points left exposed varies with sphere size. This inconsistency may be removed by using a process such as reactive-ion etching of an array of already deposited spheres such that they remain at the same position relative to each other but the diameter of each sphere is reduced.

Furthermore, the silica sol technique used to pattern samples has been very effective when using spheres of 500 nm and 1 µm diameter. Difficulties were experienced when scaling this up to spheres of 1.5 µm diameter and it is considered likely that this difficulty will continue with larger spheres. Further work is required in this area so that this technique may be scaled up to larger sphere sizes, since for FE purposes it appears that larger spacing is preferable.

Significant sample melting and disruptions were observed during this work. The nature of these events is not fully understood, particularly in terms of their detailed impact on the quality of data gathered. It would be desirable to carry out experiments to determine at what voltage/current these effects occur at and how they may be reduced/prevented. Major surface disruptions, most probably due to arcing, of the type described in this thesis are especially detrimental to FE emission quality and uniformity and may represent an issue for ZnO nanowires in terms of whether such structures will ultimately be candidates for industrial–scale, high performance FE applications. Further work is needed to determine the exact causes of such disruptions, and how such effects may be avoided. Since it has been shown in this work that samples with extremely uniform heights are more likely to exhibit this damage, introducing a small random variance in nanowire height throughout an array may be beneficial in reducing the occurrence of the effect.

Finally, further work is required to expand the physical understanding of the array geometric factor calculated in this work. In particular it would be of significant interest to understand over what range of values of tip area, nanowire height, and array density does the correlation hold. These goals may be achieved through both experimental FE analysis of nanowire arrays produced with significant differences in morphologies and also through more general theoretical and/or computational studies.